NAVAL POSTGRADUATE SCHOOL

MONTEREY, CALIFORNIA

DISSERTATION

CONSTRUCTION AND CHARACTERIZATION OF A DUAL ATOMIC BEAM ACCELEROMETER/GYROSCOPE

by

Michael Manicchia

June 2020

Dissertation Supervisor: Francesco A. Narducci

THIS PAGE INTENTIONALLY LEFT BLANK

REPORT DOCUMENTATION PAGE

Form Approved OMB No. 0704–0188

1. AGENCY USE ONLY *(Leave Blank)*	2. REPORT DATE June 2020	3. REPORT TYPE AND DATES COVERED Dissertation

4. TITLE AND SUBTITLE

CONSTRUCTION AND CHARACTERIZATION OF A DUAL ATOMIC BEAM ACCELEROMETER/GYROSCOPE

5. FUNDING NUMBERS

RPMB4; RPMQU; RPMJK

6. AUTHOR(S)

Michael Manicchia

7. PERFORMING ORGANIZATION NAME(S) AND ADDRESS(ES)

Naval Postgraduate School
Monterey, CA 93943

8. PERFORMING ORGANIZATION REPORT NUMBER

9. SPONSORING / MONITORING AGENCY NAME(S) AND ADDRESS(ES)

Naval Research Laboratory, 4555 Overlook Ave SW, Washington, DC

10. SPONSORING / MONITORING AGENCY REPORT NUMBER

11. SUPPLEMENTARY NOTES

12a. DISTRIBUTION / AVAILABILITY STATEMENT

Approved for public release. Distribution is unlimited

12b. DISTRIBUTION CODE

13. ABSTRACT *(maximum 200 words)*

Current sensors used for inertial navigation are based on technology with inherent sensitivity limitations. Atom interferometry is a very promising replacement, which could yield many orders of magnitude of improvement in sensitivity, leading to more accurate navigation over longer periods of time relative to current technology. This research investigates the physics of atom interferometry through the construction and characterization of an atomic accelerometer/gyroscope combination. In contrast to current state-of-the-art atomic sensors, which use pulsed cold atom sources and pulsed laser beams, the apparatus investigated relies purely on continuous atomic and laser beams. These differences would result in a sensor that lends itself more readily to smaller sizing, lower power consumption, and reduced complexity. This change in approach to atomic interferometry also introduces challenges resulting from laser and atomic beam divergences and the velocity averaging due to both longitudinal and transverse temperature, which this dissertation shows how to overcome. The work contained herein explores many stages of construction of an atomic gyro including the demonstration and characterization of two-dimensional laser cooling of atoms, stimulated Raman transitions, and Ramsey and spin echo interference. The implications for future research are also outlined and discussed.

14. SUBJECT TERMS

atom interferometry, laser cooling, Raman, Ramsey, spin echo, accelerometers, gyroscopes, inertial navigation, GPS-denied navigation

15. NUMBER OF PAGES 135

16. PRICE CODE

17. SECURITY CLASSIFICATION OF REPORT	18. SECURITY CLASSIFICATION OF THIS PAGE	19. SECURITY CLASSIFICATION OF ABSTRACT	20. LIMITATION OF ABSTRACT
Unclassified	Unclassified	Unclassified	UU

Standard Form 298 (Rev. 2–89)
Prescribed by ANSI Std. 239–18

i

THIS PAGE INTENTIONALLY LEFT BLANK

CONSTRUCTION AND CHARACTERIZATION OF A DUAL ATOMIC BEAM ACCELEROMETER/GYROSCOPE

Michael Manicchia
Commander, United States Navy
BS, U.S. Naval Academy, 2000
MA, Naval War College, 2014

Submitted in partial fulfillment of the
requirements for the degree of

DOCTOR OF PHILOSOPHY IN APPLIED PHYSICS

from the

NAVAL POSTGRADUATE SCHOOL
June 2020

Approved by: Francesco A. Narducci
                Dissertation Supervisor   Dissertation Committee Chair

Approved by: Peter Denning
                Chair, Department of Physics

Approved by: Douglas Moses
                Vice Provost for Academic Affairs

iii

THIS PAGE INTENTIONALLY LEFT BLANK

ABSTRACT

Current sensors used for inertial navigation are based on technology with inherent sensitivity limitations. Atom interferometry is a very promising replacement, which could yield many orders of magnitude of improvement in sensitivity, leading to more accurate navigation over longer periods of time relative to current technology. This research investigates the physics of atom interferometry through the construction and characterization of an atomic accelerometer/gyroscope combination. In contrast to current state-of-the-art atomic sensors, which use pulsed cold atom sources and pulsed laser beams, the apparatus investigated relies purely on continuous atomic and laser beams. These differences would result in a sensor that lends itself more readily to smaller sizing, lower power consumption, and reduced complexity. This change in approach to atomic interferometry also introduces challenges resulting from laser and atomic beam divergences and the velocity averaging due to both longitudinal and transverse temperature, which this dissertation shows how to overcome. The work contained herein explores many stages of construction of an atomic gyro including the demonstration and characterization of two-dimensional laser cooling of atoms, stimulated Raman transitions, and Ramsey and spin echo interference. The implications for future research are also outlined and discussed.

THIS PAGE INTENTIONALLY LEFT BLANK

Table of Contents

List of Figures

THIS PAGE INTENTIONALLY LEFT BLANK

List of Tables

THIS PAGE INTENTIONALLY LEFT BLANK

List of Acronyms and Abbreviations

2D-MOT two-dimensional magneto-optical trap

AOM acousto-optic modulator

ASE amplified stimulated emission

DF Doppler-free

DS Doppler-sensitive

FWHM full width at half maximum

HWPs half-wave plates

INSs inertial navigation systems

LIA lock-in amplifier

MOT magneto-optical trap

NMR nuclear magnetic resonance

PBS polarizing beam-splitting cube

PM polarization-maintaining

PMT photomultiplier tube

QWP quarter-wave plate

RF radio frequency

RLG ring laser gyroscope

SAB signal above background

SATABS saturated absorption spectrum

SNR signal-to-noise ratio

THIS PAGE INTENTIONALLY LEFT BLANK

Acknowledgments

First and foremost I wish to gratefully acknowledge Dr. Frank Narducci for his help throughout this process. His expertise and seemingly inexhaustible patience have been critical to my completion of this dissertation. I would also like to thank Dr. Jeff Lee for his help not only explaining physics but also operating lab equipment and writing code. Dr. George Welch of Texas A&M University, Dr. Mark Havey of Old Dominion University, and Dr. Philippe Bouyer of the Institut d'Optique in Bordeaux, France have all visited the lab multiple times and I appreciate their questions, critiques, and insights. I would like to thank the Physics Departments of the U.S. Naval Academy and the Naval Postgraduate School for the opportunity to conduct this research in the first place. Finally, I would like to thank my wife Elizabeth and our daughters Claire and Lilly for their tireless support and understanding these last years.

THIS PAGE INTENTIONALLY LEFT BLANK

CHAPTER 1:
Introduction

The motivation for my research, from an application standpoint, is to aid in the development of a sensor that can replace a device called a ring laser gyroscope (RLG). RLGs are used in the inertial navigation systems (INSs) of Navy ships, submarines, and aircraft to assist in a type of navigation known as *dead reckoning*. This process involves starting with a known position and then inferring a later position based on known parameters such as heading and speed. When GPS signals are unreliable or unavailable, operators still need to know where they are not just for navigation, but for other reasons such as weapons employment. RLGs assist in inertial navigation due to their inherent sensitivity to rotation. Measurements from an RLG, when fed into navigational calculations along with heading and speed, provide a very accurate real-time position.

There are, however, limitations to this accuracy. Because every new position calculated by an INS uses the previous position as a starting point, errors accumulate quickly and improvements in accuracy pay huge dividends, especially at later times. The sensors' sensitivity depends on multiple factors, but one fundamental one is the effective mass of the photon, given by equating Einstein's mass-energy equivalence equation with the Planck-Einstein relation

$$
\begin{aligned}
E_{mass-energy\,equivalence} &= E_{Planck-Einstein}, \\
m_\gamma c^2 &= hf, \\
m_\gamma &= \frac{hf}{c^2},
\end{aligned}
\tag{1.1}
$$

where E is energy, m_γ is the effective photon mass, h is Planck's constant, f is the frequency of light, and c is the speed of light. Since the sensitivity scales with the mass, if one could increase the mass of the photon then there would be a requisite increase in sensitivity. This is essentially what this research entails—but rather than increasing the mass of the photon, we replace relatively light photons (with effective masses extracted from their wavelengths via the deBroglie equation, $\lambda_{deBroglie} = h/mv$) with relatively heavy atoms. The actual parameter that these sensors measure is a phase shift (in this example produced by a rotation

of magnitude Ω) given by [1], [2]

$$\Delta\phi = \frac{2m}{\hbar}\mathbf{\Omega} \cdot \mathbf{A}, \qquad (1.2)$$

where m is the mass of the atom or photon, $\hbar$ is the reduced Planck's constant (Planck's constant, h, divided by 2π), $\mathbf{\Omega}$ is the rotation vector, and $\mathbf{A}$ is the area enclosed by the interferometer. Rewriting Equation (1.2) in terms of the minimum detectable rotation magnitude, we can say that

$$\Omega_{min} = \frac{\hbar\Delta\phi_{min}}{2mA}. \qquad (1.3)$$

Written this way, we can see that not only is $\Omega_{min} \propto m$, but that as m gets very big, Ω_{min} gets very small. Also, whereas RLGs use matter in the form of beam splitters and mirrors to manipulate light waves, we use specially controlled laser light to manipulate matter waves of carefully prepared atoms. We invert the roles that matter and light play in an optical interferometer to make an *atom interferometer*.

Atom interferometers were initially developed in the 1990s to take advantage of their extreme sensitivity to acceleration and rotation [1]. Since the initial inception of atom interferometry with the launch of seminal papers in 1991 [3], [4], [5] and 1992 [6], the field has found use in a wide range of applications. Atom interferometry has been used successfully to confirm physical constants [7], test fundamental physics [8], and measure the effects of gravity and magnetic fields [9], [10]. It has also been used in applications as an inertial accelerometer/gyroscope since 2006 [11], [12], [13], [14]. Most of these examples use pulses of laser light to very precisely manipulate the atoms. Despite yielding impressive results, interferometers using pulses suffer from two inherent drawbacks [15]. First, these pulses are usually derived from passing continuous lasers through modulators that generate the pulses. These modulators require a significant amount of power, typically on the order of 1 watt of radio frequency power per pulse generator. A typical atom interfermeter will have several laser beams that need to be pulsed, thus this method requires a significant power budget. A second and more fundamental drawback to pulsed interferometers is a consequence of what happens to the atoms in between pulses. During these "dead times" no information about the acceleration or rotation of the interferometer can be determined—this can lead to measurement error.

Though less common, there have been atom interferometers based on continuous laser beams [16]. There are still many variations, however, within this subset of interferometers, namely atomic source generation and preparation and schemes to match the correct type of light with the specific element being used. My research, already lying within this small subset, involves unique variations in each regard. Specifically, the atomic source involves a transversely cold and longitudinally "cool" atom source (discussed in Sections 2.1 and 3.1), the atoms are put in the appropriate state via a novel optical pumping scheme (discussed in Sections 2.4 and 3.3), and the specific frequencies of laser light used to drive Raman resonances are generated in a novel way (discussed in Section 5.1.1). This experiment also uses rubidium 85 as the atom source, which plays into the aforementioned characteristics of the research. Many other atom interferometers use cesium or rubidium 87, but this experiment uses rubidium 85 for a few reasons. First, the wavelength of the primary transition involved in the research is matched to the operating frequency of many inexpensive and commonly available lasers (discussed in Section 2.2). Also, the novel scheme employed for the generation of the required frequencies of light for the optical pulses is most efficient with this particular isotope because its ground state splitting is smaller than that of other rubidium isotopes and cesium (Section 5.1.1).

The light in this research serves as an analog to physical mirrors and optics used in an RLG. With the mass of an atom being on the order of $10^4 MeV$ and the effective mass of a photon being on the order of a few electron volts, we have

$$
\begin{aligned}
\frac{\Delta\phi_{atom}}{\Delta\phi_{RLG}} &= \frac{m_{atom}}{m_\gamma}, \\
&= \frac{10^4 * 10^6 eV}{1 eV}, \\
\frac{\Delta\phi_{atom}}{\Delta\phi_{RLG}} &= 10^{10}.
\end{aligned}
\tag{1.4}
$$

Thus the relative mass difference between atoms and photons sets the bar as high as ten orders of magnitude in sensitivity increase. Even when the drawbacks of using atoms versus photons (such as not being able to recycle the atoms) are taken into account, one can still expect a sensitivity increase of three to four orders of magnitude [2].

The objective of my research is to improve and build upon existing research by means of

conceiving, assembling, and characterizing the most significant constituents of an atom interferometer that uses continuous light rather than pulsed lasers. This work is intended to contribute to making this technology more applicable for use as an operational navigational gyro rather than a laboratory instrument. The critical and novel change of using continuous light is promising for future gyros. It accumulates phase information continuously requires less equipment, thus lending itself more readily to the size, simplicity, and power consumption required for shipboard use.

In Chapter 2, I discuss laser cooling of atoms (which forms the basis for our atom source), how we prepare the atoms for the actual experiment, and how we take measurements. In Chapter 3, I discuss the experimental aspects of those concepts and characterize our experimental apparatus. I describe the theory of atom optics in Chapter 4 and specifically how the concept of reversing the roles of light and matter in an interferometer works, along with some ramifications of using continuous light. Chapter 5 then shows our results of putting those concepts to the test, with measurements of the different spectra and interference patterns involved with the many intermediate steps of constructing an atom interferometer. Finally, in Chapter 6, I discuss the relevance of what we've accomplished and the work that we envision for the future.

CHAPTER 2:
State Preparation: Theory

In any experiment, one always desires to maximize the signal while minimizing the noise. In this chapter, I will first discuss the theory of cooling and trapping of atoms since laser-cooled atoms form the basis of our atom source. These specially prepared atoms serve as the source of the signals that we wish to maximize. Prior to being measured as our signal, the atoms need to be specially prepared; this preparation step is described next.

2.1 Cooling and Trapping of Atoms

The foundation upon which this experiment rests is a continuous supply of cold atoms. These cold atoms are made in a region of the apparatus called a two-dimensional magneto-optical trap (2D-MOT). The cold atoms and the region where they are made are so fundamentally connected that the stream of cold atoms itself is typically referred to as the 2D-MOT or magneto-optical trap (MOT) for short. The actual process by which atoms are cooled in the MOT is called laser cooling. While perhaps seeming counterintuitive at first glance, this process is a result of three fundamental aspects of basic physics, namely the Planck-Einstein relation [17] and the conservation of momentum and energy.

Consider the simple two-level atom as depicted in Figure (2.1) with relevant energy levels (or states) which I will refer to as the ground and excited states ($|g\rangle$ and $|e\rangle$, respectively). The energy difference between the two states is ΔE. By the Planck-Einstein relation, we can rewrite this energy difference in terms of a frequency, $\Delta E = hf$ or $\Delta E = \hbar\omega_a$, where ω_a is the resonant atomic frequency associated with the transition between these two states. Now suppose this atom is illuminated by a laser of frequency ω_l. Bohr theory tells us that an incident photon having the correct frequency ($\Delta E/\hbar$) will be absorbed and the atom will be promoted to the excited state. In reality, the absorption of this photon from an applied laser field is probabilistic and depends on the difference between the laser frequency and the resonant atomic frequency, the spontaneous emission rate of the atom, and the strength of the coupling between the laser field and the atomic transition. This probability (steady-state,

zero velocity) is given by

$$P_{absorption} = \frac{\frac{1}{4}\Omega^2/\beta^2}{\frac{1}{2}\Omega^2/\beta^2 + 1 + \delta^2/\beta^2}, \tag{2.1}$$

where $\delta = \omega_l - \omega_a$ is the aforementioned frequency difference (known as *detuning*), 2β is the natural or spontaneous emission rate, and Ω here describes the strength of the coupling (and not a rotation as in Chapter 1) [18], [19]. Ω is known as the Rabi frequency and is given by

$$\Omega = \frac{2\left(\boldsymbol{\mu}^* \cdot \boldsymbol{\epsilon}_l\right)\mathcal{E}}{\hbar}, \tag{2.2}$$

where $\boldsymbol{\mu}^*$ is the complex conjugate of the dipole moment vector of the atom (a fundamental property of the atomic transition), $\boldsymbol{\epsilon}_l$ is the polarization vector of the laser, and $\mathcal{E}$ is the laser's electric field amplitude. The Rabi frequency is the rate at which a driven atom cycles between states. Even with a strongly-coupled, on-resonance laser, a given atom will still decay (mostly stimulated with occasional spontaneous emission) back to the ground state before being promoted back to the excited state.
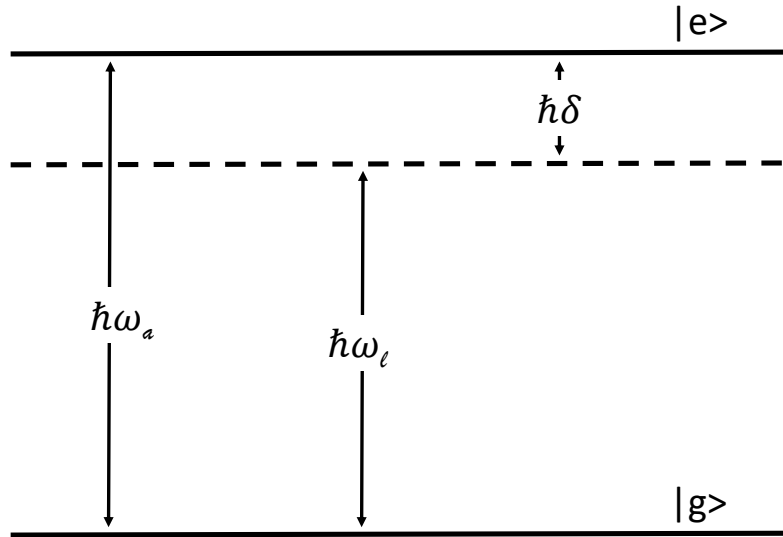
Figure 2.1: Energy diagram of a two-level atom with resonant atomic frequency ω_a being illuminated by a laser of frequency ω_l. The laser is *red-detuned* with its frequency ω_l below the resonant frequency ω_a such that $\delta < 0$.

In order to understand how this absorption and emission of photons is relevant to the laser cooling process we next consider the conservation of momentum. Every time a photon is absorbed from a laser field, in addition to being promoted to the excited state, the atom acquires a small amount of momentum from the photon, given by

$$p = \hbar k = \hbar \left(\frac{2\pi}{\lambda} \right) = \left(\frac{\hbar \omega_l}{c} \right), \tag{2.3}$$

where λ is the transition wavelength, k is the wave number associated with the wavelength, and c is the speed of light. The momentum transfer of a photon to a moving atom is very small; it is analogous to the momentum transfer of a ping pong ball thrown at a rolling bowling ball. The momentum of a single photon in this process (using a representative wavelength from our experiment) is $p = 2\pi\hbar/\lambda = 2\pi\hbar/780 \ nm = 8.5 \times 10^{-28} \ kg \ m \ s^{-1}$. For an atom from our experiment at thermal velocity we have $p = mv = \left(1.42 \times 10^{-25} \ kg \right) \left(170 \ m \ s^{-1} \right) = 2.4 \times 10^{-23} \ kg \ m \ s^{-1}$, or five orders of magnitude greater than the photon momentum. That being said, when millions of ping pong balls (photons), all coming from the same direction, hit the bowling ball (atom), there is a pronounced cumulative effect.

Of course, as the atom cycles between states it emits photons as well, each with its own associated momentum kick due to recoil. Whereas the incident photons have a cumulative effect due to their common incident direction, spontaneously emitted photons are ejected from the atom in random directions with the expected momentum kicks opposite to the direction of the ejected photons. Any cumulative momentum shift from spontaneous emission averages to zero. Thus the net effect of the absorption and emission process is for the atom to be pushed in the direction of laser propagation.

We can find the force associated with this effect by taking Equation (2.1) and multiplying by two additional factors [20]:

$$F = - \left(\hbar k \right) \left(2\beta \right) \left(P_{absorption} \right) = - \left(\hbar k \right) \left(2\beta \right) \left(\frac{\frac{1}{4}\Omega^2/\beta^2}{\frac{1}{2}\Omega^2/\beta^2 + 1 + \delta^2/\beta^2} \right). \tag{2.4}$$

In this case, the minus sign indicates that the direction of the force is opposite to the direction of the wave number (or direction of laser propagation) and is therefore a repulsive force. Note the three distinct factors contributing to the force acting on the atom correspond

to the momentum kick per photon, the spontaneous emission rate, and the probability of being in the excited state, respectively. This equation is not entirely correct, however, as it has no dependence on velocity; in its current form it only applies to stationary atoms. The real-world process of laser cooling involves atoms moving at thermal velocities with a Boltzmann distribution of velocities. To correct this equation for moving atoms we must introduce the Doppler shift associated with the motion, which modifies the frequency from ω_l to $\omega_l \pm kv$. Our (one-dimensional) force equation now becomes (assuming no saturation effects and two laser beams incident on the atom from opposite sides)

$$F = - \left(\hbar k \right) \left(2\beta \right) \left[\left(\frac{\frac{1}{4}\Omega^2/\beta^2}{\frac{1}{2}\Omega^2/\beta^2 + 1 + \left(\delta - kv \right)^2/\beta^2} \right) - \left(\frac{\frac{1}{4}\Omega^2/\beta^2}{\frac{1}{2}\Omega^2/\beta^2 + 1 + \left(\delta + kv \right)^2/\beta^2} \right) \right] \tag{2.5}$$

or, for small velocities,

$$F = - \left(\hbar k \right) \left(2\beta \right) \left[\left(\frac{\Omega^2}{\beta^2} \right) \left(\frac{k\delta/\beta^2}{\frac{1}{2}\Omega^2/\beta^2 + 1 + \delta^2/\beta^2} \right) \right] v, \tag{2.6}$$

with the key takeaway being that we now have $F \propto v$. See Figure (2.2) for a plot of this force versus detuning. Note that the laser must be red-detuned (tuned to a frequency below atomic resonance) for the laser to exert a force that opposes the motion of the atom.
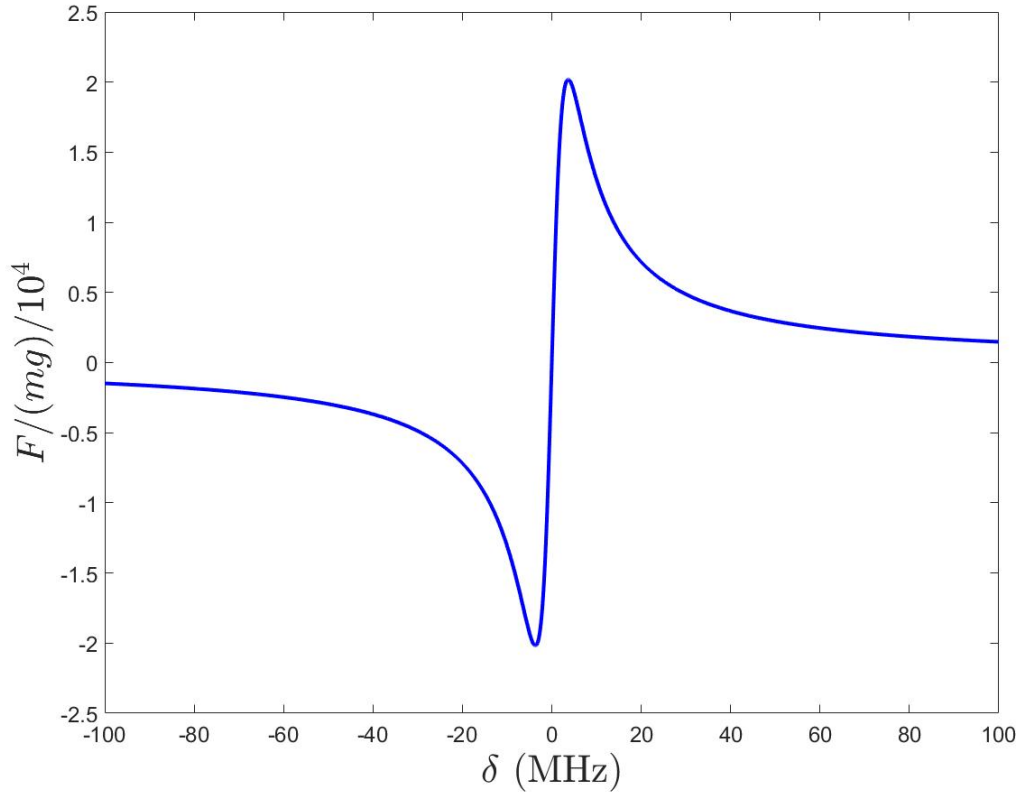
Figure 2.2: Force on an atom as a function of detuning. Only a red-detuned laser will exert a force that opposes the motion of the atom. Of note, $\Omega/\beta = 1$ and $v = 10 \ m/s$ (^{85}Rb atom used for modeling).

While we have established how the atoms are pushed by applied laser fields, we have not explained how they are actually cooled. To explain cooling, we must consider the conservation of energy. Referring back to Figure (2.1), notice the difference in frequencies between the laser and the atomic resonance. We discussed this difference in terms of detuning, but it also means that there is an energy difference between the photons that are absorbed (with $E = \hbar\omega_l$) and the photons that are emitted (with $E = \hbar\omega_a$). Now, we see another cumulative effect of the laser cooling process, which is that over many absorption and emission cycles the atom loses energy. The energy gained by an atom is $\hbar\left(\omega_l - \omega_a\right)$ per cycle; this amount is *negative* when $\omega_l < \omega_a$, and thus the atom cools (loses energy) when the laser is red-detuned. This energy loss translates to a loss of kinetic energy (e.g.,

9

motion) and thus temperature. Strictly speaking, slowing is the process of reducing the most-probable velocity (as just described) and cooling is the process of reducing the velocity spread (the slowing of many velocity groups causes them to "pile up" in a single velocity class, hence the reduction in velocity spread). The cumulative energy loss associated with the laser cooling process serves to reduce both metrics so we use the term laser cooling to describe both the slowing and cooling of atoms in the case of our experiment.

The process of slowing and cooling atoms as described above is referred to as an *optical molasses*. Since the pushing force of the lasers on the atoms is proportional to velocity, it is as if the atoms are moving in a thick, viscous medium. Mathematically, this looks like a damped harmonic oscillator

$$m\ddot{x} + b\dot{x} = 0, \tag{2.7}$$

where the resistive force exerted by the lasers is $-b\dot{x}$ (b is the large term in front of v in Equation (2.6)). With two lasers pushing on an atom from different directions, when an atom has a velocity in a given direction it feels a force that is stronger from the laser beam opposing its motion. Because of the Doppler shift and the fact that the laser is tuned below resonance, the laser beam opposing the motion of the atom is closer to resonance and hence exerts a strong force on the atom. So if an atom starts to move toward a given laser it is immediately pushed and slowed. While these beams do indeed slow and cool the atoms, they do not localize the atoms in a particular location since the atoms feel no force once velocity goes to zero independent of position.

The localization comes from the "magneto" part of the MOT. Permanent magnets are oriented in an anti-Helmholtz configuration around the optical molasses and exert a force on the atoms that is proportional to position rather than velocity. The mechanism that produces this force is a Zeeman shift in the magnetically sensitive sublevels of the atom caused by the field which increases linearly with distance from the center of the trap [21]. In order to make a MOT, the cooling light needs to be circularly polarized, with beams that have right-handed ($\hat{\boldsymbol{\sigma}}^- \equiv \hat{\boldsymbol{x}} - i\hat{\boldsymbol{y}}$) and left-handed ($\hat{\boldsymbol{\sigma}}^+ \equiv \hat{\boldsymbol{x}} + i\hat{\boldsymbol{y}}$) circular polarization. Due to selection rules, $\hat{\boldsymbol{\sigma}}^+$ light only couples to the $\Delta m_F = +1$ sublevel and $\hat{\boldsymbol{\sigma}}^-$ light only couples to the $\Delta m_F = -1$ sublevel. As depicted in Figure (2.3), the further from the center that an atom moves, the greater the Zeeman shift, and the closer the atomic resonance shifts toward the red-detuned laser. An atom to the left of center feels a force from the $\hat{\boldsymbol{\sigma}}^+$

beam since the $\hat{\sigma}^+$ beam is closer (in energy/frequency) to its resonant magnetic sublevel. Similarly, an atom to the right of center feels a force from the $\hat{\sigma}^-$ beam since the $\hat{\sigma}^-$ beam is closer to its resonant magnetic sublevel. Thus we are left with the same effect as an atom moving toward the laser (i.e., a push). Building upon our damped harmonic oscillator equation (Equation 2.7), we can now add another term, so that

$$m\ddot{x} + b\dot{x} + Kx = 0, \tag{2.8}$$

with this resistive force given by the Hookean term $-Kx$ where [20]

$$K = \left(\frac{2\hbar k}{m}\right)\left(\frac{\Omega^2}{\beta^2}\right)\left(\frac{\delta}{(1 + \delta^2/\beta^2)^2}\right). \tag{2.9}$$

This forms a potential well to concentrate the atoms into a small region. The MOT is essentially a damped harmonic oscillator with velocity-dependent damping and position-dependent confining.
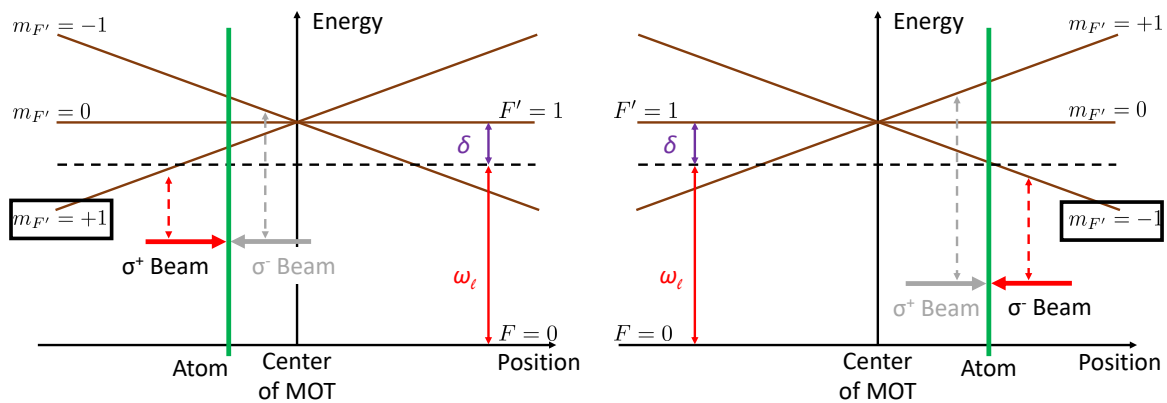
Figure 2.3: One-dimensional depiction of the MOT with the center of the inhomogeneous magnetic field coincident with the center of the trap (left). An atom to the left of center feels a force from the $\hat{\sigma}^+$ beam. An atom to the right of center feels a force from the $\hat{\sigma}^-$ beam (right).

Previous work actually began in a three-dimensional configuration [22] and moved to a two-dimensional configuration a few years later [23]. In this experiment, this double-damped harmonic oscillator is two-dimensional, resulting in a cold atom beam that propagates through a pinhole to a vacuum chamber. The MOT and vacuum chamber (along with the

other major components of the experiment) are depicted in Figure (2.4). At this point, the foundation is laid and the experiment begins.
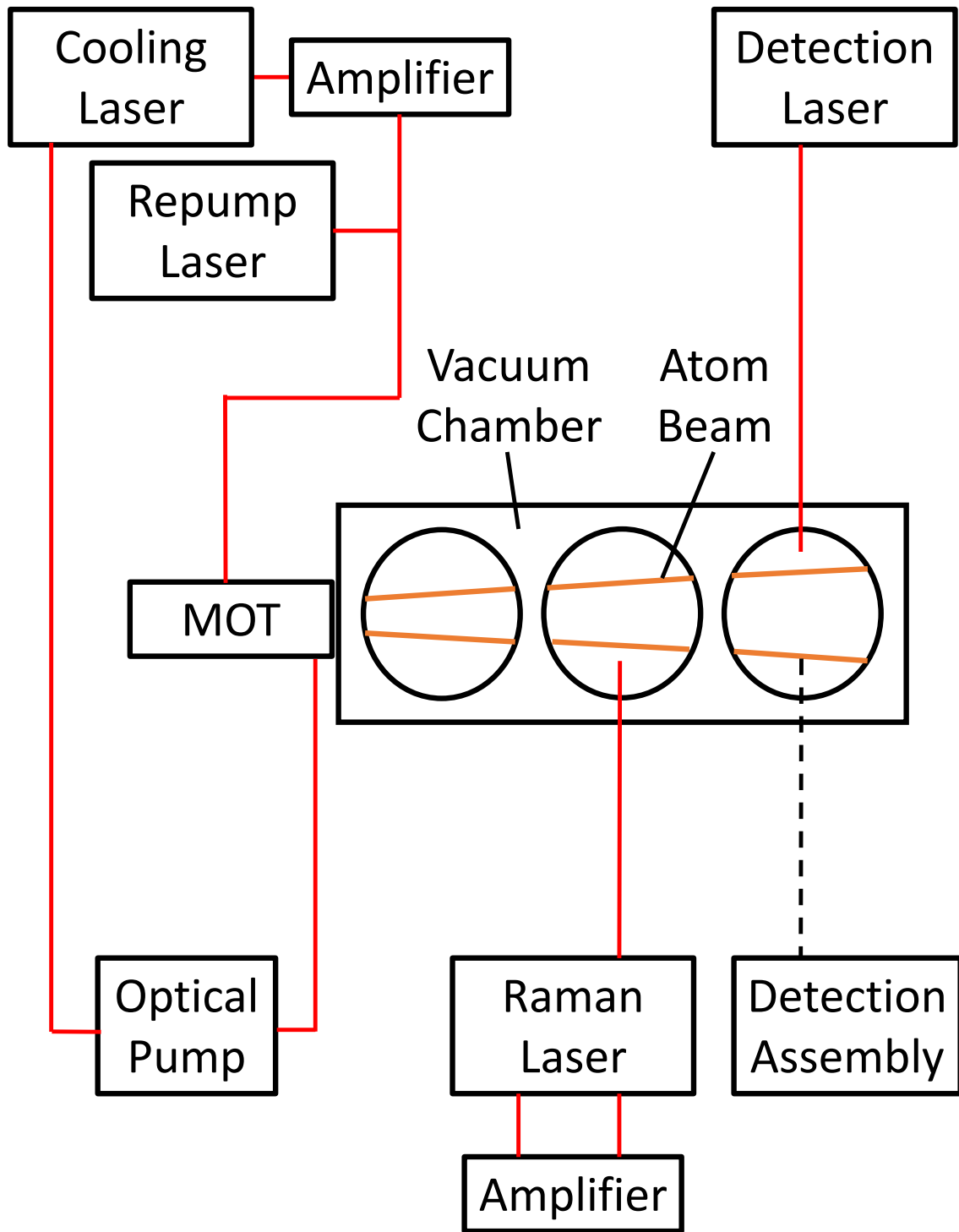
Figure 2.4: Depiction of the experiment (some items have not been discussed yet; diagram is intended for use as a future reference). Red lines indicate laser beams; dashed line indicates digital signal acquisition.

2.2 Repumping

The basic theory described in the previous section used a simple two-level atom model. The actual atom used in this experiment is ^{85}Rb—which is very much *not* a two-level atom. Figure (2.5) depicts the two relevant levels which are $5S_{1/2}$ and $5P_{3/2}$. This transition is known as the D2 transition of ^{85}Rb. The left side of Figure (2.5) depicts *fine structure*, which is determined by the addition of orbital angular momentum $\boldsymbol{L}$ and spin angular momentum $\boldsymbol{S}$ ($\boldsymbol{J} = \boldsymbol{L} + \boldsymbol{S}$). The right side of Figure (2.5) depicts the addition of this total electronic angular momentum $\boldsymbol{J}$ with the total nuclear angular momentum $\boldsymbol{I}$ and is known as *hyperfine structure* ($\boldsymbol{F} = \boldsymbol{J} + \boldsymbol{I}$). The laser cooling process used in this experiment relies on atomic transitions between the two hyperfine levels $F = 3$ and $F' = 4$ (the prime nomenclature indicates an excited state) resident within the fine levels $5S_{1/2}$ and $5P_{3/2}$. Once we consider the multiple hyperfine levels, the simple, two-level atom discussed earlier gets more complicated.
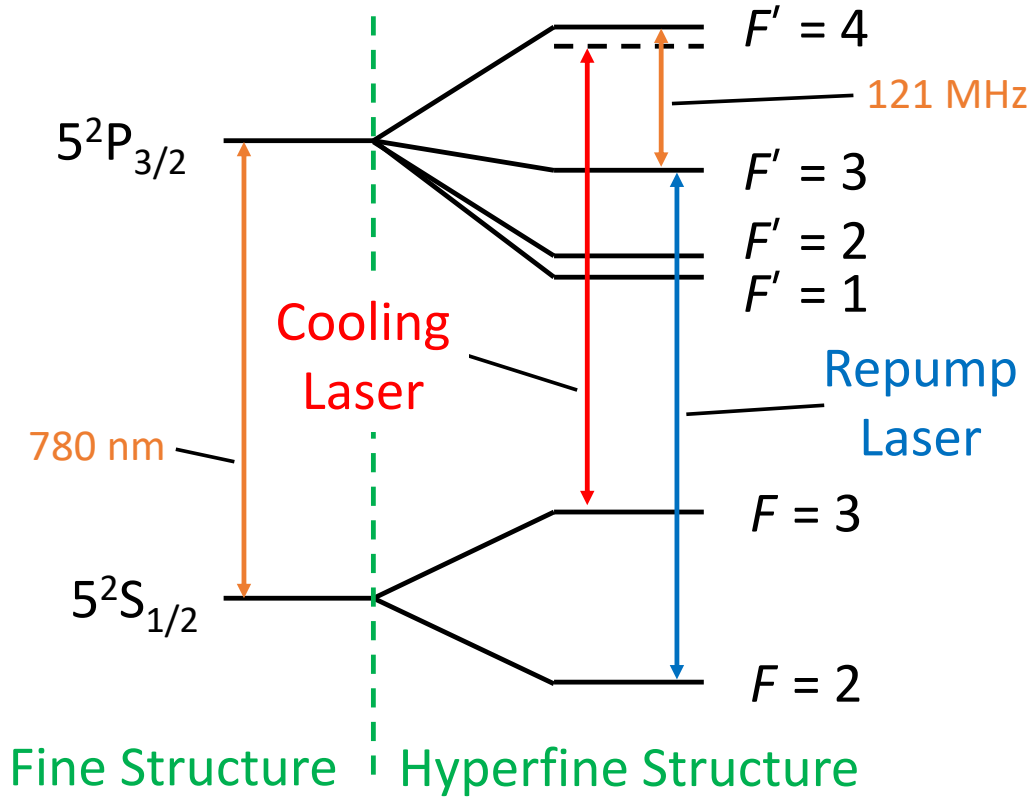
Figure 2.5: The D2 transition of Rubidium 85 (not to scale). The nomenclature of the fine levels comes from the nuclear magnetic resonance (NMR) community $(N^{2S+1}L_J)$.

One complication that arises due to the increased atomic structure complexity is that a laser tuned to excite atoms from $F = 3$ to $F' = 4$ has a nonzero probability of off-resonantly exciting atoms to $F' = 3$ instead. In Section 2.1, Equation (2.1) described the probability of absorption and hence, the probability of excitation (since the equation was for a simple closed, two-level system). Specifically, with a laser tuned close to the $F = 3$ to the $F' = 4$ transition, the probability of exciting into the $F' = 3$ state is

$$P_{excitation\ to\ F'=3} = \frac{\frac{1}{4}\Omega^2/\beta^2}{\frac{1}{2}\Omega^2/\beta^2 + 1 + \delta^2/\beta^2}. \tag{2.10}$$

In rubidium the $F' = 3$ and $F' = 4$ levels are separated by $121\ MHz$ and so $\delta =$

$2\pi \ (121 \ MHz)$. Meanwhile, the D2 transition has a decay rate of $2\beta = 2\pi \ (6.07 \ MHz)$ [24]. Finally, a typical value of Ω/β in our experiment is around 5, so $\Omega/\beta \ll \delta/\beta$ in this context. Thus, using the large-detuning limit, the probability of excitation reduces to

$$
\begin{aligned}
P_{excitation \ to \ F'=3} &\approx \frac{1}{\delta^2/\beta^2}, \\
&\approx \frac{1}{(2\pi \ (121 \ MHz))^2 / (\pi \ (6.07 \ MHz))^2}, \\
P_{excitation \ to \ F'=3} &\approx \frac{1}{1600}.
\end{aligned}
\tag{2.11}
$$

Equation (2.11) means that a laser tuned to excite atoms from $F = 3$ to $F' = 4$ has about a 1/1600 chance of accidentally exciting an atom to $F' = 3$ instead. While selection rules prohibit spontaneous decay from $F' = 4$ to $F = 2$, they do not prohibit spontaneous decay from $F' = 3$ to $F = 2$. This may sound like nothing to worry about, but recall that it takes millions of photons to cool atoms. This calculation shows that cooling would stop after around 1600 cycles because, once an atom falls into the $F = 2$ state, cooling "catastrophically" stops (no graceful degradation or simple attenuation). The ratio of decay into these two ground states can be calculated by looking at the dipole matrix elements for the transitions between the various magnetic sublevels and is known as the *branching ratio* (see the appendix for detailed calculations). About half of the atoms that get promoted to $F' = 3$ end up in $F = 2$. Once an atom drops into the $F = 2$ state, cooling for that atom stops since the cooling laser is now out of resonance with the atom. Without an intervention, the net result of this effect is a catastrophic cessation of the cooling process. The solution to this problem is another laser referred to as the *repump laser*. The most straightforward tuning of this laser would be $F = 2$ to $F' = 4$ so that atoms would be directly reinserted into the cooling transition of $F = 3$ to $F' = 4$. Unfortunately, as already mentioned, selection rules prohibit this transition (ΔF must be 0 or ± 1). Therefore the repump laser is tuned to the allowed transition of $F = 2$ to $F' = 3$ so that each atom is essentially given another 50-50 chance to decay into the desired state of $F = 3$. It is through this mechanism that the repump laser ensures the cooling process can continue indefinitely (that is to say the sample reaches its fundamental temperature limit, but the actual temperature is maintained indefinitely).

16

2.3 Detection

Everything in our experiment—ranging from characterization of our atomic source to final rotation measurements—depends on measuring the number of atoms that reside in the $F = 3$ state. Here, we describe our detection process. As depicted in Figure (2.6), the atoms are measured with yet another laser (referred to as the *detection laser*) and a photomultiplier tube (PMT). As we shall see later in Section 4.1, the two relevant states for our experiments are the two hyperfine ground states $F = 2$ and $F = 3$. Ideally we would measure the number of atoms residing in each, but the $F = 2$ state is experimentally difficult to measure. Fortunately, we can get enough information by measuring atoms in the $F = 3$ state only. A detection laser tuned to the $F = 3$ to $F' = 4$ transition will do precisely that. Any atom in the $F = 3$ state which is illuminated by this light is excited to the $F' = 4$ state and then spontaneously decays back to the $F = 3$ state after a short time (minus the small number of atoms that excite to $F' = 3$ and decay to $F = 2$). Any atom not initially in the $F = 3$ state passes through the detection laser beam without scattering any light. The way that this detection scheme measures the number of atoms in the $F = 3$ state is by detecting the spontaneous emission of photons from the atoms as they decay from $F' = 4$ back down to $F = 3$; off-resonant excitation into $F' = 4$ by stray resonant light will also result in detected photons as the atoms decay, but that effect is mitigated by the design of our apparatus (beam blocks, light-absorbing covers on exposed windows, etc.). The detection scheme, placed at the far end of the apparatus, specifically has the laser exciting the atoms and the PMT measuring a fraction of the spontaneously emitted photons. However, the cooling and repumping process leaves *virtually* all of the atoms in the $F = 3$ state (modeling shows only a small fraction remain in $F = 2$ after atoms pass through beams and begin to decay). In order to measure how the experiment is affecting the atoms, they must be put *back* in the other relevant ($F = 2$) state prior to entering the vacuum chamber; this process will be described in the next section.
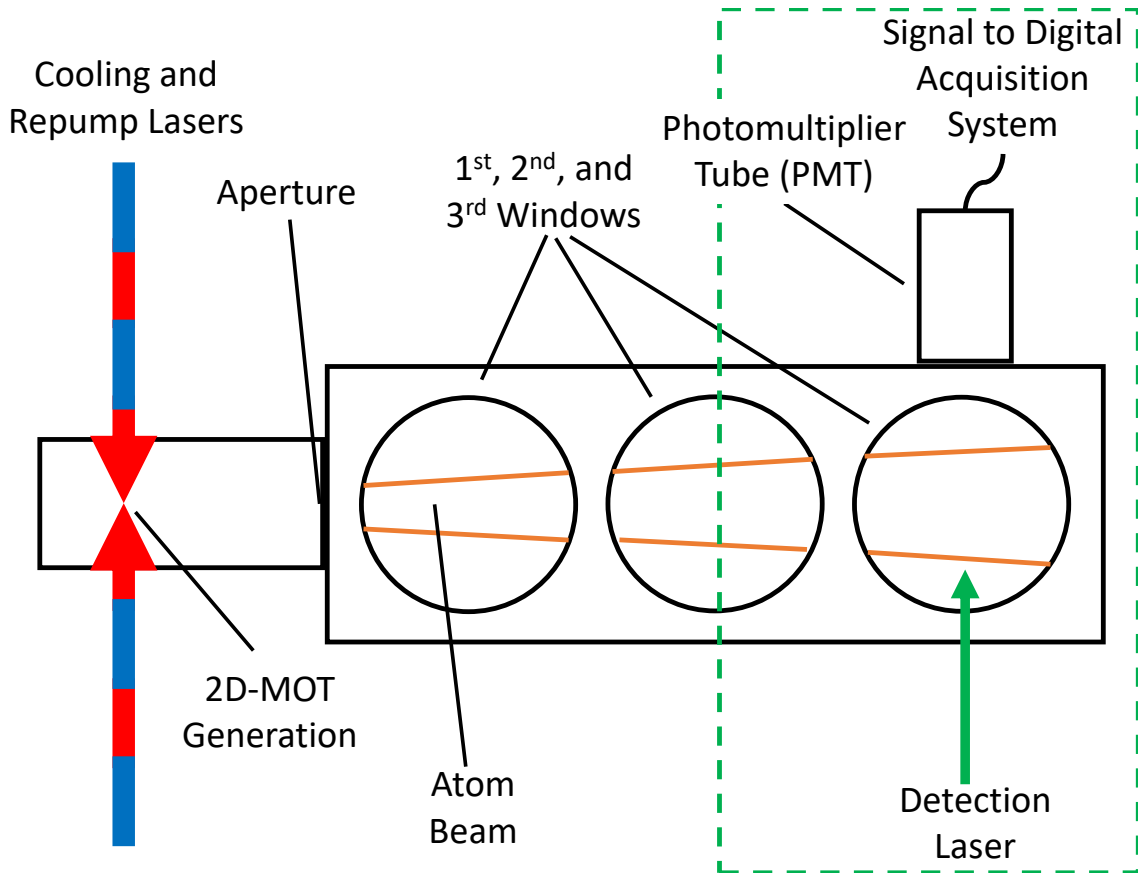
Figure 2.6: Experimental apparatus with emphasis (dashed box) on the detection scheme.

2.4 Optical Pumping

The previous section described how to use the repump laser to keep atoms out of the $F = 2$ state to ensure the cooling process would continue. However, as atoms leave the MOT region for the interferometry region, we need to ensure that they are all placed in the $F = 2$ state so that we can conduct the experiment and make measurements. The process of using a laser to move atoms from the $F = 3$ to the $F = 2$ state is referred to as *optical pumping*. We could theoretically just use some light from the cooling laser since we know that, in the absence of repumping, the atoms that are excited from $F = 3$ to $F' = 4$ will eventually end up in the $F = 2$ state, which is precisely where we now want them. Each atom would have to be pumped, on average, around 1600 times to get there. There is a

problem, however, with this method. As depicted in Figures (2.7) and (2.8), the atoms leave the MOT region and travel in the dark (no laser illumination) through an aperture before entering the interferometry region.
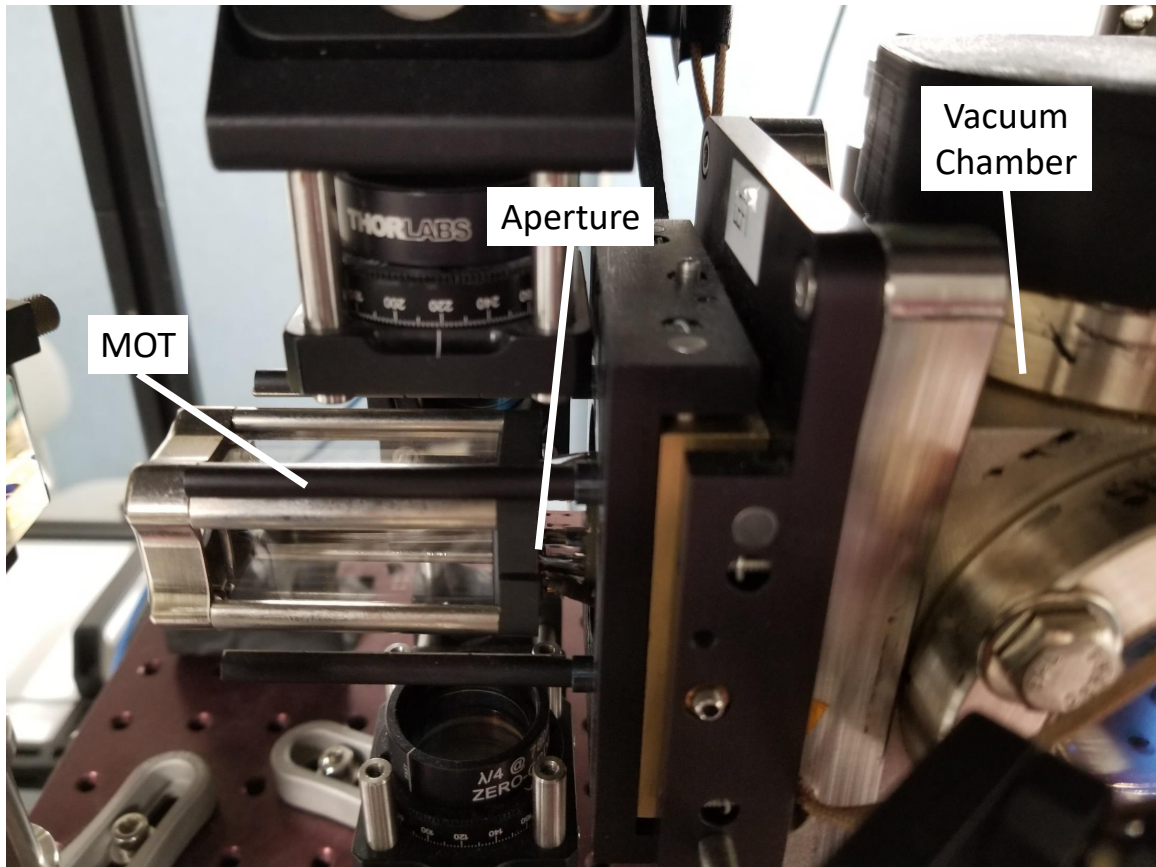
Figure 2.7: Photograph of the MOT and the vacuum chamber.
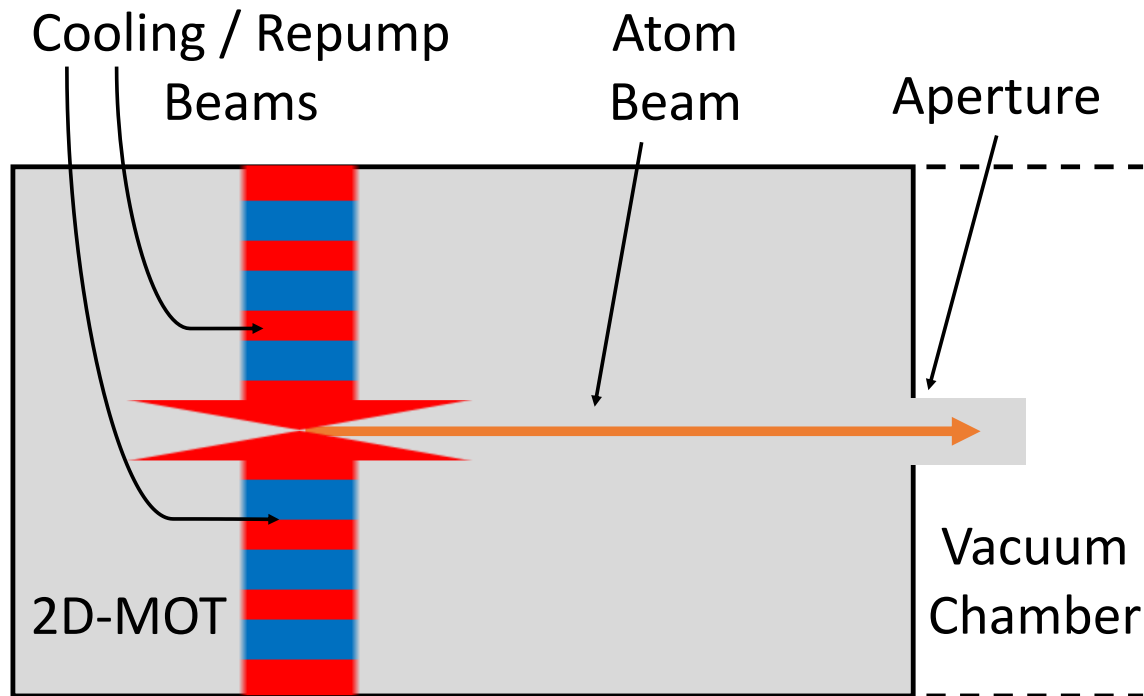
Figure 2.8: Depiction of atom beam and aperture separating the MOT region from the vacuum chamber.

However, there is a catch—the momentum kick discussed in Section 2.1 is also present during the optical pumping process. In this proposed optical pumping scheme, every atom would, on average, receive 1600 momentum kicks (of $\hbar k$) before dropping into the $F = 2$ state. The effect from an optical pumping beam tuned as described is a net push on the atom beam as it makes its way toward the aperture. Instead of being advantageous (as in laser cooling where the kicks "push" the atom to a standstill) these kicks actually push and *deflect* the atom beam enough that it doesn't actually make it through the aperture as depicted in Figure (2.9). From a detection standpoint, this looks the same as very effective optical pumping—the signal is zero. One could easily attribute the lack of signal to all of the atoms being in the $F = 2$ state. Only during follow-on steps in the experiment does it become clear that something is amiss. This is precisely how the sequence of events played out in

our laboratory (see Section 3.3.1). This phenomenon was discovered *experimentally* and only later confirmed by theory. One might wonder, why not negate any effects of angular displacement by filling up the entire MOT region with cooling light? Unfortunately, the placement of metal and glass in the actual physical apparatus (see Figure [2.10]) precludes us from doing that. We are constrained by the physical dimensions to generate the atom beam at a non-negligible distance from the aperture and vacuum chamber.
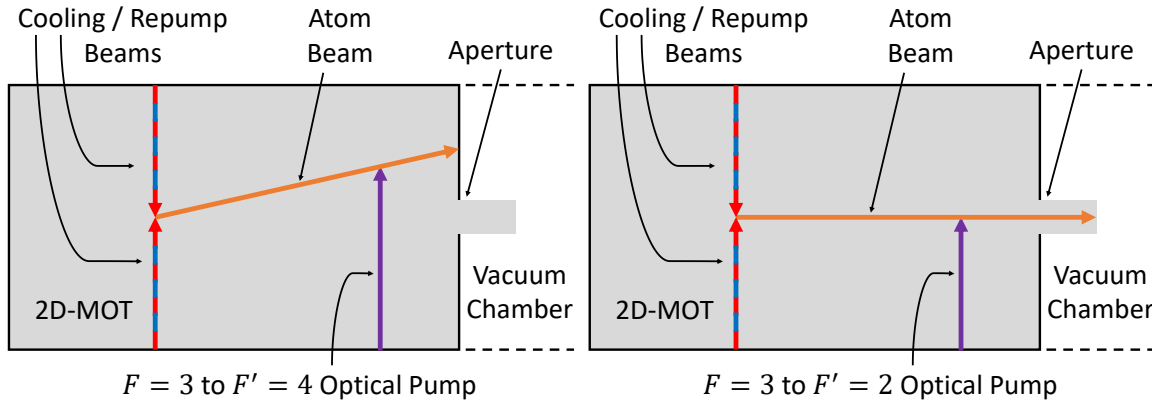
Figure 2.9: Displaced atom beam missing the aperture and failing to propagate into the vacuum chamber (left). Atom beam passing through the aperture after being optically pumped (right).

Fortunately, there are other ways to pump the atoms into the $F = 2$ state. Due to selection rules, atoms in any of the other excited states ($F' = 1, 2, 3$) can also spontaneously decay into the $F = 2$ state. By those same selection rules, optical pumping from $F = 3$ to $F' = 1$ is prohibited. We know that atoms in $F' = 3$ will decay into $F = 3$ and $F = 2$ at an equal rate (recall the branching ratio discussion in Section 2.2). If the atom beam is illuminated with $F = 3$ to $F' = 3$ light the atoms will quickly accumulate in the $F = 2$ state (without having to wait 1600 spontaneous lifetimes for off-resonant excitation to take place), so this transition is a viable candidate for optical pumping. However, atoms in the $F' = 2$ state will also decay into the same two ground states (see the appendix for a detailed calculation of the branching ratio). Rather than having a roughly even branching ratio, decay from $F' = 2$ is four times stronger into $F = 2$ than into $F = 3$. So, $F' = 3$ and $F' = 2$ seem likely to both be acceptable candidates for the optical pumping state. In the next chapter I will discuss the experimental measurements that led to our eventual selection of the $F = 3$ to $F' = 2$ transition as the preferred choice for the experiment's optical pumping transition.
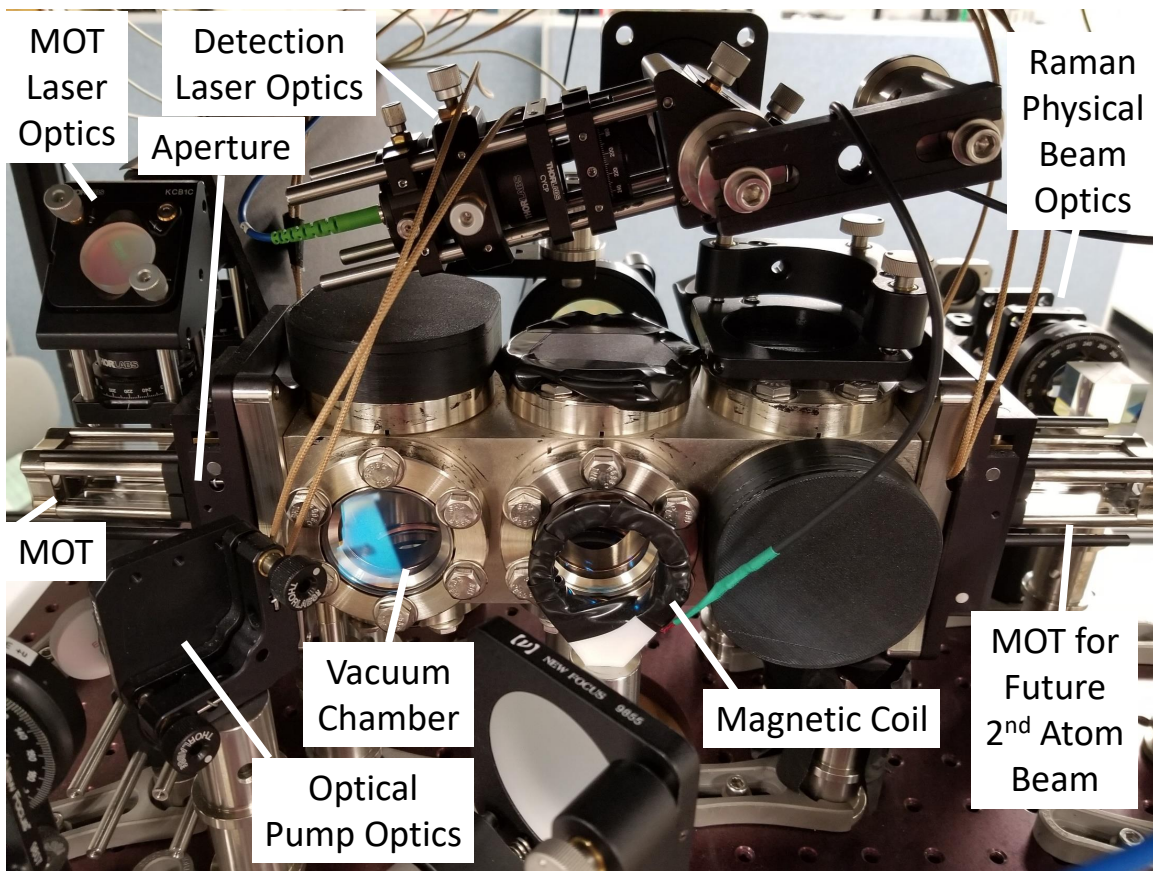
Figure 2.10: Photograph of the vacuum chamber (some items have not been discussed yet; photograph is intended for use as a future reference).

CHAPTER 3:
State Preparation: Experiment

Now that the theoretical groundwork has been laid, I will discuss how we handled state preparation in the lab. The three major components are the MOT, detection, and optical pumping.

3.1 Cooling and Trapping of Atoms

The theoretical discussions of cooling and trapping atoms along with the repumping of atoms all lead to the realization of a 2D-MOT in the lab. We are interested in characterizing the atomic beam as atoms travel through the experimental apparatus. There are three main characterization parameters that we are interested in measuring: signal optimization, atom beam divergence (size), and atom beam velocity profile. The first item sets our upper end for signal detection and the latter two are critical for determining how to construct our Raman laser pulses (to be discussed in Section 4.3).

3.1.1 Atomic Fluorescence Optimization

Parts of this section are adapted from [25], an accepted manuscript of an article published by Taylor & Francis in Journal of Modern Optics on 12 November 2019, available online: https://www.tandfonline.com/doi/full/10.1080/09500340.2019.1688410.

Our experiment begins with an apparatus (recall Figure 2.6) that produces a 2D-MOT. Light from two distributed feedback lasers (Eagleyard EYP-DFB-0780-00080-1500-TOC03) is split into four orthogonal beams which illuminate a small chamber filled with gaseous rubidium atoms in their natural isotopic abundance. The laser light in each beam is a mixture of light from the cooling and repump lasers (described in Sections 2.1 and 2.2). The atoms are neither confined in the third dimension nor are they slowed, but the geometry of the aperture leading to the main experiment's differentially-pumped vacuum chamber selects a subset of velocity classes below typical thermal velocities; the (radial) cooling time (proportional to the downrange travel distance inside the MOT beams) determines the transverse velocity. The vacuum chamber is an approximately 9-in long stainless steel

chamber featuring three $2.75 - in$ ConFlat$^{\text{TM}}$ flange sight windows along each longitudinal edge, pumped to a typical pressure of $1.2 \times 10^{-9} \, Torr$. This vacuum chamber is where the atom beam is subjected to the various types of light associated with different aspects of the experiment. As noted, every laser used in this experiment is continuous, i.e., no pulses are required or used.

We used the fluorescence from the atomic beam itself to optimize parameters of the experiment. As depicted in Figure (3.1), the signal is a Lorentzian, and we are concerned with the signal itself and the background upon which it sits (in the figure the signal is superimposed on the detection laser saturated absorption spectrum (SATABS) as a frequency reference). In Section 3.2, I will describe in detail how we make this signal; what the atomic beam fluorescence signal represents is the number of atoms in the experiment. It is important to note that all measurements are based on this number and will be a fraction of this signal. Thus, it is important to optimize the number of atoms.
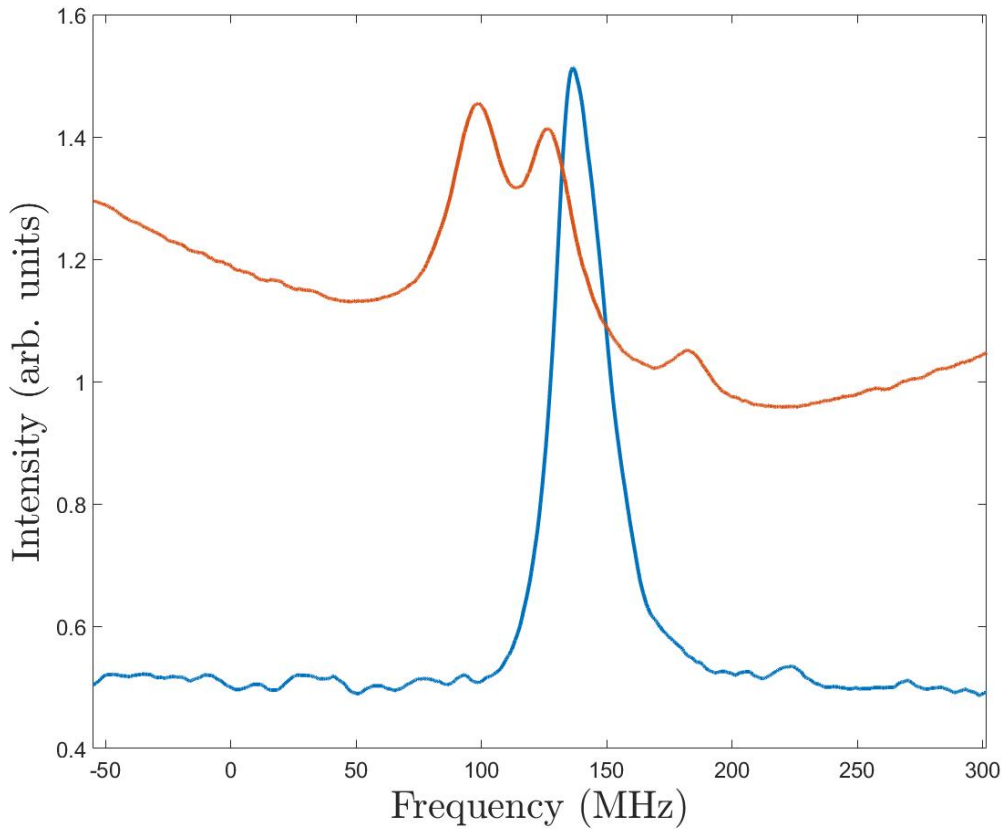
Figure 3.1: Lorentzian fluorescence peak from the atomic beam (blue) superimposed on the detection laser SATABS (orange).

Having established a working 2D-MOT, the first immediate "dial" to adjust is the power of the cooling and repump lasers. We expect the number of atoms in the MOT and hence atomic beam fluorescence to increase up to a point as the laser powers are increased. The point at which it ceases to increase corresponds to the saturation point of the cooling process. Recall from Equation (2.1) that the probability of absorption increases with the strength of the coupling Ω (the Rabi frequency) between the lasers and the atoms (where $\Omega \propto \mathcal{E}$, the laser's electric field amplitude). As Ω increases this probability goes to one half. Additionally, increasing the power of the cooling and repump lasers can lead to scattering in the chamber which leads to a higher background signal. Experimentally, this all looks like an increasing fluorescence signal sitting on a steady (or slightly increasing) background

turning into a steady (or slightly increasing) fluorescence signal sitting on an increasing background (signal above background (SAB)). The aim is to maximize the signal-to-noise ratio (SNR), which in the context of our experiment is really the amplitude of the Lorentzian peak above the background, divided by the background (with the final metric referred to as the signal above background).

As depicted in Figures (3.2) and (3.3), these values were experimentally determined by individually and incrementally increasing the laser powers and noting the point at which the signal above background ceased to appreciably increase. For each laser the measurements were made while increasing the power and then again while decreasing the power in order to gain more data points and check reproducibility; for the repump laser this process was repeated a second time due to a less (initially) well-defined saturation point. Of note, we fed the output of the cooling laser through an amplifier (Thorlabs TPA780P20 Tapered Amplifier mounted on a Thorlabs LDC2500B Tapered Amplifier Controller) to get to its signal saturation point. We used a similar process to determine the optimal current setting for the *getter* (our source of Rubidium). As with laser power, Table (3.1) shows that increasing getter current increases the signal up to a point where it saturates. The optimal setting is just at the saturation point.

Table 3.1: Atomic beam fluorescence vs. getter current; this data was used to determine the optimal getter current ($2.4\ A$).

Current [A]	SAB / B	SNR
2.1	.360 / 0.368	1.0
2.2	.584 / 0.368	1.6
2.3	.624 / 0.360	1.7
2.4	1.28 / 0.380	3.4
2.5	1.06 / 0.380	2.8
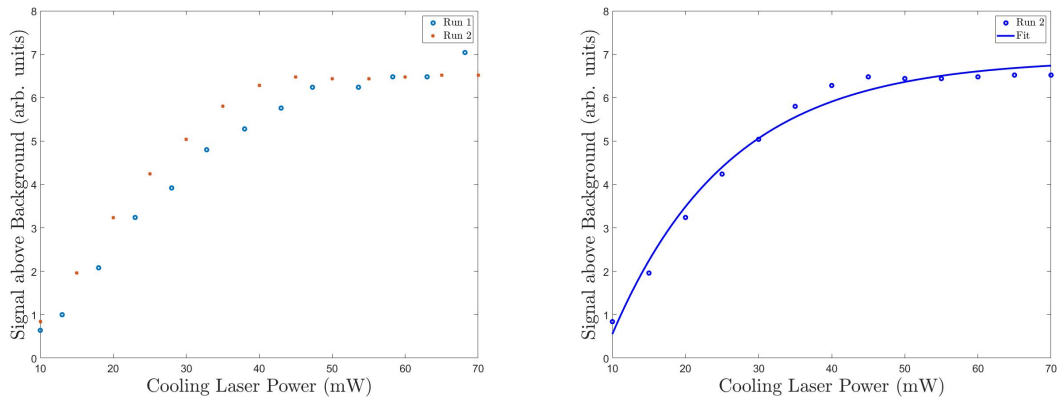
Figure 3.2: Atomic beam fluorescence vs cooling laser power (data points from two runs); this data was used to determine the optimal cooling laser power (left). Second data run fit to the exponential $Signal = A\left(1 - \exp\left(-B * Power\right)\right) + C$ where $A = 11.79$, $B = 16.08\ \left[mW\right]^{-1}$, and $C = 4.90$ (right).
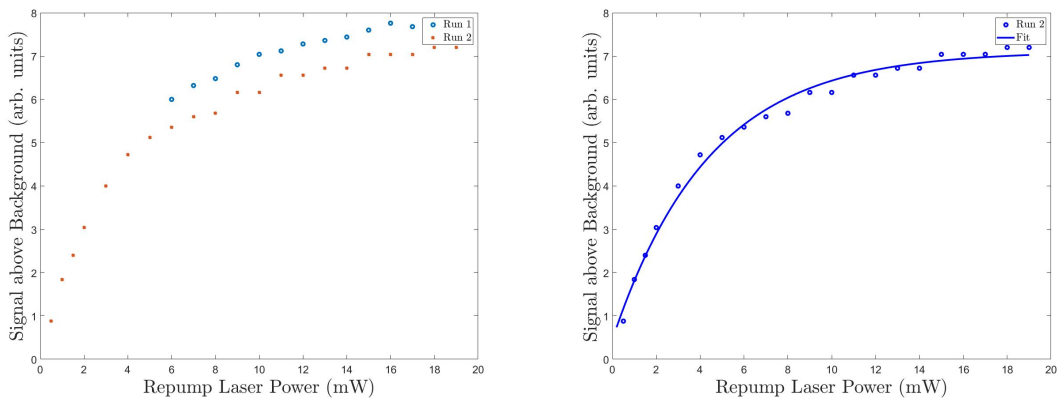
Figure 3.3: (Atomic beam fluorescence vs repump laser power (data points from two runs); this data was used to determine the optimal repump laser power (left). Second data run fit to the exponential $Signal = A\left(1 - \exp\left(-B * Power\right)\right) + C$ where $A = 6.65$, $B = 4.38\ \left[mW\right]^{-1}$, and $C = 0.45$ (right).

3.1.2 Atom Beam Divergence

This section is adapted from [25], an accepted manuscript of an article published by Taylor & Francis in Journal of Modern Optics on 12 November 2019, available online: https://www.tandfonline.com/doi/full/10.1080/09500340.2019.1688410.

The most immediate impact of atomic beam divergence is that it determines the size of the atomic beam at the different windows in the vacuum chamber. We need to know its size if we are to effectively optimize the size of the detection laser beam as it crosses the atomic beam in front of the PMT, for example. (Atom beam divergence has additional ramifications that will be discussed in detail in Section 4.6.) We measured the divergence of the atom beam by measuring the atomic beam width at the first window of the vacuum chamber in the following way. As depicted in Figure (3.4), we took a photograph of the atomic beam fluorescence with a camera (Mightex CCE-B013-U USB camera) and recorded the image as a .jpg file. The fluorescence was generated one vertical slice at a time using a laser beam shining vertically down through the chamber to excite the atoms. After each photo, the laser was translated down the long axis of the chamber by one laser beam width at which point we took another photo. We combined the slice photos into one image to show a virtual atom beam propagating and diverging down the chamber. Finally, we analyzed a vertical slice of the image using MATLAB. The MATLAB code fit the intensity of this slice to a Gaussian function; we used the full width at half maximum (FWHM) from the Gaussian fit and the known distance from the beam aperture of known diameter to calculate an atom beam (half-angle) divergence of $56\ mrad$. This value is consistent with preliminary rough measurements we made with a translating on-resonance probe in the second window of the vacuum chamber.
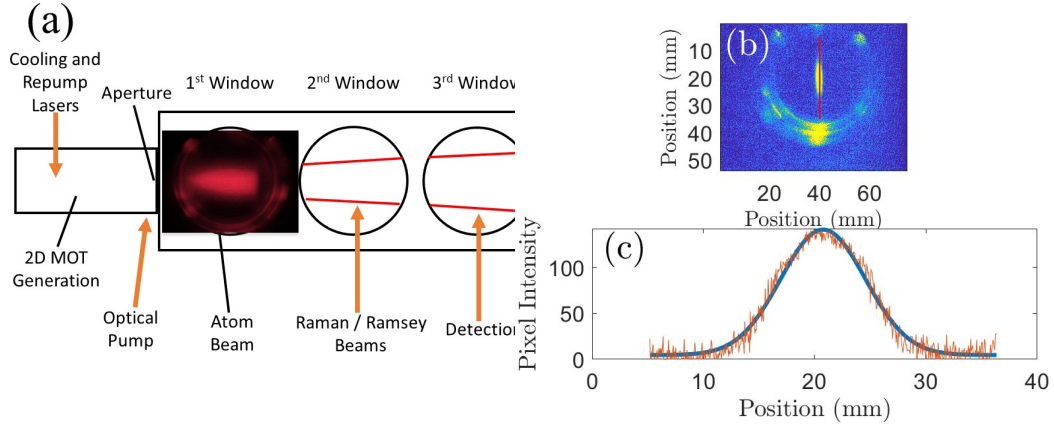
Figure 3.4: Depiction of the experimental apparatus with photo of atom beam located in the first vacuum window (a). Photo of atomic beam taken with a thin on-resonance laser beam (b). The red line shows the part of the photo that was then used to generate the intensity plot shown in (c), which consists of the data in brown and a Gaussian fit in blue.

3.1.3 Velocity of Atoms

Generally, the atomic beam fluorescence is measured (as in Section 3.1.1) with a detection laser that is orthogonal to the atom beam. This is done to avoid any Doppler broadening of the resonant light by velocity components of the atomic motion along the laser beam direction. However, we can intentionally orient the detection laser anti-parallel to the atomic motion to detect a Doppler-broadened peak and from that extract a velocity profile. (The peak will not only be Doppler-shifted, it will also be broadened because the beam is not monoenergetic and instead contains many different velocity classes.) Now, the frequency of the peak will not be exactly at the $F = 3$ to $F' = 4$ transition but rather Doppler shifted proportionally to the speed of the atoms—this is the basis for our first velocity measurement of the atom beam. Experimentally, this means we measure the frequency difference between the fluorescence peak and the SATABS in the transverse *and* longitudinal directions then use the difference as the basis of our calculations (ideally, the shift would be zero in the transverse case but is not due to slight misalignments in beams and, more importantly, atomic beam divergence, etc.). Figures (3.5(left)) and (3.5(right)) show the frequency shifts in the transverse and longitudinal directions, respectively. The data were fit to the function $\frac{2v^3}{v_{mp}^4}e^{-v^2/v_{mp}^2}$ from which $v_{mp} = 1.4 \ m/s$ was extracted [26]. This is a difficult and not

29

very reliable measurement to make due to the relatively slow speed of the atoms; based on the resolution of the experiment and previous measurements we used an estimated most probable velocity v_{mp} on the order of $10\ m/s$ in our numerical model until we could make a better measurement.
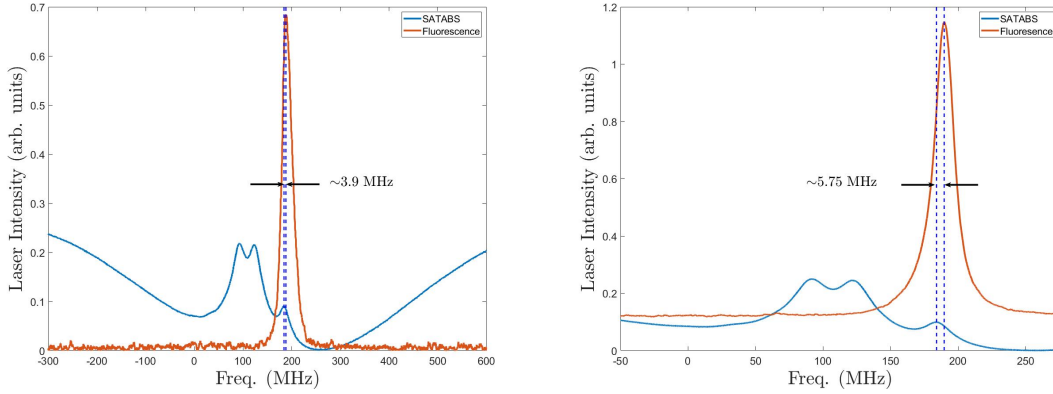
Figure 3.5: Frequency difference between fluorescence and SATABS in the transverse direction (left). Frequency difference between fluorescence and SATABS in the longitudinal direction (right). The difference was used to calculate a most probable atomic beam velocity of $\sim 1.4\ m/s$.

3.2 Detection

This section is adapted from [25], an accepted manuscript of an article published by Taylor & Francis in Journal of Modern Optics on 12 November 2019, available online: https://www.tandfonline.com/doi/full/10.1080/09500340.2019.1688410.

While all of the measurements of the atom beam involve detecting the fluorescence of atoms, what I will discuss here are the actual construction, optimization, and parameters of the detection apparatus itself which can be applied to measurement of interference as well as MOT characterization.

The basic detection scheme (as described in Section 2.3 and Figure 2.6) involves a PMT (Hamamatsu H6780-20) measuring the fluorescence of atoms excited by a detection laser (Eagleyard EYP-DFB-0780-00080-1500-TOC03 distributed feedback laser) tuned to the $F = 3$ to $F' = 4$ transition. There are some complications, however, due to the specifics of

the experiment. First, the divergence of the atom beam makes for a relatively large cross section at the 3rd window where the detection assembly is, so the laser and PMT must be configured accordingly. The transverse width of the detection laser beam is adjustable via an aperture—it can be made to match the atom beam width (3.56 cm as extrapolated from the previously described measurement and known vacuum chamber geometry) to achieve maximum signal strength or narrowed down to allow us to control the effective divergence of the atomic beam. Next, because the atom beam is not just large but *divergent*, there is a range of velocity classes present in every cross section. The consequence is that the carefully tuned $F = 3 \rightarrow F' = 4$ light is in resonance with some atoms but not in resonance with others (this is discussed in detail in Section 4.6). Finally, due to the longitudinal velocity of the atoms down the vacuum chamber, the downrange depth (thickness) of the detection laser must be large enough to scatter as many photons as possible without optically pumping the atoms back into the dark state. Figure (3.6) shows measurements of the fluorescence signal strength as a function of the downrange depth of the detection laser beam. Based on these measurements we shaped the beam to have a depth of $1.5\ mm$, just at the saturation point.
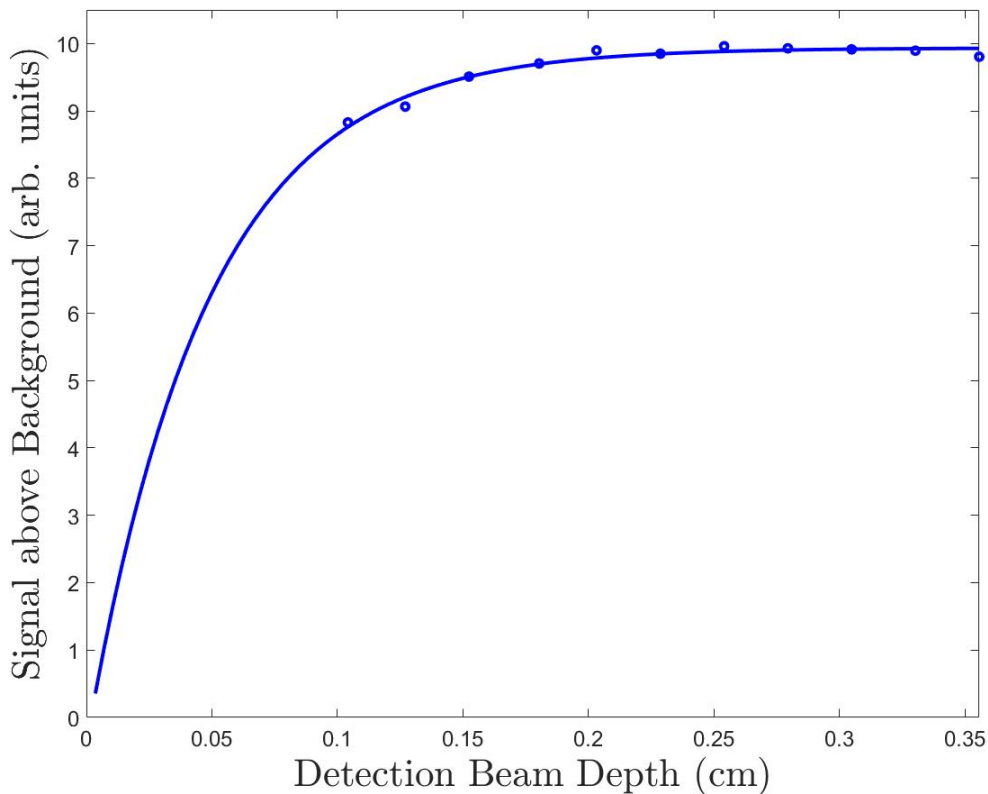
Figure 3.6: Atomic beam fluorescence signal as a function of detection beam depth (thickness down the long axis of the vacuum chamber). The data points are fit to $y = A\left(1 - \exp\left(-bx\right)\right) + c$, where $A = 20.6$, $b = 0.0479 \ \left[cm\right]^{-1}$, and $c = 12.8$.

The actual transverse width of the detection beam is $\sim 1 \ cm$. We achieve this sheet-shaped beam by shining the detection laser beam through an anamorphic prism pair and spherical lens before directing it through the vacuum chamber. The exact position of the beam through the window was fine-tuned by optimizing the atomic beam fluorescence signal above background. The power was adjusted and tuned in a similar manner as the cooling and repump laser powers. In this case, the signal above the background and the background level itself move as the beam is adjusted, but ultimately the same metric is used for optimization (the SNR as defined in Section 3.1.1).

32

3.2.1 Lock-In Detection

Parts of this section are adapted from [25], an accepted manuscript of an article published by Taylor & Francis in Journal of Modern Optics on 12 November 2019, available online: https://www.tandfonline.com/doi/full/10.1080/09500340.2019.1688410.

Due to the Zeeman degeneracy of the $F = 2$ ground state, the maximum Raman signal we could expect to detect is 20% of the optical fluorescence signal. This type of signal (Raman) will be explained in detail in Section 4.1; for now we take its importance to be axiomatic. In our system, we found that this results in a relatively small signal sitting on a large background (mostly from stray laser light). To remove the background effects and improve the signal-to-noise ratio of the spectra we fed the output of the PMT into a lock-in amplifier (LIA) (Stanford Research Systems SR530 lock-in amplifier). We frequency modulated ("dithered") the detection laser while it was locked to the cooling transition and phase detected on this signal.

Figure (3.7) shows how our lock-in detection works. We lock the detection laser about one linewidth away from resonance and apply a frequency dither of amplitude of approximately one linewidth. This results in a signal that looks like an amplitude dither. There are two reasons why we chose specifically to frequency modulate the detection laser. First, if we amplitude modulate the detection laser, we would eliminate scatter from the Raman laser but not from the detection laser. Note that the signal intensity is given by

$$I_{total} = I_{fluorescence} + I_{Raman\ scatter} + I_{Detector\ scatter}, \tag{3.1}$$

where $I_{fluorescence}$ is the desired signal and $I_{Raman\ scatter}$ and $I_{Detector\ scatter}$ are unwanted signals. Frequency modulating the detection laser eliminates scatter from both lasers. Second, we dither the detection laser rather than the Raman laser so we do not have to integrate the signal for too long of a time. Due to the narrower linewidth of the Raman signal we would need a slower dither followed by integration, so the current setup scheme allows us to use a smaller integration time constant.
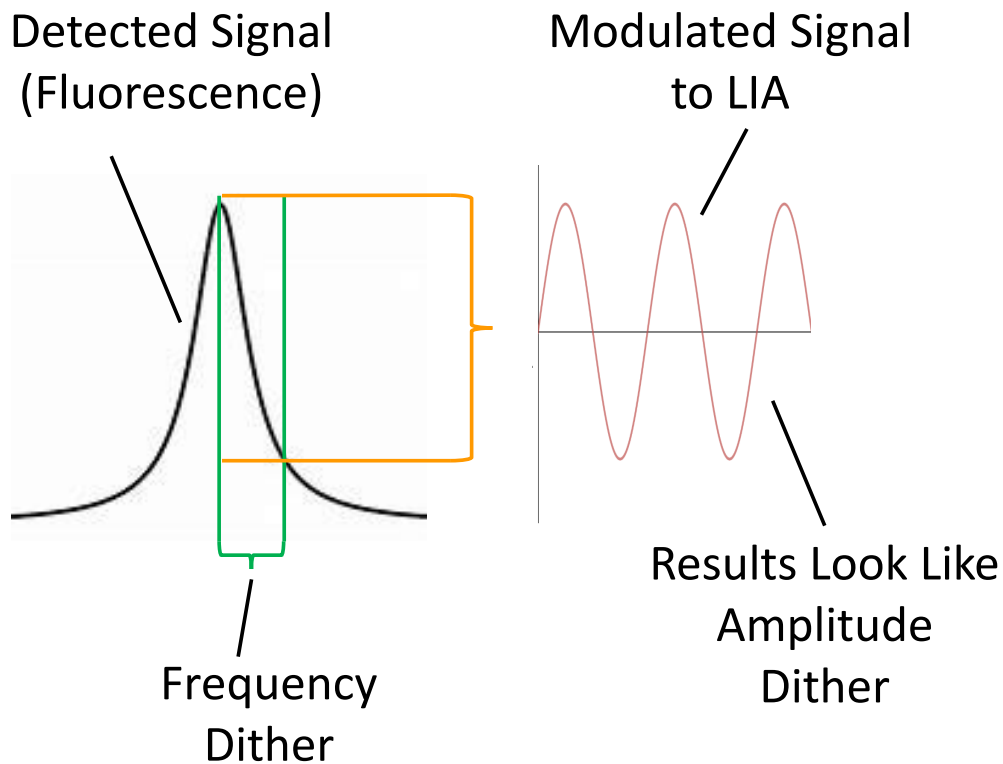
Figure 3.7: Depiction of the lock-in detection method which makes a small frequency dither look like an amplitude dither.

3.3 Optical Pumping

3.3.1 Optimal Optical Pumping Transition Determination

In the previous chapter, we discussed why we could not use the $F = 3$ to $F' = 4$ transition to optically pump atoms into the $F = 2$ state, namely the momentum transfer leading to atom beam deflection. The next step is to confirm this via experiment as well as to confirm the effectiveness of $F = 3 \rightarrow F' = 2$ as an optical pumping transition.

A typical experiment to count the number of atoms in the detection region might involve a scanning detection laser, which causes fluorescence from the atoms with a Lorentzian

profile. Introduction of the optical pump beam can lead to a drop of the signal, ideally to zero if the drop is due to true optical pumping. Unfortunately, a drop to zero signal can also be caused by a complete loss of atoms (from atom beam deflection, for example) rather than complete optical pumping. To unambiguously differentiate between good optical pumping and no atom beam, rather than scanning the detection laser to produce a single peak of atoms fluorescing as they decay to the $F = 3$ state, we locked the detection laser at the $F = 3 \rightarrow F' = 4$ frequency and scanned a single frequency-shifted beam from an additional auxiliary laser (the Raman laser, used here for a different purpose). Figure (3.8) is a measurement of the atomic beam fluorescence versus Raman laser frequency with no optical pumping (purple trace), optical pumping on the $F = 3 \rightarrow F' = 4$ transition (yellow trace), and optical pumping on the $F = 3 \rightarrow F' = 2$ transition (orange trace) ($F = 3 \rightarrow F' = 3$ is both less efficient than $F = 3 \rightarrow F' = 2$ and more difficult to produce with our equipment and is thus omitted here). The SATABS of the scanning Raman laser is included as a frequency reference.
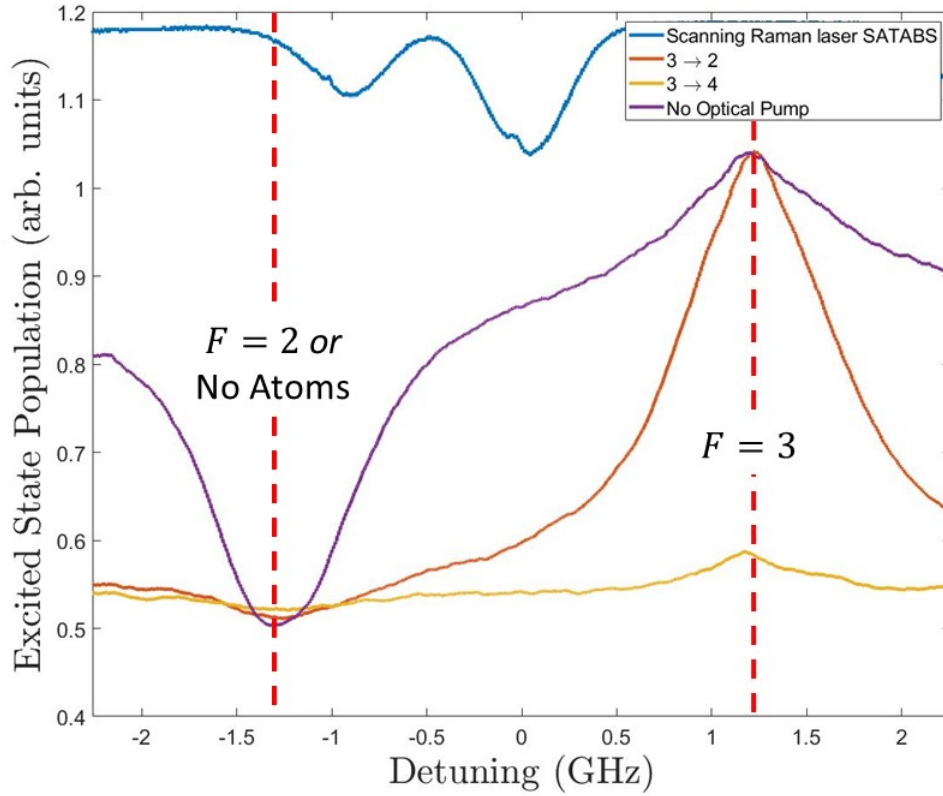
Figure 3.8: Fluorescence measurements used to determine optimal optical pumping transition.

First, consider the no pumping fluorescence ("No Optical Pump") as compared to the SATABS. Since there is no pumping, the atoms are in some combination of the $F = 2$ and $F = 3$ states as they enter the vacuum chamber (numerical modeling indicates they are mostly in the $F = 3$ state). Next, the atoms are illuminated by the scanning Raman laser and then the locked detection laser. Atoms that are illuminated by the Raman laser as it scans through $F = 3 \rightarrow F' = 4$ resonance are put into $F = 2$ and *are not* excited by the detection laser—this is the dip in the left side of the "No Optical Pump" trace. Atoms that are illuminated by the Raman laser as it scans through $F = 2 \rightarrow F' = 3$ resonance are put into $F = 3$ and *are* excited by the detection laser—this is the peak in the right side of the "No Optical Pump" trace. (Note that the positions of these resonances are shifted by $1.5\,GHz$ relative to $F = 3 \rightarrow F' = 4$ in the SATABS. This is simply due to the fact that, for

convenience, our auxiliary laser beam is simply one of the frequency-shifted beams from our Raman laser setup, described later in Section 4.1.)

Next, we consider the traces with optical pumping on, starting with the "$3 \to 4$" trace. We expect this light to displace the atom beam such it is that (virtually completely) deflected and therefore the detection laser sees (virtually) no atoms, and that is exactly what we see. Finally, with the $F = 3 \to F' = 2$ pump on, all of the atoms are in $F = 2$ as they enter the vacuum chamber. Atoms that are illuminated by the Raman laser as it scans through $F = 2 \to F' = 3$ resonance are put back into $F = 3$ and are excited by the detection laser as seen by the peak on the right side of the "$3 \to 2$" trace. Atoms illuminated by any other frequency of light do not make it into $F = 3$. With this method, effective optical pumping will result in a baseline at the intensity of the "No Optical Pump" dip and a peak height at the intensity of the "No Optical Pump" peak, which is precisely what we see here.

3.3.2 Optical Pumping Setup Scheme

To provide a steady source of $F = 3 \to F' = 2$ light for the optical pump, we start by picking off a beam of light from the cooling laser breadboard (the machined aluminum plate onto which the laser and all of its associated optics are attached, which is then attached to the optics table). This means the light is essentially at the $F = 3$ to $F = 4'$ transition (red-detuned by $6 \; MHz$). The desired purpose of the setup scheme is to be able to use that unaltered light to deflect the atoms and hence turn off the atomic beam while also being able to use altered light as an $F = 3 \to F' = 2$ optical pump. To do that the frequency of the light must be red-shifted by $178 \; MHz$ ($184 \; MHz$ total between the $F' = 2$ and $F' = 4$ levels minus the $6 \; MHz$ of detuning) [24]. We do this by using an acousto-optic modulator (AOM) (Isomet 1205C-2-804B driven by Isomet D322B-788-805 acousto optic deflector driver) and exploiting the fact that it can alternately produce a 0th order beam that is not frequency shifted and a 1st order beam that is. However, the AOM cannot produce a frequency shift of $178 \; MHz$ after a single pass; its specification is $80 \pm 20 \; MHz$. Our solution to this problem is a double-pass configuration.

Fiber from Cooling Laser

Lens

Mirror

AOM

0th Order   0th Order

Fiber to Atom Beam

1st Order

1st Order
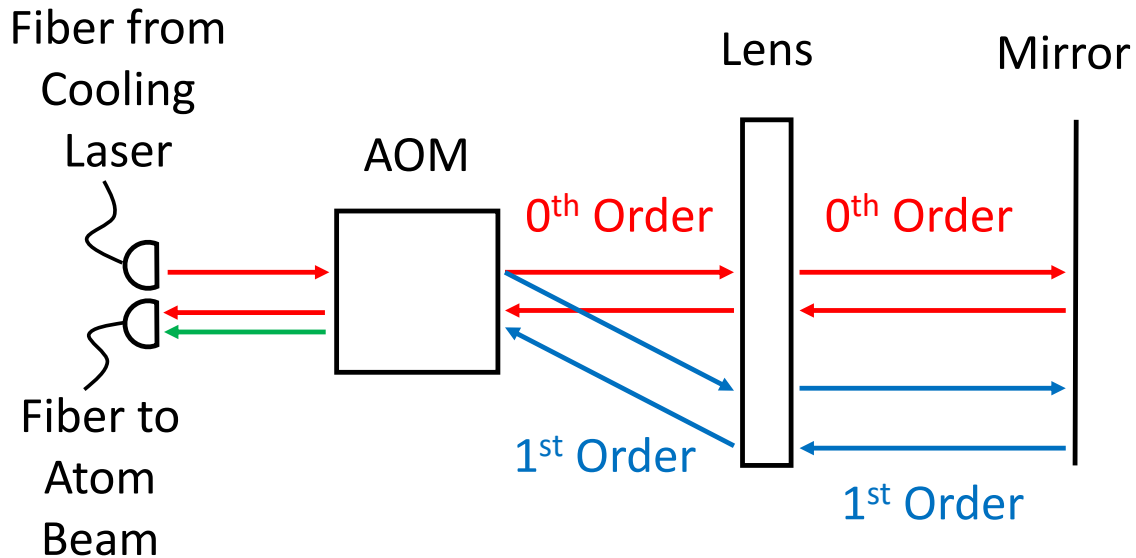
F = 3 to *F*′ = 4 Light
F = 3 to halfway between *F*′ = 4 and *F*′ = 2
F = 3 to *F*′ = 2 Light

Figure 3.9: Optical pumping scheme whereby cooling laser light is frequency shifted to optical pumping light via two passes through an AOM.

Figure (3.9) is a depiction of the optics setup on the optical pump breadboard. After coming out of a fiber from the cooling laser breadboard, the light passes through the AOM. The 0th order beam is neither frequency shifted nor deflected; the 1st order beam is shifted approximately $89\ MHz$ and deflected. We have a lens inserted after the first pass through the AOM whose focal length is such that the 0th and 1st order beams emerge parallel to each other. These then retroreflect off of a mirror and follow the same path back through the lens and converge in the AOM resulting in the *second-pass* 0th order beam consisting of light from the *reflected first-pass* 0th and 1st order beams (in this application we are not concerned with the 1st order beam from the second pass). So, the 0th order beam from the second pass contains $F = 3 \rightarrow F' = 2$ light (that went straight through the AOM twice

and never shifted) and also light that shifted twice for a total of $184\ MHz$. This results in $F = 3 \to F' = 4$ light coupling into the fiber to the atom beam when the AOM is off and a combination of $F = 3 \to F' = 4$ and $F = 3 \to F' = 2$ light coupling into the fiber when the AOM is on. The AOM was adjusted upon insertion so that, when on, the power from the $F = 3 \to F' = 4$ light is negligible compared to the $F = 3 \to F' = 2$ light.

We measured effectiveness of different beam sizes and different points of intersection with the atom beam. We found that a relatively large beam intersecting the atom beam prior to the aperture gives the most effective pumping. The power was adjusted and tuned in the same manner as the cooling and repump laser powers.

3.3.3   Optical Pump as an Atom Beam Switch

The optical pump scheme with its AOM is thus, in essence, a switch for the atom beam. When the signal to the AOM driver is off, the atom beam is off (deflected); when the signal is on, then a beam of atoms optically pumped into the proper state ($F = 2$) propagates down the vacuum chamber. This feature lends itself well to another velocity profile measurement of the atom beam (to compare with the previous measurement made in Section 3.1.1).

Experimentally, this starts with a detection laser locked at the peak of fluorescence from an atomic beam that is not being optically pumped. We then use a function generator (Agilent 33220A 20MHz Function / Arbitrary Waveform Generator) to configure the optical pump such that it is at a baseline of $F = 3 \to F' = 4$ and essentially turning the atom beam off. Next, we introduce a brief step function that produces a pulse of off-resonance light, whose effect is to produce a pulse of atoms that make it through the aperture but that are *not* optically pumped. Figure (3.10) depicts the result—a baseline of no signal with a peak of atoms propagating down the vacuum chamber. The width of the peak is a consequence of the velocity spread of the atoms and the center of the peak gives the most probable velocity of the atoms. The measured velocity is $v_{mp} = 6.4\ m/s$ (strictly speaking we measured the time then applied this to the distance traveled between the optical pump beam and the detection beam farther down the vacuum chamber). This corroborates the rough measurement of $1.4\ m/s$ and the working value of $10\ m/s$ from Section 3.1.3.
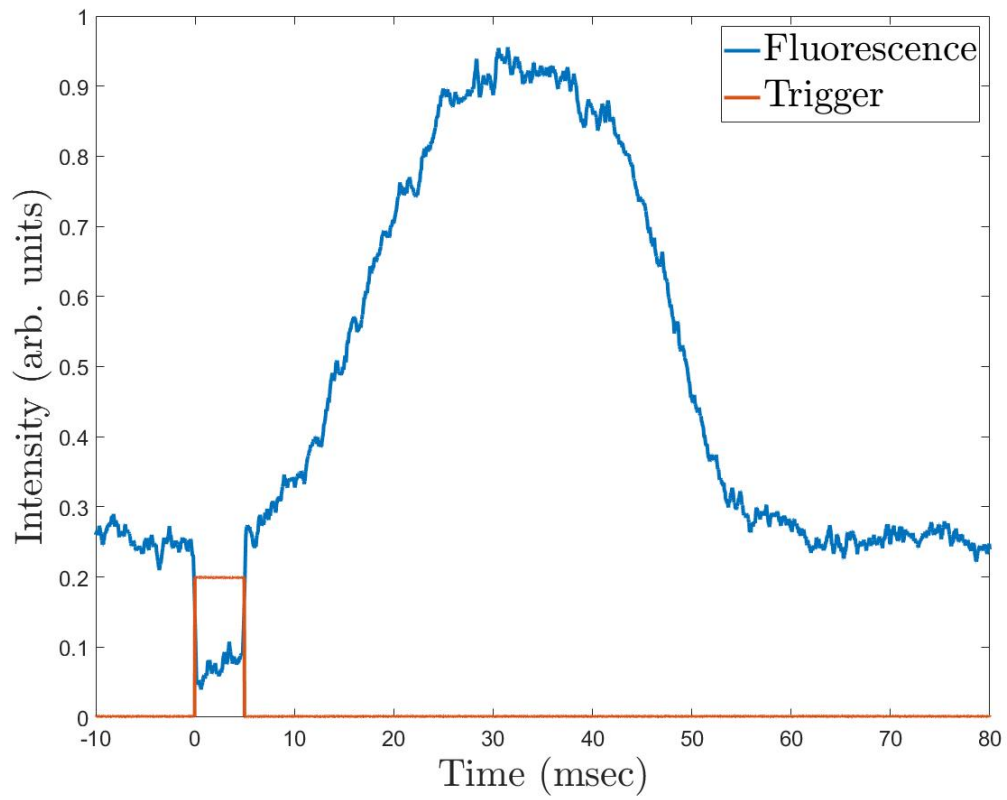
Figure 3.10: Travel time of optically pumped atoms. The amplitude peak corresponds to the most probable speed of 6.4 m/s.

CHAPTER 4:
Atom Interferometry: Theory

4.1 The Raman Process

A Raman process is one in which an atom starts in one ground state and ends up in another. For the purposes of this dissertation, what we refer to as a Raman process is really a *stimulated* Raman process with laser fields stimulating the transition between the states. Recall the "usual" depiction of a simple atomic transition—the two-level atom discussed in Section 2.1 (specifically Figure 2.1). When the two-level atom involves a ground state and an excited electronic state, spontaneous emission—which is incoherent—cannot be avoided and is a serious drawback. In order to avoid this, one can drive a Raman transition between two ground states, thus eliminating spontaneous emission. This avoidance of spontaneous emission is the critical element of the Raman process that makes it a fundamental building block of this experiment.

To visualize what is happening, we replace the picture of the simple, two-level atom with a diagram of a three-level atom in a *lambda configuration*, so named for the overall visual shape of the diagram [25]. As shown in Figure 4.1, this atom now has two ground states ($|1\rangle$ and $|2\rangle$) and one excited state ($|3\rangle$). (In our experiment, $|1\rangle$ and $|2\rangle$ correspond to $F = 2$ and $F = 3$, respectively, and $|3\rangle$ corresponds to the F' states; we will do away with the F and F' notation for the duration of this chapter for clarity.) Now there are *two* laser fields driving *two* atomic transitions; one laser tuned to frequency ω_1 driving $|1\rangle \rightarrow |3\rangle$ and another laser at ω_2 driving $|2\rangle \rightarrow |3\rangle$. With two lasers, we modify the Rabi frequency equation from Section 2.1,

$$\Omega = \frac{2\left(\boldsymbol{\mu}^* \cdot \boldsymbol{\epsilon}_l\right)\mathcal{E}}{\hbar}, \tag{2.2}$$

to read

$$\Omega_1 = \frac{2\left(\boldsymbol{\mu}_{13}^* \cdot \boldsymbol{\epsilon_1}\right)\mathcal{E}_1}{\hbar}, \tag{4.1}$$

for the laser driving $|1\rangle \rightarrow |3\rangle$ and

$$\Omega_2 = \frac{2\left(\boldsymbol{\mu}_{23}^* \cdot \boldsymbol{\epsilon_2}\right)\mathcal{E}_2}{\hbar}, \tag{4.2}$$
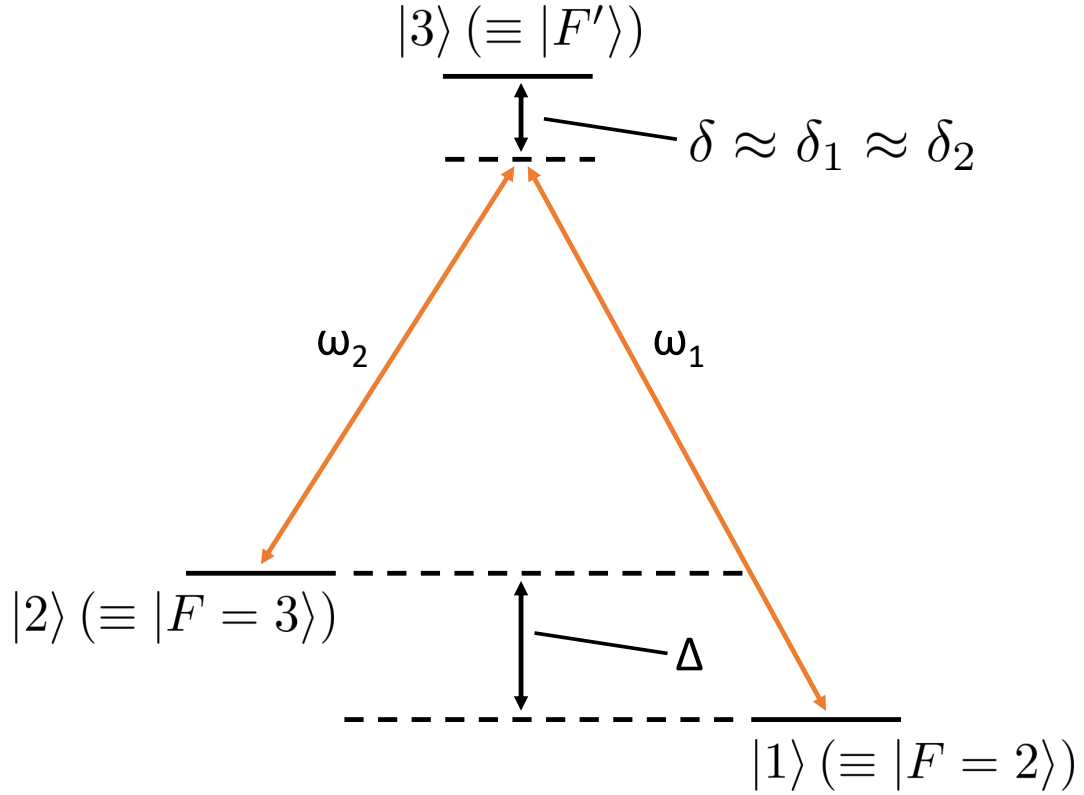
Figure 4.1: Depiction of a three-level atom in a lambda configuration.

for the laser driving $|2\rangle \rightarrow |3\rangle$.

As depicted in Figure (4.1), each laser is detuned such that $\delta_1 \equiv \omega_1 - \omega_{13}$ and $\delta_2 \equiv \omega_2 - \omega_{23}$ (when $\delta_i = 0$, $\omega_i = \omega_{i3}$). The final step in moving from the two-level to the three-level system involves resonance. A single laser driving a single resonance is said to be driving a *single-photon* resonance because it takes a single photon to go from one state to the other. Any detuning from single-photon resonance is captured in the parameter δ. We can consider the Raman transition from $|1\rangle$ to $|2\rangle$ (or the reverse) as a two-step process with $|3\rangle$ as an intermediate state. Because it takes one photon to go up (to $|3\rangle$) and another one to come down, the resonance between the two ground states ($|1\rangle$ and $|2\rangle$) is now a *two-photon* resonance. The parameter Δ, also known as *ground state hyperfine splitting*, is the frequency difference between the two ground states. Here, we assume that Δ is

large enough and the dipole matrix elements and laser polarization vectors are chosen such that each laser couples only to its respective transition. When driving a stimulated Raman transition, the individual detunings of the lasers are chosen such that $\delta_1 - \delta_2 - \Delta \approx 0$, which puts the system very close to two-photon resonance. Under these specific conditions (laser field parameters and detunings) the system acts like the simple, two-level atom of Section 2.1. We simply replace the two-level atom (aka single-photon) detuning δ with the two-photon detuning $\delta_2 - \delta_1$ and the two-level (single-photon) Rabi frequency Ω with the two-photon Raman Rabi frequency $\Omega_R = \Omega_1 \Omega_2 / (2\delta)$. The excited state $|3\rangle$ is a virtual state in which the atoms spend no actual time as they cycle between the two ground states. Thus the two ground states $|1\rangle$ and $|2\rangle$ are now effectively a ground state and an excited state (with no spontaneous decay!), which we will refer to simply as $|g\rangle$ and $|e\rangle$. This is the (stimulated) Raman process used in this experiment.

4.2 Mach-Zender Interferometry

Figure (4.2(left)) depicts the basic layout of an optical Mach-Zender interferometer. A single light wave is split into two separate waves by a beam splitter. Then the two separate waves are reflected by mirrors such that they meet and are recombined in a second beam splitter. The two output beams of this beam splitter will have intensities which vary interferometrically. If the interferometer were subject to, say, a rotation, then the path length difference between the two beams will change, which will lead to a relative phase shift between the two beams and an observable intensity change at the output of the second beam splitter. Note that the enclosed area between the paths is critical to the functionality of the interferometer (more on that in Section 4.7).

Figure (4.2(right)) depicts the same interferometer design with the initial light wave replaced by a matter wave. In this depiction, the matter wave is provided from an atom sufficiently cooled to allow observation of wave-like properties; the atom enters the interferometer in the ground state $|g\rangle$ due to the previously described optical pumping. Whereas the light wave was split in two by a physical optic (a beam splitter), here we have the matter wave encountering a light pulse known as a $\pi/2$-*pulse*. This pulse creates a superposition of ground and excited states, $|g\rangle$ and $|e\rangle$, respectively (more on how in the next section). Thus the $\pi/2$-pulse acts as an analog of a beam splitter. Next, both waves encounter a π-*pulse* which has the effect of switching the state of each wave; the π-pulse acts as an

analog of a mirror (collectively these pulses are also referred to as *Raman pulses* as in Section 3.1). Finally, both states are recombined at a second $\pi/2$-pulse; we can choose to measure either state at the output of the interferometer. The number of atoms will depend interferometrically on the path length difference. Note that this version of the Mach-Zender interferometer also has an enclosed area between the two paths.
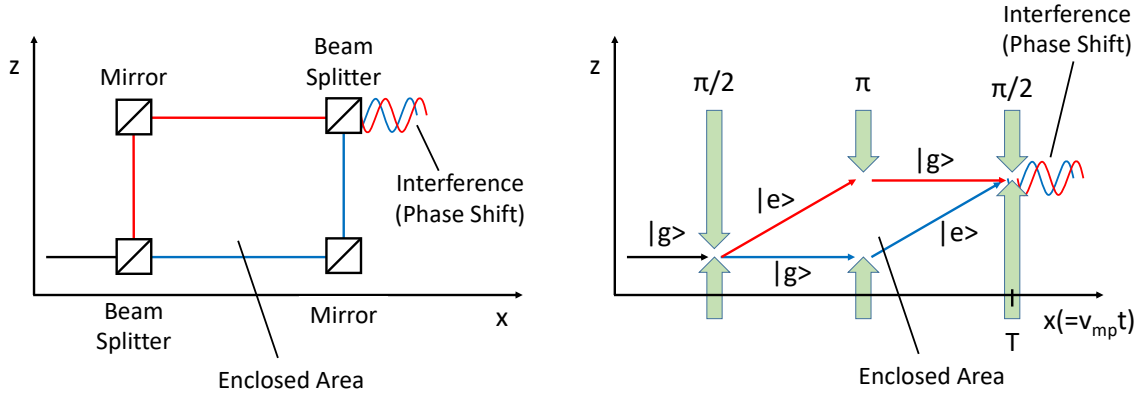
Figure 4.2: Mach-Zender interferometer using light waves (left). Mach-Zender interferometer using matter waves with light pulses as analogs for beam splitters and mirrors (right). Note that this simultaneously represents state-space and top-down views.

4.3   Light Pulses as Optics

So how exactly do light pulses act as mirrors and beam splitters? For now, let us consider Figure (4.2) from the perspective of state (rather than physical) space and focus on the two atomic states $|g\rangle$ and $|e\rangle$. A mirror pulse causes the transformation

$$|g\rangle \to i|e\rangle, \tag{4.3a}$$

$$|e\rangle \to i|g\rangle; \tag{4.3b}$$

these are the results of a π-pulse. Similarly, a beam-splitter pulse causes the transformation

$$|g\rangle \to \frac{1}{\sqrt{2}}\left(|g\rangle + i|e\rangle\right), \tag{4.4a}$$

$$|e\rangle \to \frac{i}{\sqrt{2}}\left(|g\rangle - i|e\rangle\right); \tag{4.4b}$$

these are the results of a $\pi/2$-pulse. In this section, we will see where these formulae come from. For this discussion, we will use the language of Section 2.1 and the two-level atom; Ω is replaced by $\Omega_R = \Omega_1 \Omega_2 / (2\delta)$ and δ is replaced by $\delta_2 - \delta_1$. This standard quantum optics technique adiabatically eliminates the excited state and leaves the two ground states which act as a ground state $|g\rangle$ and effective excited state $|e\rangle$.

We now add some details to our description of our driven two-level system. This system is described in general by the wave function

$$|\Psi\rangle = \tilde{c}_g(t)|g\rangle + \tilde{c}_e(t)|e\rangle \tag{4.5}$$

where $\tilde{c}_{g/e}$ denotes the probability amplitude of the ground/excited state. The tilde indicates that we have applied the *rotating wave approximation* and removed oscillations at the laser frequency; the details are not relevant to this discussion and we can consider this convention at this point. The solution to the Schrödinger equation for this system is given by Equation (4) of [27], written here in matrix form

$$\begin{bmatrix} \tilde{c}_g(t) \\ \tilde{c}_e(t) \end{bmatrix} = \begin{bmatrix} \tilde{c}_g^g(t) & \tilde{c}_g^e(t) \\ \tilde{c}_e^g(t) & \tilde{c}_e^e(t) \end{bmatrix} \begin{bmatrix} \tilde{c}_g(0) \\ \tilde{c}_e(0) \end{bmatrix} \tag{4.6}$$

where

$$\tilde{c}_g^g(t) = \left(\cos\left(\Omega't/2\right) - i\frac{\delta}{\Omega'}\sin\left(\Omega't/2\right) \right) e^{i\delta t/2}, \tag{4.7a}$$

$$\tilde{c}_e^g(t) = i\frac{\Omega}{\Omega'}\sin\left(\Omega't/2\right)e^{i\delta/2}, \tag{4.7b}$$

and

$$\tilde{c}_g^e(t) = i\frac{\Omega^*}{\Omega'}\sin\left(\Omega't/2\right)e^{i\delta/2}, \tag{4.8a}$$

$$\tilde{c}_e^e(t) = \left(\cos\left(\Omega't/2\right) + i\frac{\delta}{\Omega'}\sin\left(\Omega't/2\right) \right) e^{i\delta t/2}. \tag{4.8b}$$

Here, we have introduced yet another Rabi frequency $\Omega' \equiv \sqrt{\Omega^2 + \delta^2}$; this is known as the *generalized Rabi frequency*. We have also taken the $\tilde{c}_{g/e}$ notation from Equation (4.5) and added a superscript to indicate in which state the atom started. So, for example, $\tilde{c}_e^g(t)$

indicates the probability amplitude at time t of $|e\rangle$ assuming the initial state was $|g\rangle$. Because we prepare our atoms initially in the ground state and make our measurements on the excited state (as described in Section 2.3), the probability amplitude $\tilde{c}_e^g(t)$ is the quantity we are most interested in.

Figure (4.3) depicts this sinusoidal oscillation of the excited state population (mathematically this is given by the square of Equation 4.7b). On the left, the population has reached an even superposition at time $T_{\pi/2}$. On the right, the population has fully changed from $|g\rangle$ to $|e\rangle$ at time T_π (which is also the time it takes to go from $|e\rangle$ to $|g\rangle$). So, when you drive a system, subject to the parameters contained within the Rabi frequency for just enough time such that it evolves into an even superposition of states ($T_{\pi/2}$), a $\pi/2$-pulse has occurred. Similarly, when the same system continues to evolve until the time when the population has fully gone to $|e\rangle$ (T_π), a π-pulse has occurred. We can also now understand the nomenclature—when the argument of the cosine function is $\pi/2$ (or π) we have a $\pi/2$ (or π)-pulse. These *perfect* pulses require precise control of the laser amplitude and detuning (and thus the Rabi frequency) and the time the atom sees the light.
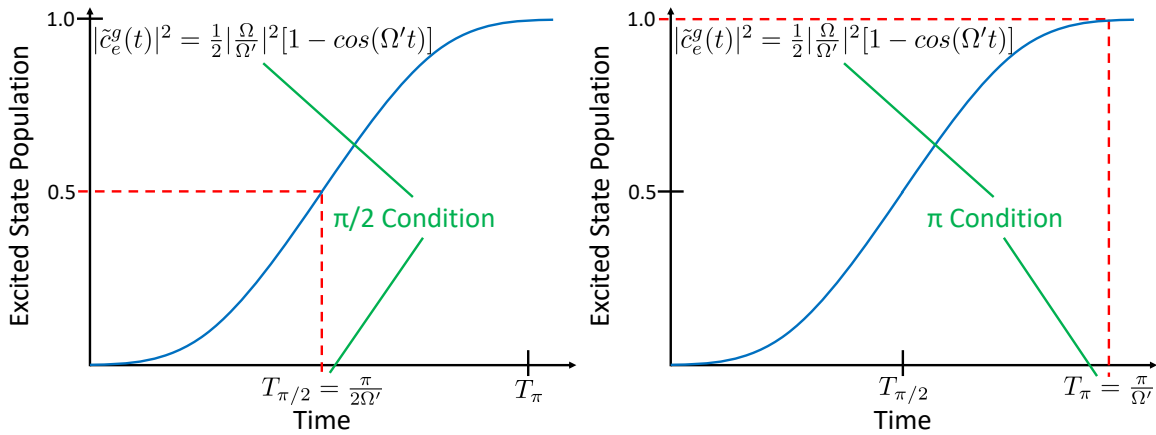
Figure 4.3: A driven two-level system undergoing a $\pi/2$-pulse such that it becomes an even superposition of states (left). A driven two-level system undergoing a π-pulse such that the population has completely moved from $|g\rangle$ to $|e\rangle$ (right).

There is one final parameter that must be controlled effectively for light to act as an optic. Note that the π and $\pi/2$ conditions depend on the Rabi frequency and recall from Equation (2.2) that the Rabi frequency also depends on polarization. In general, the "path"

the atom takes as it goes between both ground states (via the virtual excited state) in any stimulated Raman transition is dependent on the polarization. So, even though we are working with an effective two-level system, the third level affects how the atom transitions between the two levels.

There are two polarization conditions that work in this experiment: crossed-linear polarization and same-handed circular polarization (these conditions have been derived in detail in previous work [28]). The two entities that are implicitly being compared in these descriptions are the two frequency-shifted Raman beams that are contained in the Raman physical beam. These beams correspond to the lasers with frequencies ω_1 and ω_2 in the three-level atom diagram in Figure (4.1); how these beams are made in the experiment will be described in Section 5.1.1.

4.4 Co- vs. Counter-Propagating Beams

As long as one of the required polarization conditions is met, the picture developed in Section 4.3 is valid from a state-space perspective. The enclosure of an actual area in Cartesian space by the interferometer referred to in Figure (4.2), however, only occurs when momentum is considered. To do so we will discuss two different beam arrangements, namely co- and counter-propagating.

The simpler of the two (certainly from an experimental standpoint) is the co-propagating configuration. In this nomenclature, the beams that are co-propagating are the two frequency-shifted Raman beams that are coincident in a single physical beam; this configuration is also referred to as the *Doppler-free (DF)* configuration. As depicted in Figure (4.4), the physical beam is initially horizontally polarized (more on that in Section 5.1.1). After passing through a quarter-wave plate (QWP), the light is circularly polarized and, more importantly, the two frequency-shifted beams within the physical beam have same-handed circular polarization. Since their wave vectors are parallel, the effective wave number of the light is

$$
\begin{aligned}
k_{eff} &= |\boldsymbol{k_1} - \boldsymbol{k_2}|, \\
&\approx k_1 - k_1, \\
k_{eff} &\approx 0.
\end{aligned}
\tag{4.9}
$$

Intuitively, when looking at Figure (4.4), it would seem that there would indeed be a momentum kick in this scenario which appears to depict a beam of light pushing on a beam of atoms with nothing on the far side to counteract the force. However, recall from Section 2.1 that momentum transfer from laser light to an atom is $p = \hbar k$ where k is actually k_{eff}. Another way to understand this is to think about how an atom goes from one ground state to the other via the virtual excited state. As depicted in Figure (4.5), the laser field with $\boldsymbol{k_1}$ brings the atom up to the virtual state; the atom absorbs a momentum kick of $\hbar k_1$ in the direction of $\boldsymbol{k_1}$. The laser field with $\boldsymbol{k_2}$ brings it down to the second ground state via stimulated emission; the atom recoils *opposite* the direction of $\boldsymbol{k_2}$ with a magnitude of $\hbar k_2$. These effects cancel when $\boldsymbol{k_1}$ and $\boldsymbol{k_2}$ are co-propagating and when $k_1 \approx k_2$, both of which are the case here. Thus there is no momentum kick and no enclosed area in the Doppler-free configuration.
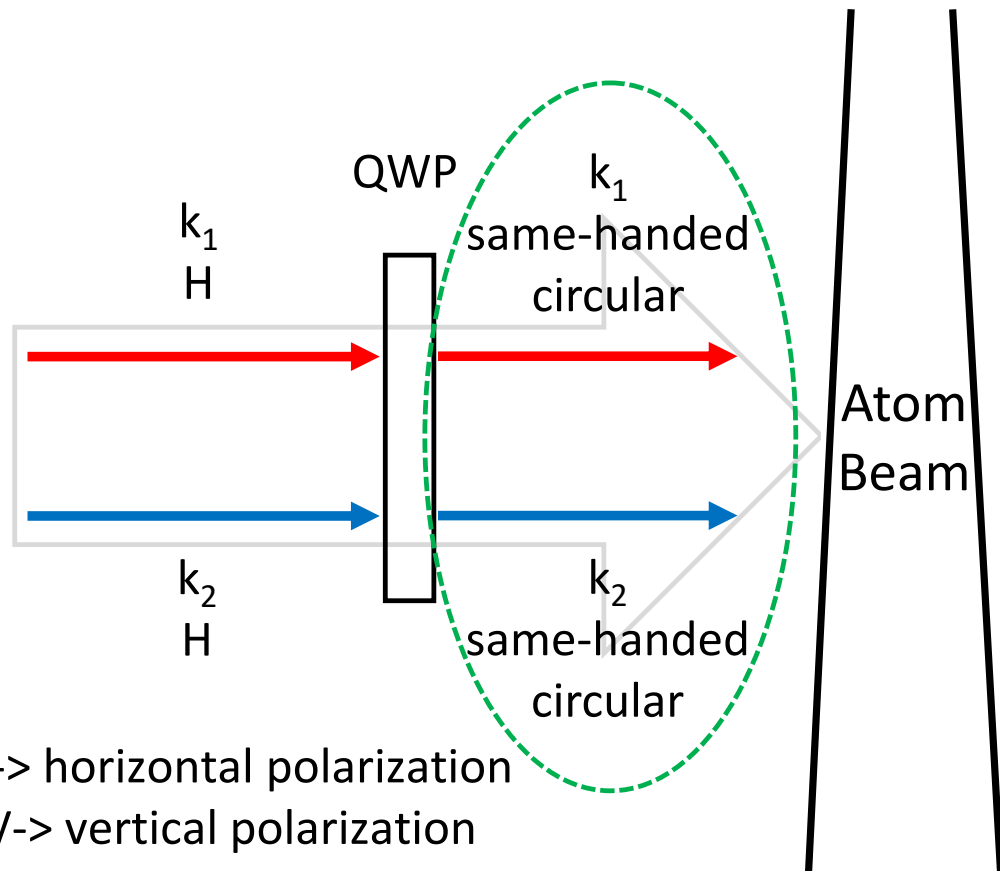
Figure 4.4: Top-down depiction of a single Raman physical beam in the Doppler-free configuration. Note that the two frequency-shifted beams produce one of the necessary polarization conditions (same-handed circular in this case, highlighted by the dashed ellipse) but do *not* produce a momentum kick since the wave vectors are parallel.

49
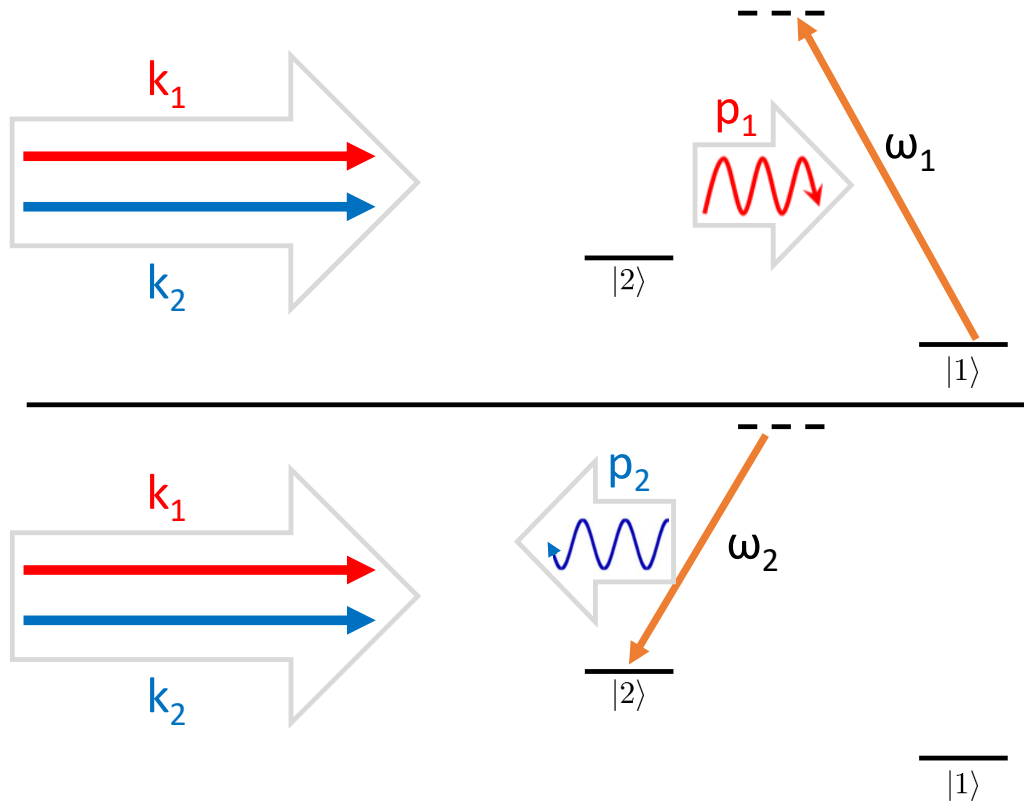
Figure 4.5: Schematic diagram of the momentum kick associated with the Doppler-free configuration with both frequency-shifted beams incident from the same direction (co-propagating). The red-shifted field gives a momentum kick to the atom as it brings it up to the virtual state (top); the blue-shifted field gives a momentum kick in the opposite direction as it brings it down to the second ground state (bottom). These effects cancel each other out and there is no net momentum kick.

Now, we consider the counter-propagating case, also referred to as the *Doppler-sensitive (DS)* configuration. As depicted in Figure (4.6), the physical beam (containing the two Raman frequency-shifted beams) that is incident on the atom beam does not meet a necessary polarization condition (note the absence of the QWP from the Doppler-free scenario). After passing through the atom beam, the light passes through a different QWP to become circularly polarized. The light then reflects off a retroreflecting mirror and passes back through the same QWP, which has the effect of producing vertically-polarized light. The

net result is a set of beams which meet the other option for necessary polarization, crossed-linear, but between pairs of laser fields that are counter-propagating. Intuitively, this now looks like a situation with balanced forces and no momentum kick; but, focusing on the effective wave number of light beams that meet the necessary polarization condition we see that p is *not* zero due to a nonzero wave number:

$$
\begin{aligned}
k_{eff} &= |\boldsymbol{k_1} - \boldsymbol{k_2}|, \\
&\approx k_1 - (-k_1), \\
k_{eff} &\approx 2k_1. \tag{4.10}
\end{aligned}
$$

Similarly to the co-propagating case, we can also think of this in terms of the atoms journey from one ground state to the other. As depicted in Figure (4.7), the laser field with $\boldsymbol{k_1}$ again brings the atom up to the virtual state; the atom absorbs a momentum kick of $\hbar k_1$ in the direction of $\boldsymbol{k_1}$ as in the co-propagating case. The laser field with $\boldsymbol{k_2}$ again brings it down to the second ground state; the atom recoils *opposite* the direction of $\boldsymbol{k_2}$ with a magnitude of $\hbar k_2$ as before, but now the direction of $\boldsymbol{k_2}$ is reversed. Thus, rather than cancelling each other out, the momentum kicks are additive.
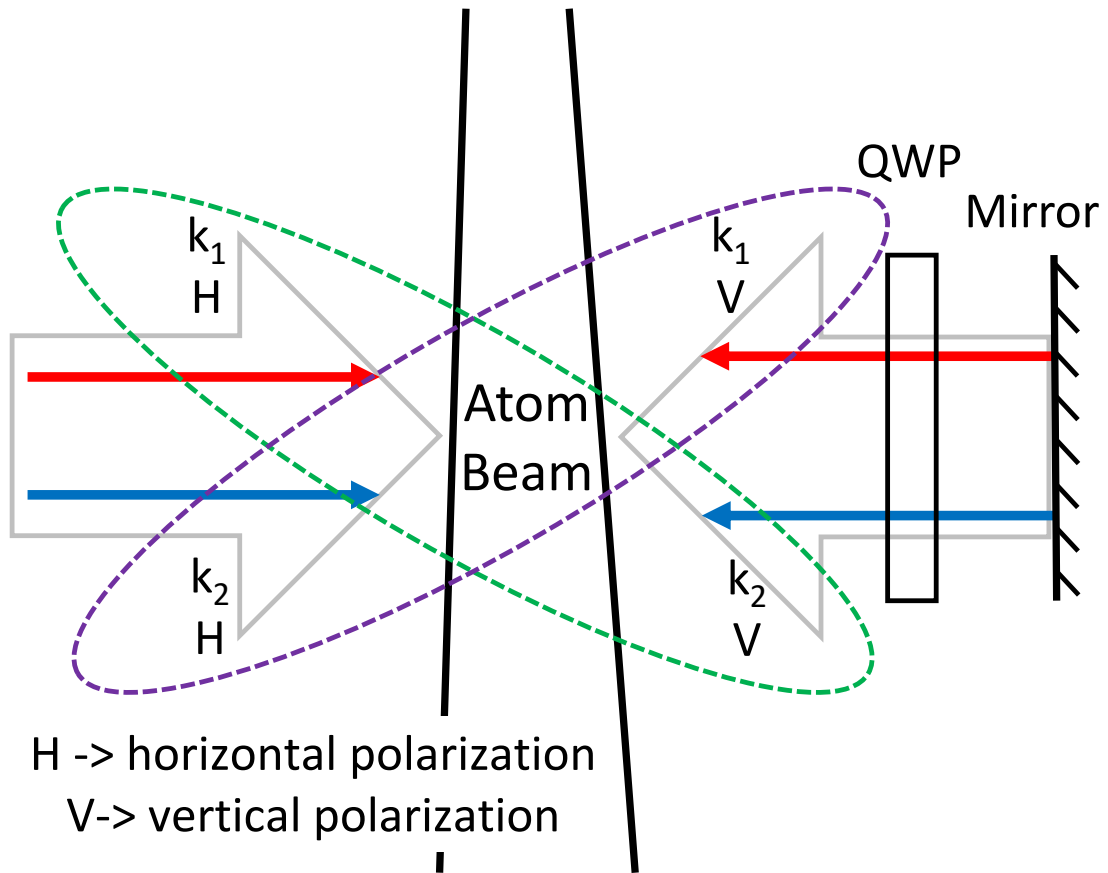
Figure 4.6: Top-down depiction of a single Raman physical beam in the Doppler-sensitive configuration. Note that the (two pairs of) two frequency-shifted beams (highlighted by the dashed ellipses) produce one of the necessary polarization conditions (crossed-linear in this case) only after retroreflection. They also produce a momentum kick since the wave vectors are anti-parallel.
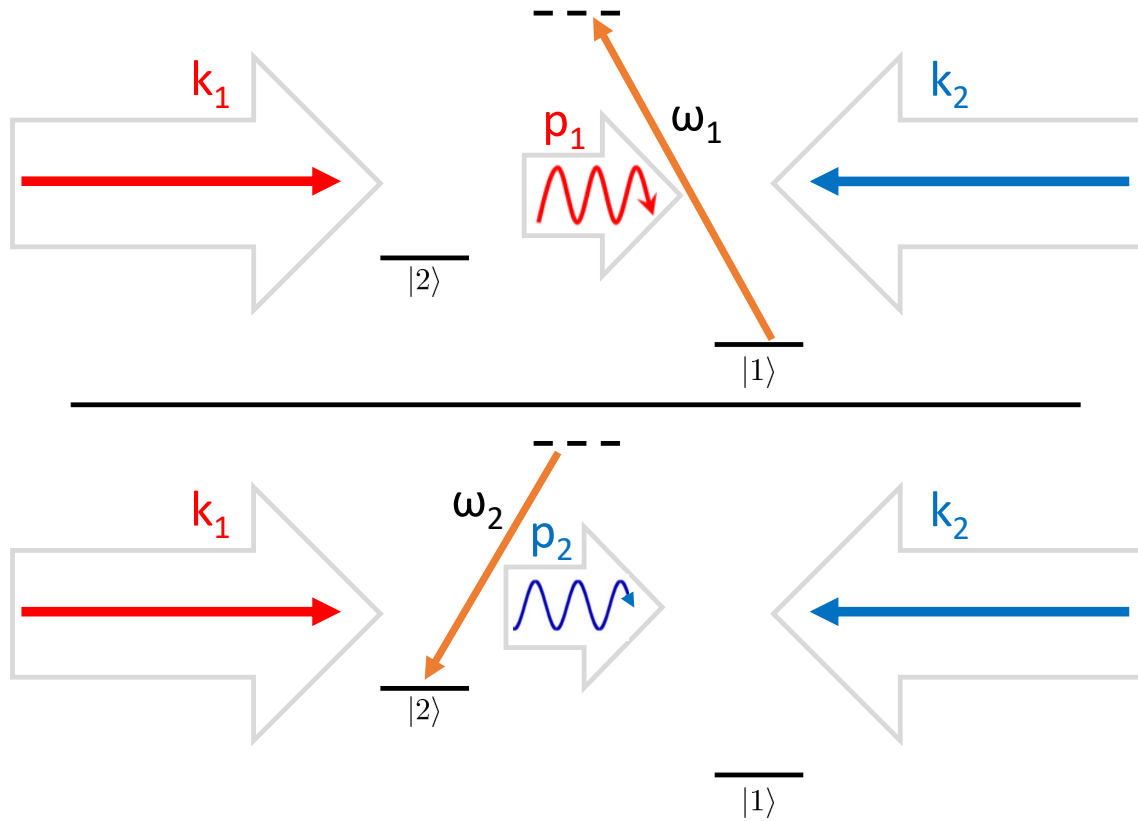
Figure 4.7: Schematic diagram of the momentum kick associated with the Doppler-sensitive configuration with the two frequency-shifted beams incident from opposite directions (counter-propagating). The red-shifted field gives a momentum kick to the atom as it brings it up to the virtual state (top); the blue-shifted field gives a momentum kick in the same direction as it brings it down to the second ground state (bottom). These effects combine to impart a net momentum kick.

Unfortunately, there is a third configuration of beams that meets a necessary polarization configuration: retroreflected Doppler-free. As depicted in Figure (4.8), this scheme is very similar to the layout of the aforementioned Doppler-sensitive setup—horizontally polarized light passes through the atom beam followed by a QWP and a mirror. In this case, however, the QWP is adjusted such that it changes the linearly polarized light into elliptically polarized light rather than circularly polarized light. This results in light that is still elliptically polarized after retroreflection and arbitrarily linearly polarized after a second pass through

the QWP. Note that, based on this description, it would still be possible for the vertically polarized components in the retroreflected light to couple with the horizontally polarized light. The precision of alignment of the incident and reflected physical beams, however, is critical according to intuition and discussion with experts in the field; numerical modeling is ongoing for our unique system. Due to the precision required, this scenario is more likely to produce transitions from the same-handed circularly polarized light in the reflected beam. Although undesirable, it is an unavoidable consequence of this configuration, the significance of which will be discussed in the next chapter.
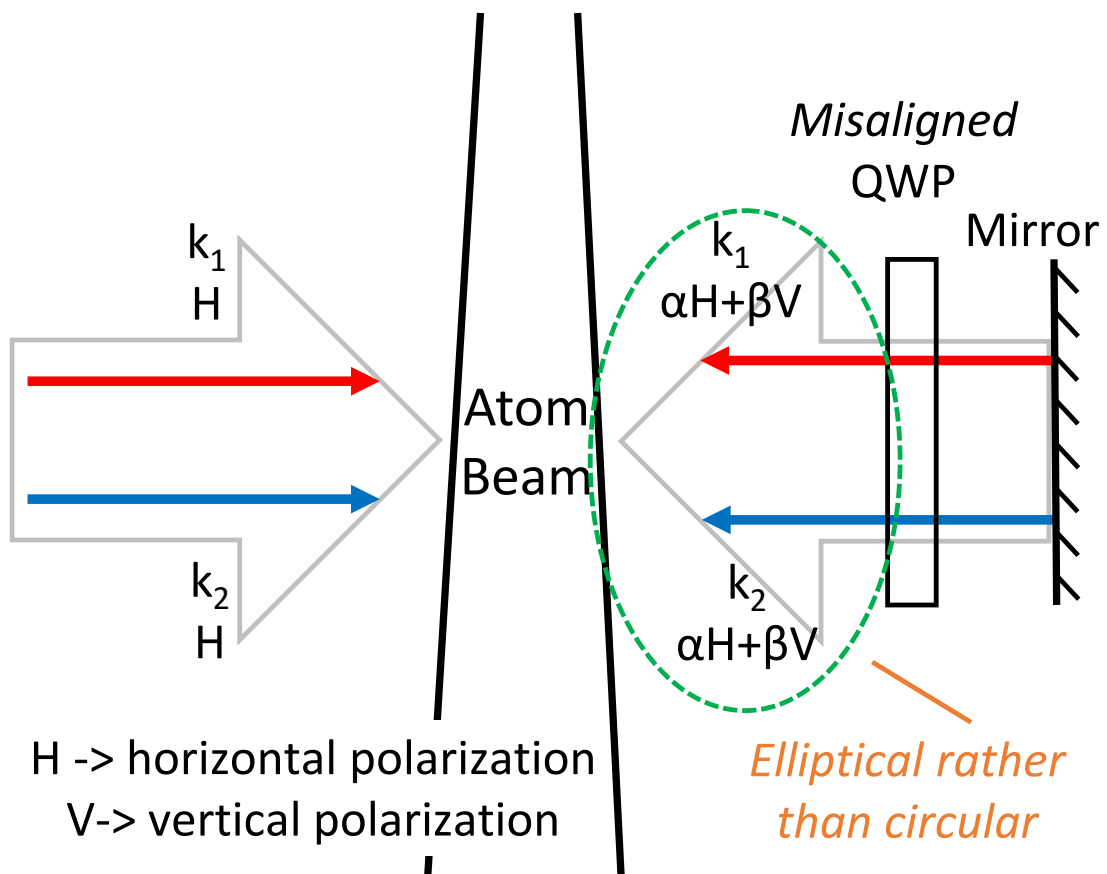
Figure 4.8: Top-down depiction of a single Raman physical beam in the retroreflecting Doppler-free configuration. Note that the (two pairs of) two frequency-shifted beams (highlighted by the dashed ellipses) produce one of the necessary polarization conditions (crossed-linear in this case) only after retroreflection. They also produce a momentum kick since the wave vectors are anti-parallel.

4.5 Combinations of Light Pulses: Raman, Ramsey, and Spin Echo Spectra

So far we have discussed the Raman process (Section 4.1) and light pulses acting as optics to make an interferometer (Sections 4.2, 4.3, and 4.4). The $\pi/2 - \pi - \pi/2$ combination of pulses used in the Mach-Zender configuration is known as a *spin echo* sequence. This sequence, in a Doppler-sensitive configuration, is what makes an inertially-sensitive atomic gyro. Experimentally, however, it makes sense to add some intermediate steps in the process to more effectively characterize the apparatus and troubleshoot as necessary. These steps consist of incrementally adding physical beams and doing so sequentially in the DF and DS configurations. These will be discussed in detail in Chapter 5.

In order to make the discussion of beam divergence theory (Section 4.6) make sense, I will briefly introduce an intermediate step known as *Ramsey interference*. This is similar to a spin echo sequence, but with the removal of the π-pulse, leaving a $\pi/2 - \pi/2$ sequence. This interference, which was developed by Norman Ramsey and earned him a Nobel prize, has been discussed in detail in other publications [26], [29]. The result is a series of fringes contained inside an envelope; the fringes are largely determined by the spacing of the two physical beams and the envelope is the Raman spectrum. The effect is analogous to and reminiscent of a double-slit interference pattern. Its usefulness in this context is to help us characterize different spacing configurations of our physical beams as well as being used to determine the effectiveness of our $\pi/2$-pulses, especially regarding the effects of velocity averaging and beam divergence.

4.6 Beam Divergence

This section is adapted from [25], an accepted manuscript of an article published by Taylor & Francis in Journal of Modern Optics on 12 November 2019, available online: https://www.tandfonline.com/doi/full/10.1080/09500340.2019.1688410.

Although we have just discussed pulses in detail, recall that all beams (atom and laser) in this experiment are continuous; the apparatus consists of atoms continuously extracted in a beam from a 2D-MOT which cross through the laser beams that generate the atom optic "pulses." The laser fields are on continuously and so the transit time of the atoms through the laser beam is treated as the laser "pulse." The atoms emanating from the 2D-MOT

have a spread in their velocity and hence a spread in the laser pulse time due to the spread in the time the atoms spend in the laser field. This has an effect of washing out fringes and was accounted for in our earlier publication [1]; specifically, with no velocity spread (and a perfectly collimated and monoenergetic beam) we would expect to see "perfect" Raman and Ramsey interference, for example—see Figures (4.9(left)) and (4.10(left)). Figures (4.9(right)) and (4.10(right)) show the expected effect of averaging over a velocity spread in the examples of Raman and Ramsey interference, respectively, with the expected reduction of fringes. In our experiment, both the laser beams *and* the atomic beam have divergence (see e.g., Section 3.1.2) which will affect the length of time the atoms spend in the laser beams and the free evolution time. These effects need to be taken into account.
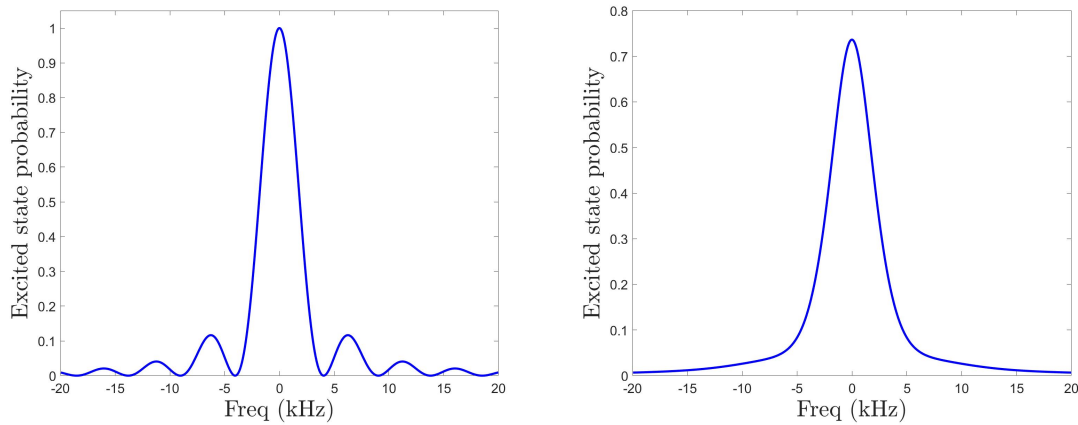
Figure 4.9: Raman spectrum with (left) and without (right) velocity averaging; note the loss of fringe structure.
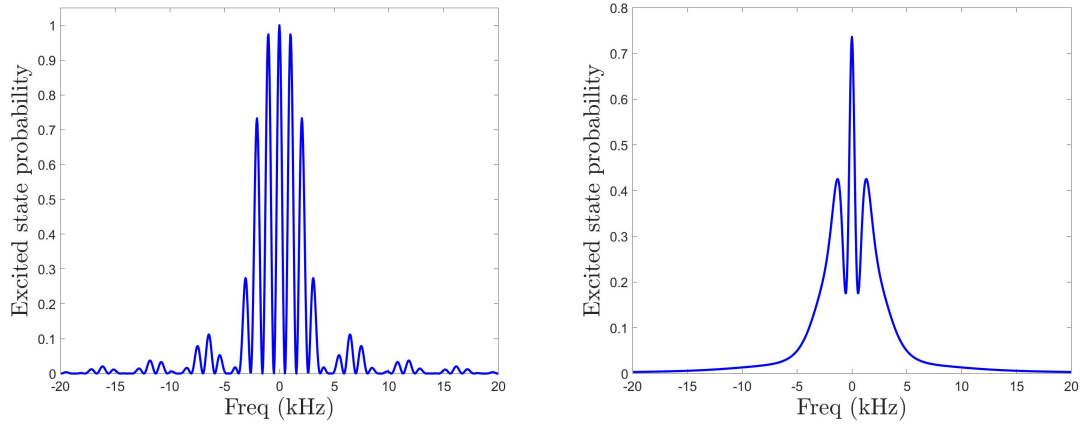
Figure 4.10: Ramsey spectrum with (left) and without (right) velocity averaging; note the loss of fringe structure.
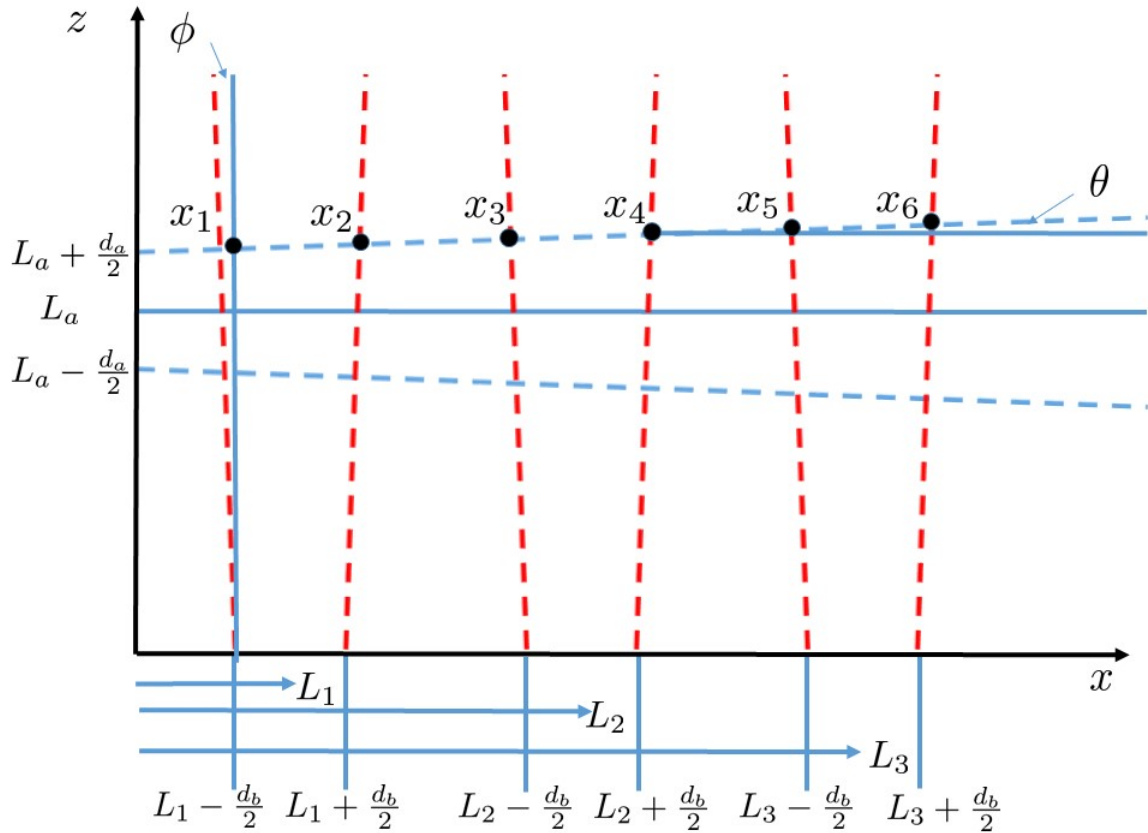
Figure 4.11: Depiction of the geometry of the (divergence) problem.

The geometry of the problem is depicted in Figure (4.11). Although the atom number transverse to the atomic beam direction has a Gaussian profile (see Figure 3.4c), we model the atom beam as having a square profile (e.g., "hard edges" with uniform atomic density inside the beam) for simplicity. (Earlier work has shown that the difference between a Gaussian pulse and a square pulse of equal area is minimal [30].) We make a similar assumption about the laser beam profile. Due to the cylindrical symmetry of the problem, we reduce the inherently 3-dimensional problem into a 2-dimensional one. As shown in Figure (4.11), the longitudinal direction of the atoms is referred to as the x direction and the direction orthogonal to it is the z direction. Atoms emerge from an aperture of diameter d_a, the location of which defines the line $x = 0$, with an atomic divergence half-angle θ with respect to the longitudinal direction. The diameter of the laser beams (assumed to

58

be all the same) is known some distance L_a away from the center line of the aperture and all the laser beams are assumed to have the same half-angle divergence, ϕ. The z-position from which the atom emerges the aperture is denoted by z_a and varies between $L_a - \frac{1}{2}d_a$ and $L_a + \frac{1}{2}d_a$. We can see immediately the effects of atomic and laser divergence. First, consider the case of a perfectly collimated atomic beam but laser fields that are diverging. Atoms emerging toward the bottom of the aperture spend less time in the laser fields than do atoms emerging toward the top. By a similar argument, the atoms emerging toward the bottom of the aperture will experience a longer free evolution time than the atoms toward the top of the aperture.

In our simulations, we assume the atomic velocity distribution is well described by Equation (4.11a):

$$P(v) = \frac{2v^3}{v_o^4} e^{-v^2 v_o^2} \tag{4.11a}$$

and

$$v_{mp} = \sqrt{\frac{2k_B T}{m}}, \tag{4.11b}$$

where v_{mp} is the most probable velocity of an atom of mass m in an atomic source of longitudinal temperature T and where k_B is the Boltzmann constant [26]. In our simulations, we take $v_{mp} = 7$m/s, which comes from the results of measurements we discussed in [1] and Section 3.3.3. We first define the Rabi frequency associated with a nominal π pulse as the Rabi frequency needed for an atom of velocity v_{mp} traveling through a collimated laser beam of diameter d_b to experience a perfect π pulse:

$$\Omega_\pi \frac{d_b}{v_{mp}} = \pi. \tag{4.12}$$

For the Ramsey interferometry sequence, the Rabi frequency associated with each beam of light is set equal to $\frac{1}{2}\Omega_\pi$.

Next, we determine the length of time that the atoms spend in each of the laser fields. Using simple geometry, we can determine the distances $x_2 - x_1$, $x_3 - x_2$, $x_4 - x_3$, etc. To find the time the atoms spend in the laser beam, we divide the distance $x_2 - x_1$ by the speed of the atoms. This speed is determined by randomly picking a velocity with a distribution given by Equation (4.11a). The free evolution time is determined in a similar way, using

the distance $x_3 - x_2$.

Atoms traveling at an angle θ interacting with a laser beam making an angle ϕ will see a different frequency due to the Doppler shift, $\boldsymbol{k}_{eff} \cdot \boldsymbol{v}$. For this geometry, the projection of $\boldsymbol{v}$ along the longitudinal direction is given by $v \sin(\theta + \phi)$. Here, $\boldsymbol{k}_{eff}$ is taken to be the k-vector associated with the ground state splitting in ^{85}Rb: $|\boldsymbol{k}_{eff}| = 2\pi \left(3 \times 10^9 \text{ Hz}\right)/c$. Notice, however, that the angle between the laser and the atom changes as the atom propagates through the laser field. Proper modeling of this effect would involve integrating the differential equation that led to Equation (4.6) but with a time varying Doppler shift. Other models have explored this effect and found that it is minimal and does not lead to a qualitative difference. For the case of co-propagating Raman fields, the correction is very small, since $|\boldsymbol{k}_{eff}| \approx 0$. However, this effect will need to be included in the case of counter-propagating Raman fields, since $\boldsymbol{k}_{eff}$ for that case can be taken to be $\boldsymbol{k}_{eff} = 2\boldsymbol{k}$, where $\boldsymbol{k}$ is the wave vector associated with the optical transition at $\lambda = 780.24$ nm.

The simulations were run for a fixed value of the atomic beam divergence θ and laser beam divergence ϕ. The results were run many times for varying velocity of the atoms, with a probability distribution given by Equation (4.11a) and averaged together.

Effects of Atomic Beam Divergence
This section is adapted from [25], an accepted manuscript of an article published by Taylor & Francis in Journal of Modern Optics on 12 November 2019, available online: https://www.tandfonline.com/doi/full/10.1080/09500340.2019.1688410.
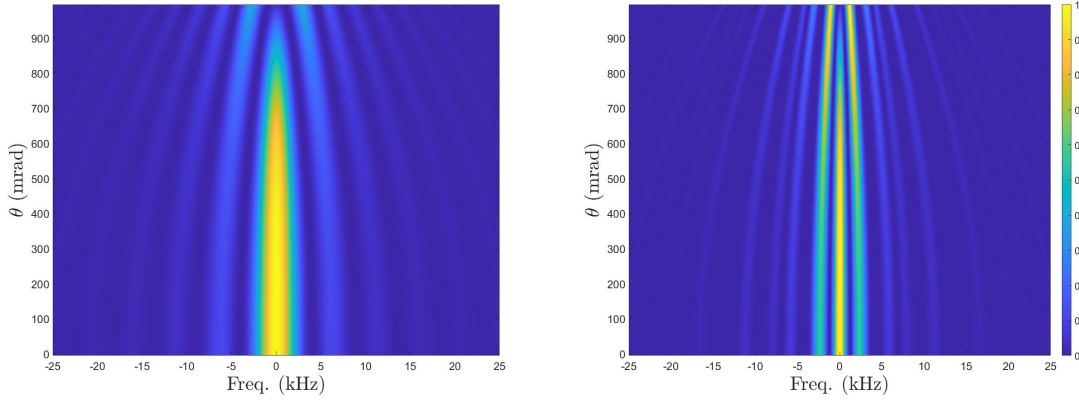
Figure 4.12: Raman spectrum (left) and Ramsey spectrum (right) as a function of frequency and atomic beam divergence angle, θ. The parameters in the simulation are $\phi = 0$, $v_{mp} = 7$ m/s, $d_b = 1.5$ mm, $L_1 = 10.2$ cm, $L_1 = 10.4$ cm, $L_1 = 10.6$ cm, chosen to match those of the experiment.

In this section, we consider the effects of atomic beam divergence. We first consider the case depicted in Figure [4.12] for a monoenergetic atomic beam with a divergence angle of $\theta = 1000$ mrad, which is much larger than the actual divergence in the experiment but chosen to illustrate the effects we are describing. Two effects can be seen in both plots. First, as the divergence gets larger, the atoms spend more time in the laser beams. In the case of the Raman spectrum, if the laser beam intensity is set such that an atom in a perfectly collimated atomic beam experiences a π pulse, then the atoms begin to experience a pulse area greater than π. Thus the central peak decreases in height and the end result of greater atomic beam divergence is less contrast. At the same time, the side lobes of the Raman Airy function, or the adjacent fringes in the Ramsey spectrum, experience increasing pulse area. Thus the height of these peaks increases and the result of decreased contrast is exacerbated.

Whereas the first effect of atomic beam divergence lowers the contrast via the amplitude, the second effect lowers it via frequency. The frequency spacing between the central peak and the first sidelobe (in the case of the Raman spectrum) depends inversely on the length of time the atoms experience a light field. Thus the spacing decreases, as manifested by the bright lines in the plot curving toward the central line, as divergence increases. Similarly, the interference fringe spacing in the Ramsey spectrum depends on the "dark time" or "free evolution time." If the laser beams are perfectly collimated, increased divergence of the

61

atomic beam means increased time spent in the dark and, again, the fringes curve toward the central peak. As this happens the fringes begin to overlap, and the trend of reduced contrast is reinforced.

Depicted in Figure (4.13) are the results of a simulation of a more realistic experiment in which we included velocity averaging. The inclusion of velocity averaging causes many of the finer details of the spectra to be washed out. In comparing Figure (4.12) with Figure (4.13), we see that after velocity averaging, only the main central peak remains in the Raman spectra and only the main central peak and one additional fringe remain in the Ramsey spectra. The contrast between the central peak and the first fringe remains good at these more realistic parameters. So, while this is good for the ability to conduct our experiments, the takeaway is that atomic beam divergence should be minimized as far as it can practicably be controlled.

Figure 4.13: Raman spectra versus atomic beam divergence angle with velocity averaging ($v_{mp} = 7$ m/s) (left). Ramsey spectra versus atomic beam divergence angle with velocity averaging ($v_{mp} = 7$ m/s) (right).

Effects of Laser Beam Divergence

This section is adapted from [25], an accepted manuscript of an article published by Taylor & Francis in Journal of Modern Optics on 12 November 2019, available online: https://www.tandfonline.com/doi/full/10.1080/09500340.2019.1688410.

Here, we consider the effects of laser beam divergence. Again, we first consider the effects

of laser beam divergence on an atomic beam with a single velocity group. The results of this simulation are depicted in Figure (4.14) (and the results with Doppler averaging included are depicted in Figure 4.15). The overall effect of laser beam divergence is the same as that of atomic beam divergence—reduced contrast. The magnitude of this effect, however, is much more pronounced. First, notice that the range of divergence plotted is only to $\phi = 10$ mrad, as compared to $\theta = 1000$ mrad in Figure (4.12). Second, even with the reduced range of divergence angle, we see greatly increased structure in both the Raman and Ramsey spectra. The change in the structure of the spectra, including, for example, the narrowing of the fringe spacing is again due to the increased path lengths that occur when divergence is taken into account. However, let us compare the effects of divergence. In the case of atomic divergence, the extra distance the atoms travel scales with d_b, which is on the order of 0.15 cm, whereas the extra time the atoms spend in a diverging laser beam scales as L_a, which is on the order of 20 cm, or two orders of magnitude larger. For that reason, we find the system is much more sensitive to the laser beam divergence than to the atomic beam divergence. What this means for our system is that minimizing laser beam divergence is much more critical that minimizing atomic beam divergence if we want to have usable signals with acceptable visibilities. This is fortunate since we have far greater control and "tunability" of the laser beam divergence than the atomic beam divergence. Though we can measure the atomic beam divergence of our system to confirm that it is within acceptable limits, we cannot easily alter it without significant changes to the apparatus. In contrast, due to the nature and layout of optics in our system, we can easily shape and subsequently measure the collimation of our laser beams in an unobtrusive manner.

One can also notice a sort of revival in Figure (4.14), which does get washed out when Doppler averaging is included as seen in Figure (4.15). For example, the population in the excited state for 0 detuning with 0 divergence angle is 1 and decreases with increasing divergence. The decrease is due to the fact that, since the atom spends more time in the laser field, the atom experiences *more* than a π pulse. As the divergence angle increases, the atom experiences increasing pulse area until the pulse area is 2π, at which time the population in the excited state is again 0. The pulse area continues to increase until it reaches 3π at which the population is again 1. However, we note that, while our model includes the effect of increasing beam size, it does not account for the decrease in Rabi frequency as the intensity decreases. The results of our modeling indicate that laser beam divergence is

already critically important at the 1-mrad level. Therefore, inclusion of the loss of intensity in our model would only sharpen that constraint and would not add any value to how the model informs our experiment (i.e., laser divergence must be minimized).
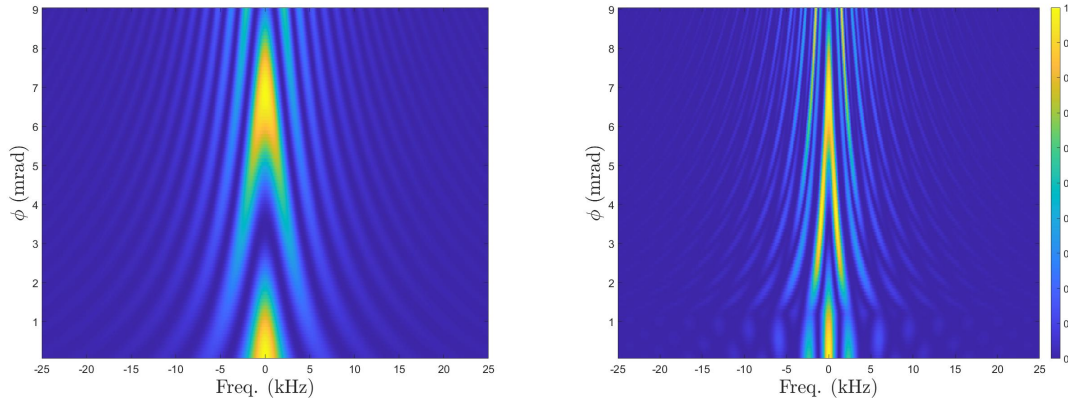
Figure 4.14: Raman spectra versus laser beam divergence angle without velocity averaging (left). Ramsey spectra versus laser beam divergence angle without velocity averaging (right).

Finally, we again consider the effect of velocity averaging, depicted in Figure (4.15). We see that many of the fine details evident in the plots with no velocity averaging have been washed out. The main peak and first sidebands still persist with good contrast, enabling interferometry with continuous beams. As with the atomic beam divergence effects, this allows us to proceed with the experiment, but demonstrates that laser beam divergence is a critical parameter that must be minimized. Note that this value is well within the range of divergence for which we would expect acceptable signal contrast as discussed earlier.
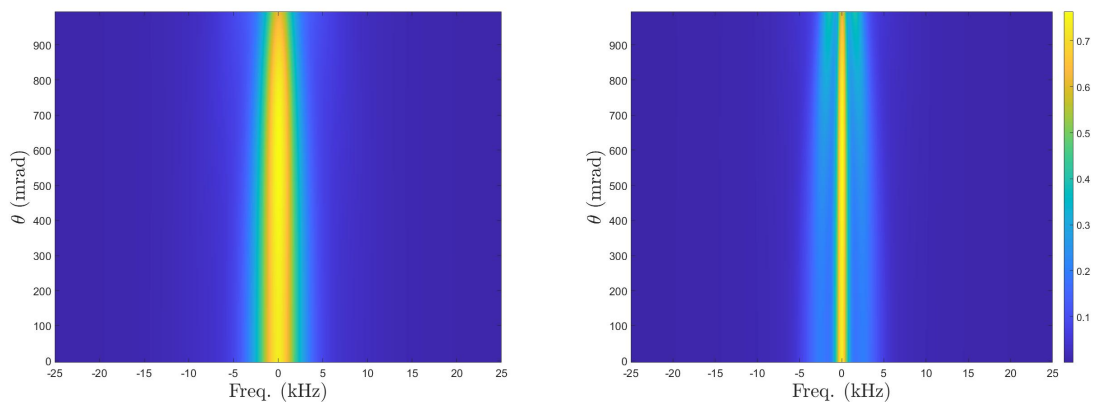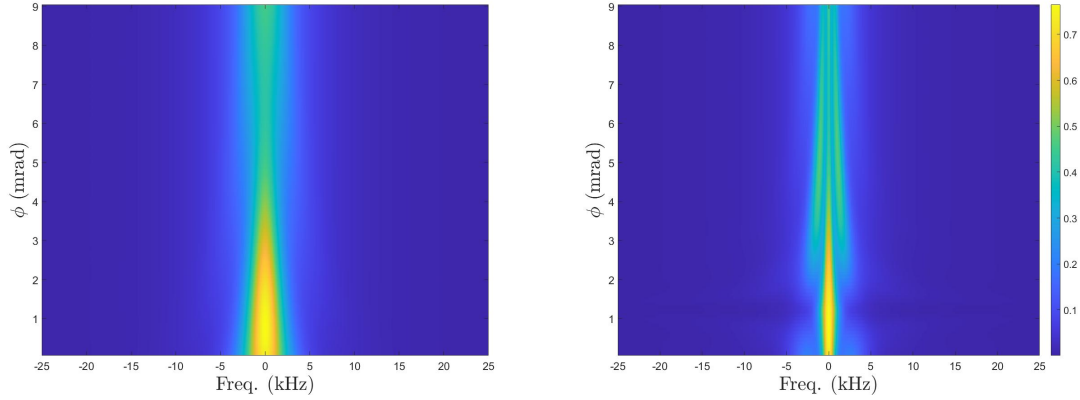
Figure 4.15: Raman spectra versus laser beam divergence angle with velocity averaging ($v_{mp} = 7$ m/s) (left). Ramsey spectra versus laser beam divergence angle with velocity averaging ($v_{mp} = 7$ m/s) (right).

4.7 Phase Shift

Our Mach-Zender interferomter's output is the number of atoms in the excited state. This varies with interferometric sensitivity as the result of phase shifts between the matter waves as they travel the two distinct paths. An interferometer subject to an acceleration will acquire a phase shift [1], [31]

$$\Delta\phi_{acc} = k_{eff}aT^2, \tag{4.13}$$

where k_{eff} is the effective laser wave number ($k_{eff} \equiv k_2 - k_1 \approx 2k$ for counter-propagating geometry), a is the magnitude of the acceleration, and T is the time between the light pulses that separate and recombine the waves. Similarly, an interferometer subject to a rotation will acquire a phase shift

$$\Delta\phi_{rot} = \frac{2m}{\hbar}2\boldsymbol{\Omega} \cdot \boldsymbol{A}, \tag{4.14}$$

where $\boldsymbol{\Omega}$ once again represents a rotation vector as in Chapter 1. The total phase shift is a combination of both such that

$$\Delta\phi_{total} = \Delta\phi_{acc} + \Delta\phi_{rot}. \tag{4.15}$$

These equations describe the effects of acceleration and rotation on a single interferometer.

65

Without external knowledge about what is happening to the system, the cause of the phase shift is ambiguous and one cannot discern the shift from acceleration from the shift from rotation. The key to unlocking that critical piece of information lies in the area vector $\boldsymbol{A}$. For any given rotation, this vector will have a given direction defined by the direction of the atoms' travel crossed with the wave vector of the Raman laser ($\boldsymbol{A} \propto \boldsymbol{v} \times \boldsymbol{k}$). By adding a second interferometer, based on an atom beam that is anti-parallel to the first, we now have an area vector whose orientation is opposite to the first for the same rotation. Thus we have a second set of *nearly* identical equations, with the difference being a reversal of the sign of the area vector. Figure (4.16) depicts how this looks in Cartesian space.
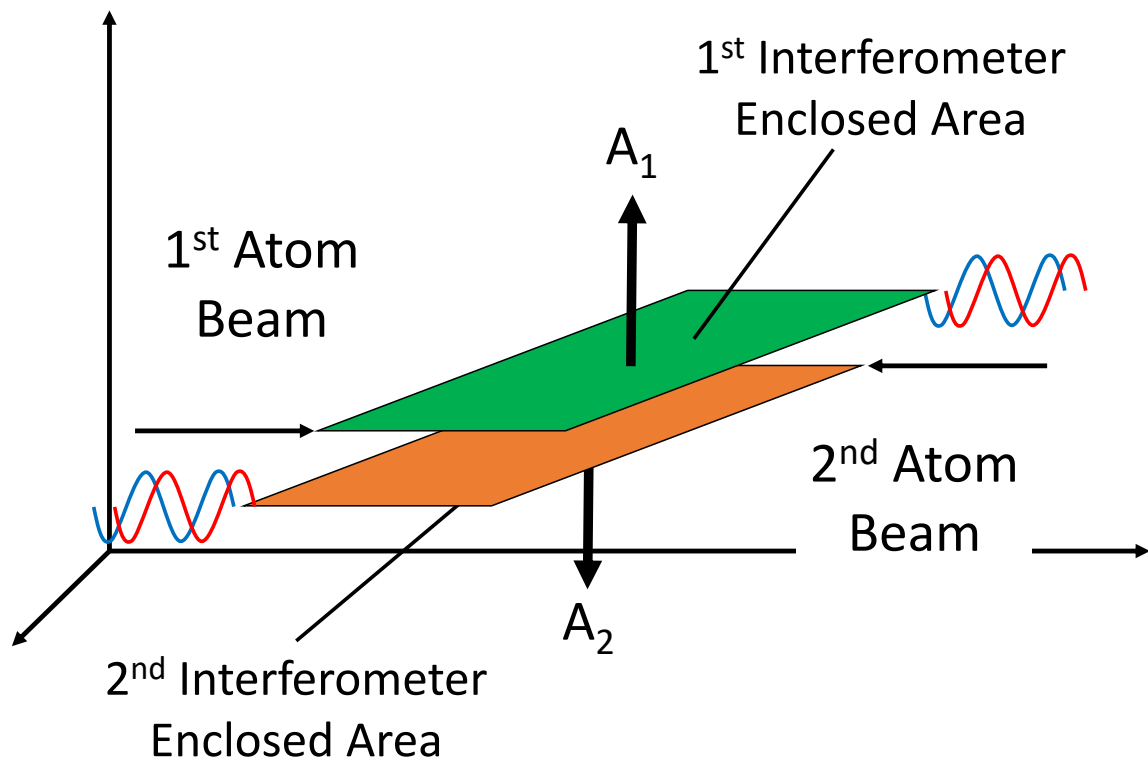
Figure 4.16: Depiction of the enclosed areas of two anti-parallel atom beams. The difference in sign between the area vectors is what transforms ambiguous interference explicitly into contributions from acceleration and rotation.

Since everything else is the same (same $\boldsymbol{\Omega}$ and same a), when we add the total phase

shifts from each interferometer, the contributions from rotation cancel out, leaving an unambiguous result due to acceleration:

$$
\begin{aligned}
\Delta\phi_{beam\ 1} + \Delta\phi_{beam\ 2} &= \Delta\phi_{acc,1} + \Delta\phi_{rot,1} + \Delta\phi_{acc,2} + \Delta\phi_{rot,2}, \\
&= \Delta\phi_{acc,1} + \Delta\phi_{acc,2} + \Delta\phi_{rot,1} + \Delta\phi_{rot,2}, \\
&= k_{eff}aT^2 + k_{eff}aT^2 + 2\boldsymbol{\Omega}\cdot\boldsymbol{A_1}/\hbar + 2\boldsymbol{\Omega}\cdot\boldsymbol{A_2}/\hbar, \\
&= 2k_{eff}aT^2 + 2\boldsymbol{\Omega}\cdot\boldsymbol{A_1}/\hbar - 2\boldsymbol{\Omega}\cdot\boldsymbol{A_1}/\hbar, \\
&= 2k_{eff}aT^2, \\
\Delta\phi_{beam\ 1} + \Delta\phi_{beam\ 2} &= 2\Delta\phi_{acc}.
\end{aligned}
\tag{4.16}
$$

Likewise, when we take the difference, the shifts from acceleration cancel out and we are left with the result from rotation:

$$
\begin{aligned}
\Delta\phi_{beam\ 1} - \Delta\phi_{beam\ 2} &= \Delta\phi_{acc,1} + \Delta\phi_{rot,1} - \Delta\phi_{acc,2} - \Delta\phi_{rot,2}, \\
&= \Delta\phi_{acc,1} - \Delta\phi_{acc,2} + \Delta\phi_{rot,1} - \Delta\phi_{rot,2}, \\
&= k_{eff}aT^2 - k_{eff}aT^2 + 2\boldsymbol{\Omega}\cdot\boldsymbol{A_1}/\hbar - 2\boldsymbol{\Omega}\cdot\boldsymbol{A_2}/\hbar, \\
&= 2\boldsymbol{\Omega}\cdot\boldsymbol{A_1}/\hbar + 2\boldsymbol{\Omega}\cdot\boldsymbol{A_1}/\hbar, \\
&= 4\boldsymbol{\Omega}\cdot\boldsymbol{A_1}/\hbar, \\
\Delta\phi_{beam\ 1} - \Delta\phi_{beam\ 2} &= 2\Delta\phi_{rot}.
\end{aligned}
\tag{4.17}
$$

In this sense, a single atom beam produces an *interferometer* whereas a second beam produces a *gyroscope*.

4.8 Systematic Shifts: AC Stark and Second-Order Zeeman Shifts

Unfortunately, acceleration and rotation are not the only things that produce phase shifts in these interferometers. The two primary undesirable phase shifts manifest in the experiments are *AC Stark shifts* and *second-order Zeeman shifts*. In the context of this research, the former are a result of an improper power ratio between the red- and blue-shifted Raman beams and the latter are a result of the applied magnetic field.

To see where the AC Stark shift comes from, we take another look at the reduction of a

three-level system to a two-level system through the adiabatic elimination of the third level (as in Section 4.1). Recall we replaced the Rabi frequency Ω with the Raman Rabi frequency $\Omega_R = \Omega_1\Omega_2/(2\delta)$ and single-photon detuning δ with two-photon detuning $\delta_2 - \delta_1$. The detuning actually contains an additional term which reduces to zero in the simple case where $\Omega_1 = \Omega_2$; once we transition to the actual experiment we cannot ignore it. The full detuning term is $\delta = \delta_2 - \delta_1 - \delta_{AC}$ where $\delta_{AC} = (\Omega_2 - \Omega_1)/(2\delta)$. This extra term is the AC Stark shift which "looks" like a detuning. Free evolution in Ramsey and spin echo occurs when the laser fields are off at a rate (in the rotating frame) given by $\delta_2 - \delta_1 = 0$, but the pulses excite the atoms more efficiently when $\delta_2 - \delta_1 - \delta_{ac} = 0$. For maximum excitation to occur at the same frequency as the free evolution frequency, it is important to "zero" the AC Stark shift. From theory and experiment we have operated at a 2.3 red-to-blue (frequency-shifted Raman laser beam) power ratio to eliminate the AC Stark shift. The optics, however, drift over time, and the sensitivity of the experiment to this parameter is very high. This results in having to stop work to readjust power ratios (and remeasure iteratively until the shift is minimized). Future improvements to the apparatus could include Raman beam intensity stabilization.

The latter of the shifts concerns atoms in magnetic fields (described in detail in [24]). When the magnetic field is small such that the energy shift due to it is smaller than the hyperfine splitting, the atomic levels shift according to the *linear Zeeman effect*. In this regime the energy level shift (due to a magnetic field) is a perturbation to the hyperfine interaction and leads to a frequency shift proportional to m_F; $\boldsymbol{F}$ is a good quantum number to use in this case (recall from Section (2.2) that $\boldsymbol{F} = \boldsymbol{J} + \boldsymbol{I}$ is the hyperfine structure). When the magnetic field is large such that the associated shift is larger than the hyperfine splitting, the atom is in a regime subject to the *Pashcen-Back effect*. In this regime the hyperfine energy is a perturbation to the interaction shift and $\boldsymbol{J}$ is a good quantum number to use (where $\boldsymbol{J} = \boldsymbol{L} + \boldsymbol{S}$ is the total electronic angular momentum).

In our experiment, the atoms are in an intermediate regime of magnetic field strength, where the primary effect is from the second-order Zeeman shift. The effect manifests itself according to the Breit-Rabi formula [24]

$$\frac{\Delta Frequency_{clock}}{B^2} = \frac{(g_J - g_I)^2 \, \mu^2}{2\hbar\Delta E_{hyperfine \; shift}}, \tag{4.18}$$

68

where g_J is the fine structure Landé g-factor, g_I is the nuclear g-factor, and $\Delta E_{hyperfine\ shift}$ is the hyperfine splitting. One can think of this effect as a correction to the weak-field linear Zeeman shift. For ^{85}Rb this translates to a theoretical second-order Zeeman shift of $8.12\ kHz/G^2$ (Figure 5.6 in Section 5.1.3 shows a measurement of this effect).

THIS PAGE INTENTIONALLY LEFT BLANK

CHAPTER 5:
Atom Interferometry: Experiment

5.1 Raman Spectroscopy

5.1.1 The Raman Laser

Both of our frequency-shifted Raman beams are derived from the same source, yet another distributed feedback laser (Eagleyard EYP-DFB-0780-00080-1500-TOC03). The frequency stability requirement is not as stringent as that of the other lasers. The cooling, repump, and detection lasers need to be stabilized to much less than a natural linewidth, which in rubidium is $2\pi\,(3\ MHz)$. On the other hand, we typically detune anywhere between $\approx 100-1000\ MHz$, so a drift on the order of $1\ MHz$ is insignificant. This alleviates the need for a SATABS setup and allows a simpler single-pass absorption cell setup to be used to monitor and sometimes lock the laser. The optics scheme for the light that goes to the experiment is depicted in Figures (5.2) and (5.1). The beam is oriented in a double single-pass configuration through an AOM (in this case a Brimrose GPF-1500-780 powered by an Analog Devices AD9914 3.5 GSPS direct digital synthesizer and radio frequency (RF) amplifier). A single pass produces a beam (1st *order*) that exits at an angle with a frequency shift determined by the RF driving the AOM (this beam carries $\sim 20\%$ of the incident light). The AOM produces an additional 0th *order* beam that passes straight through the AOM with no frequency shift (with the other $\sim 80\%$ of the incident light). By retroreflecting the 0th order beam one can produce an additional 1st order beam in the opposite direction, with a frequency shift of the same magnitude but different direction as the first-pass 1st order beam because the retroreflected beam and the AOM are automatically phase matched to a produce a 1st order beam in this direction. Thus the double single-pass configuration produces red/blue beams whose frequencies are shifted down/up by the RF driving the AOM. These two beams are then combined via a two-to-one polarization-maintaining (PM) fiber into a single physical beam of laser light (the "physical beam(s)" discussed in the the previous chapter).

AOM

0th Order
(No Shift)

Raman
Laser

Mirror

Blue(-shifted)
Beam

Red(-shifted)
Beam

2-to-1 Fiber to
Experiment

Dual-frequency
Light
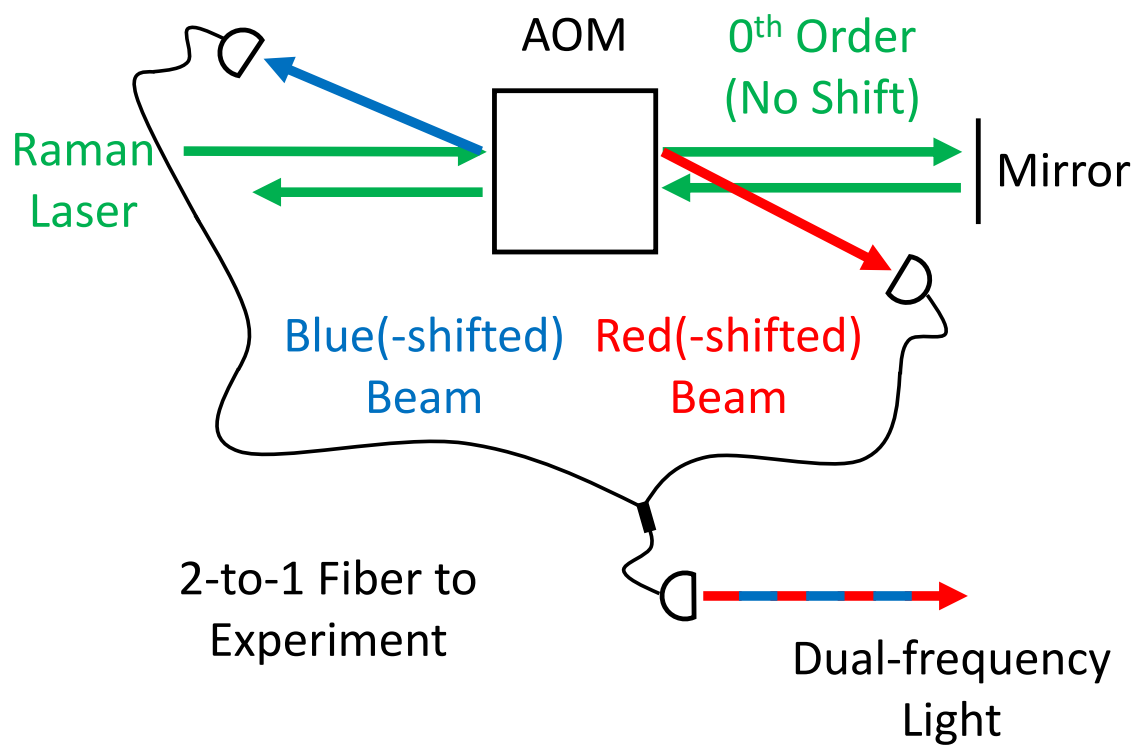
Figure 5.1: Depiction of the optics scheme used to create the two frequency-shifted Raman beams from a single laser. When the light from the Raman laser passes through the AOM, the 1st order beam is red-shifted by 1517.866 MHz. After retroreflection of the unshifted 0th order beam, the 1st order beam from the second pass is blue-shifted by 1517.866 MHz. These two beams are then combined via a 2-to-1 PM fiber and taken to the experiment.
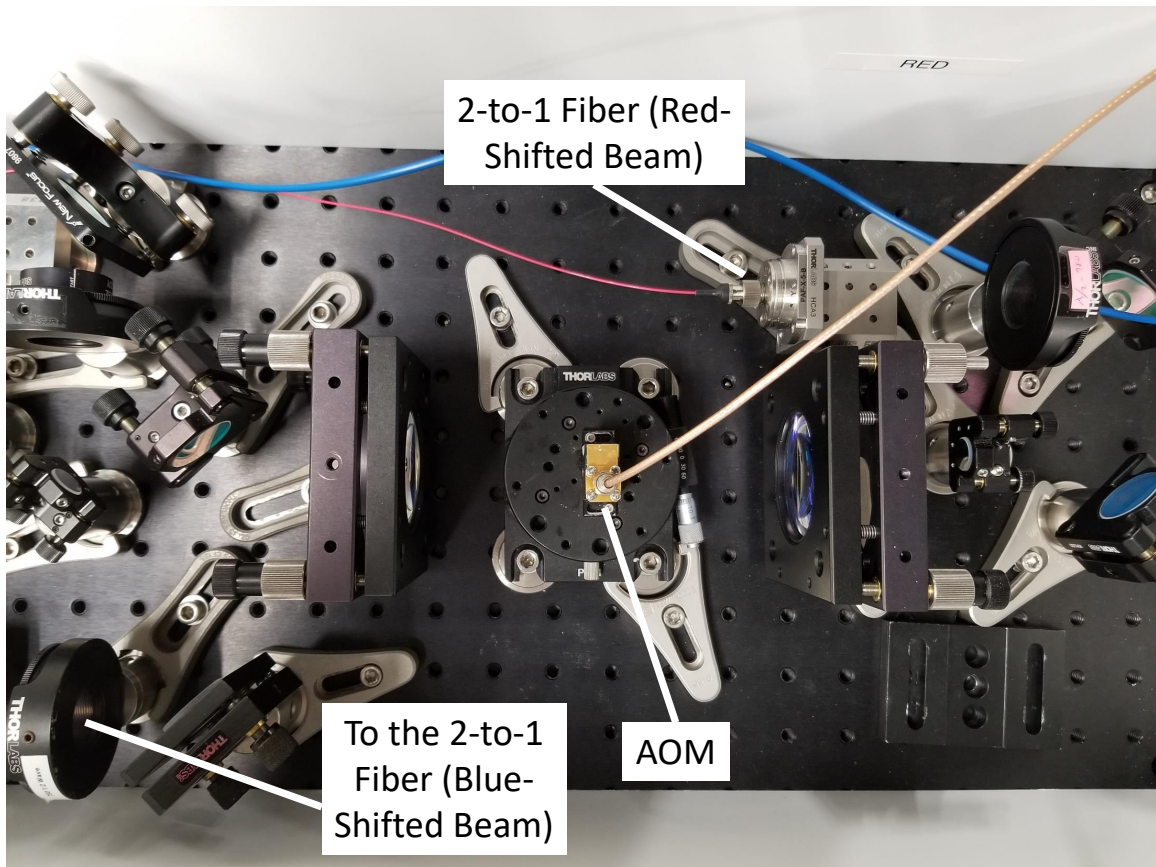
Figure 5.2: Photo of the optics scheme used to create the two frequency-shifted Raman beams from a single laser.

5.1.2 Physical Beams: Separate Beams

This section is adapted from [25], an accepted manuscript of an article published by Taylor & Francis in Journal of Modern Optics on 12 November 2019, available online: https://www.tandfonline.com/doi/full/10.1080/09500340.2019.1688410.

The physical Raman beams mentioned in Chapter 4 can be produced in different ways. We have used two methods in our experiment: one with individually controllable beams, which I will describe here, and one with a mask put in the path of a single, large beam, which I will describe in Section 5.1.3. With this first method, by carefully controlling the width, intensity, and detuning of the beams, we optimize the Raman spectrum. Since a π pulse is

one condition of an optimized spectrum, we then infer that on-resonance atoms in the most probable velocity class are experiencing π pulses. Figure (5.3(a)) is a photograph depicting the beams and Figure (5.3(b)) is a plot of the cross-section of the beams. With the actual experiment, we control the height and width of the Raman beams using a combination of cylindrical and spherical lenses to optimize for two different parameters. The major axis (height) of the optical beam is matched to the vertical extent of the atomic beam. The width of the Raman beams is optimized for creating optimal π pulses by the aforementioned method of optimizing the Raman spectrum. The end result is a pair of elliptical physical beams. Like the detection beam, these beams are still carefully collimated to ensure acceptable signal contrast. The atoms' transit time through these beams result in the atoms experiencing a pulse of light.

Our apparatus is designed to produce Raman spectra or Ramsey interference (or spin echo interference, but not using this physical beam method). Thus we have the ability to have one (for Raman spectroscopy) or two (for Ramsey spectroscopy) beams interacting with the atom beam. As shown in Figure (5.3(c)), the light from the Raman laser passes through a polarizing beam-splitting cube (PBS) along with multiple half-wave plates (HWPs) and mirrors to yet again be two physical beams (each containing the two required frequencies). We have the ability to control the power and polarization of the beams separately, as demonstrated by the unequal heights of the cross sections of the laser beams depicted in Figure (5.3(b)). To produce a Raman spectrum, one physical beam is blocked; for Ramsey interference both beams are let through into the vacuum chamber.
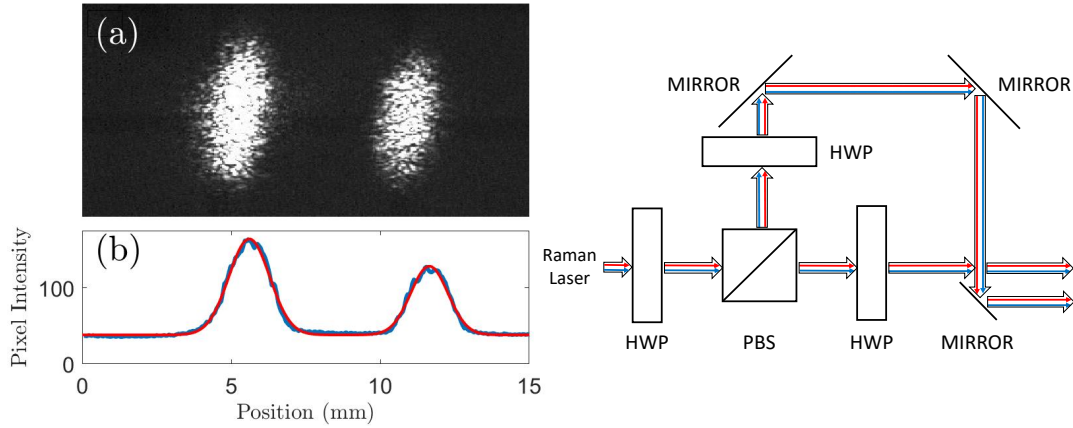
Figure 5.3: Photograph of physical beam spacing (a). Intensity plot of the beams made by taking the average of the vertical pixels (b). The blue line is the actual data and the red line is a double Gaussian fit. Optics used to make two physical Raman beams (c). Each physical beam includes red- and blue-shifted constituent beams which are physically right on top of each other but shown as separate beams here for clarity.

With one physical beam blocked and the first half-wave plate rotated to produce maximum power in one beam, we are left with one nominal π-pulse beam shining through the vacuum chamber window, which can drive Raman transitions. Typical spectra are depicted in Figure (5.4) (of note, all spectra are of beams in the Doppler-free configuration until Section 5.4 where I will specifically address the Doppler-sensitive configuration). Figure (5.4(a)) is a complete scan showing all 11 possible Raman transitions. Figure (5.4(b)) is a narrower scan about the central *clock* transition (so-called for its use in atomic clocks). The centered frequency $\delta = 0$ corresponds to $\omega_2 - \omega_1 - \Delta = 0$ or $2 \times 1517.866 \, MHz - 3035.732 \, MHz = 0$, where $3.0357 \, GHz$ is the ground state hyperfine splitting in ^{85}Rb. We typically use a red-to-blue power ratio of 2.3 to eliminate power-dependent AC Stark shifts (empirically determined), with the polarizations of the red and blue constituent beams matched (parallel linear). A downstream quarter-wave plate changes the linear polarization to same-handed circular polarization.
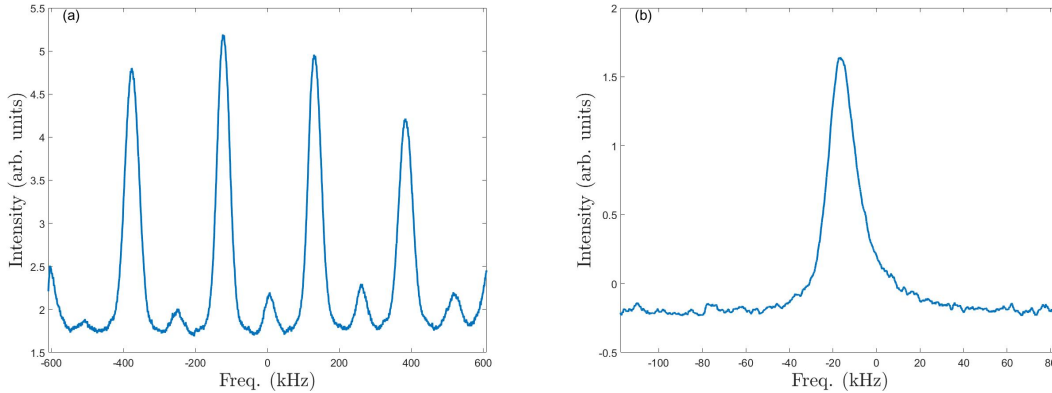
Figure 5.4: Experimentally measured full Raman spectrum in the Doppler-free configuration (a). Experimentally measured clock transition in the Doppler-free configuration (b).

Total beam power was relatively low (typically less than 5 mW as measured prior to the atom beam) due to sequential losses in the optics setup. Additional power may help the signal as this power level is in the power-limited regime (this was an assumption while operating in this setup but was later confirmed with measurements with the results depicted in Figure 5.9). However, while using this physical beam method, we did not want to use a tapered amplifier to increase the optical power to avoid any undesirable effects. The tapered amplifier has a low power but broadband emission regardless of the frequency of the seed laser, so there is guaranteed to be some unwanted resonant light (*amplified stimulated emission (ASE)*). By carefully selecting the output parameters of our RF source, we were able to measure all 11 Raman peaks in the arbitrary magnetic field present in our lab. A combination of the magnetic sublevels of each manifold combined with selection rules results in 11 magnetically sensitive "paths." We added magnetic coils as well, which allow us to drive only the six even or five odd peaks as desired by adjusting the current through the coils (and thus the direction of the magnetic field; this technique is described in detail in [32]). We have typically adjusted the current such that the even peaks are prominent as these contain the zero (or clock transition) peak, which we will use for Ramsey interference.

5.1.3 Physical Beams: Mask Method

Rather than using optics to split the Raman beam into two identical (but separately controllable) physical beams, the mask method utilizes a mask to create nominally identical (and not separately controllable) physical beams from a single large Raman beam—up to three physical beams (unlike the previous method) thus also allowing for spin echo interference experiments. Figure (5.5) depicts the optics used in this method. A combination of diverging and converging lenses is used to create a single large collimated beam. Quarter wave-plates are used to ensure a necessary polarization condition just as in the previous setup scheme. Ideally, they would be placed in a collimated beam rather than a diverging one; but, the placement was necessary due to physical limitations of the optics breadboard. The first QWP is a "fixer" used to turn the likely elliptically polarized light from the PM fiber into completely linearly polarized light; the second one turns the light into circularly polarized light. (The half wave-plate and PBS are used as a power attenuator.) Figure (5.5) depicts a spin echo mask as an example, but we have a variety of 3D-printed masks with one, two, and three slits for Raman, Ramsey, and spin echo spectra, respectively.
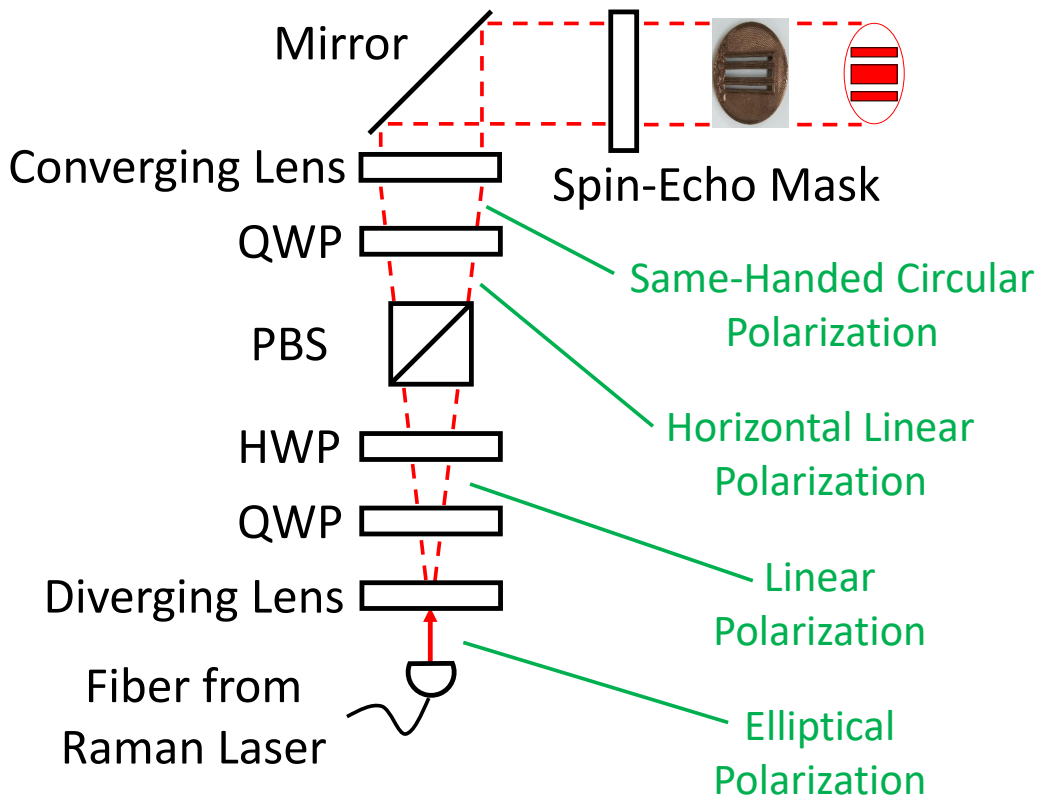
Figure 5.5: Depiction of the optics used to create the separate physical Raman beams from the single Raman laser. The beam size is manipulated so that a mask may be used to make the beams; as an example, this depiction shows a three-beam mask used for spin-echo interference. The polarization produced depends upon whether the configuration is Doppler-sensitive or not (this depiction shows same-handed circular polarization for a Doppler-free, co-propagating scheme).

The motivation for using this setup scheme in place of the separate beam method described in Section 5.1.2 is two-fold. First, while the previous method served a useful purpose in exploring incremental steps toward building an interferometer, there was no practical way of devising a three-beam setup in the previous method due to physical limitations of the optics breadboard and apparatus. Second, while it is often convenient in any experiment to have more "knobs" to turn, in this case we found it difficult to maintain proper operating conditions for great lengths of time. Multiple wave-plates must be precisely adjusted to ensure the beams are of equal power and polarization, and multiple mirrors must be precisely

adjusted to ensure the beams are parallel. The mask method addresses all of these concerns. It consistently produces identical (symmetric), parallel beams of the same polarization. If the power of the beams changes due to the drift of an optic or the laser power itself, the effect is common to each beam. Likewise, any AC Stark shifts, which are power dependent, are the same for each beam. Though they are outweighed by the advantages, this method does have some characteristics which are not desirable. Because the mask size is comparable to the size of the laser beam's Airy disc, the relative intensity of beams near to the edges is dependent on precise placement of the mask with regard to the center of the disc. Similarly, the intensity of the beams is dependent on the slit spacing of the mask (in that the greater the separation of the beams, the weaker their intensity). These disadvantages do not come into play for the central, single slit Raman configuration, but they will be a factor for Ramsey and spin echo interference. Finally, there is the fundamental presence of optical diffraction as the light passes through the slits. We projected the beam across the lab to look for diffraction effects in the far field. Diffraction was strongly present when the slits were $\sim 1\ mm$ wide, but not noticeable when the slits were $2\ mm$ wide (which became our normal operating slit width).

One final drawback of the mask method is the low intensity of the beams. The power coming out of the fiber is the same as in the previous method, but now it is spread out over a much larger surface area, resulting in a much lower intensity. Whereas we could avoid the use of an amplifier (and its associated ASE) in the previous method, we were forced to include one (another Thorlabs TPA780P20 Tapered Amplifier mounted on a Thorlabs LDC2500B Tapered Amplifier Controller) when using the mask method. For typical operating power levels we found the performance to be adequate, with the extra power (and signal) gained to be worth the addition of unwanted on-resonant ASE. In addition to providing increased power, the inclusion of the amplifier also allows for easy adjustment of the power level which is useful for characterization.

By using the two methods, we were able to characterize the experiment and measure a multitude of relevant parameters. One of the first steps in the Raman configuration is to set the conditions for an easily reproducible clock transition that occurs at the expected frequency. As discussed in Section 4.8, eliminating (or at least minimizing) the AC Stark shift is one requirement to do that. Recall that the AC Stark shift is proportional to $\Omega_2^2 - \Omega_1^2$ and inversely proportional to the single-photon detuning. Experimentally, this

meant measuring the clock transition at a relatively low physical beam power and checking the power ratio of the blue- and red-shifted beams. Then, we would raise the power and check for a frequency shift of the transition; if it shifted, different combinations of filters were placed in front of the beams to produce a different power ratio, followed by another physical beam power adjustment and check for a frequency shift. This iterative process resulted in a red-to-blue beam power ratio of 2.3.

Another requirement is to manage the magnetic field with the magnetic coils alluded to in Section 5.1.2. We include these coils for two reasons. The first is to isolate the clock transition. A magnetic field (with the appropriate strength) applied along the direction of propagation of the Raman laser beam(s) frequency shifts the other 10 Raman transitions farther away from the central clock transition and increases the signal of the transition [32]. The second reason is to minimize second-order Zeeman effects. Figure (5.6) depicts the clock transition peak position as a function of the applied magnetic field (in the direction of the Raman beams). A stray magnetic field can change the measured frequency of the clock transition and make it susceptible to inconsistent shifting. By controlling the applied field, we can ensure that the clock transition is measured at its natural frequency.
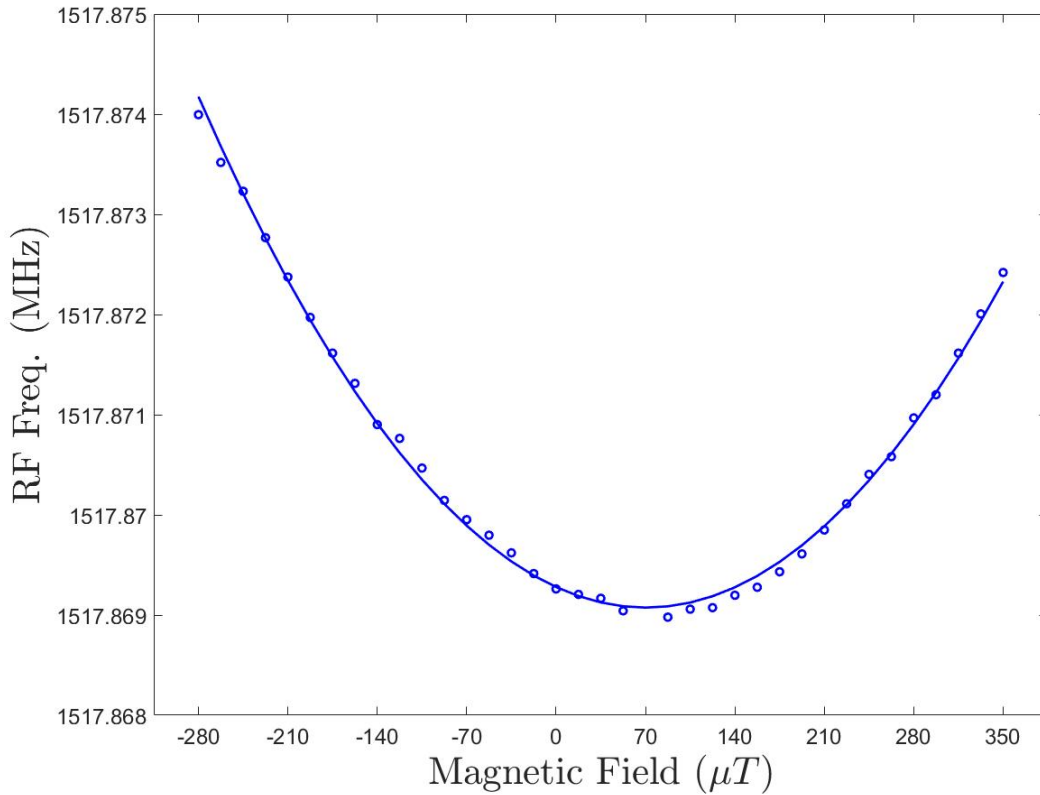
Figure 5.6: Experimentally measured clock transition position as a function of applied magnetic field.

With the frequency of the clock transition stabilized, we go back once again to signal optimization. In addition to all of the foundational steps described in Chapter 3, we have a few final adjustments to fine-tune: RF settings, detuning, and power of the Raman laser. Our primary lesson learned was to ensure the RF scan was slow enough relative to our detection scheme. The scan rate needs to be slow relative to the lock-in integration time yet not so slow as to impede efficient data collection or unnecessarily introduce undesirable signal noise from laser drift, temperature variations, etc. From theory we expect the signal to increase as detuning decreases, provided we do not get too close to resonance. Figure (5.7) depicts the Raman signal as a function of detuning in the full 11-peak case (we made the measurement without an applied magnetic field so the clock transition was small, thus the choice to measure the -1 or 5th peak from the left).
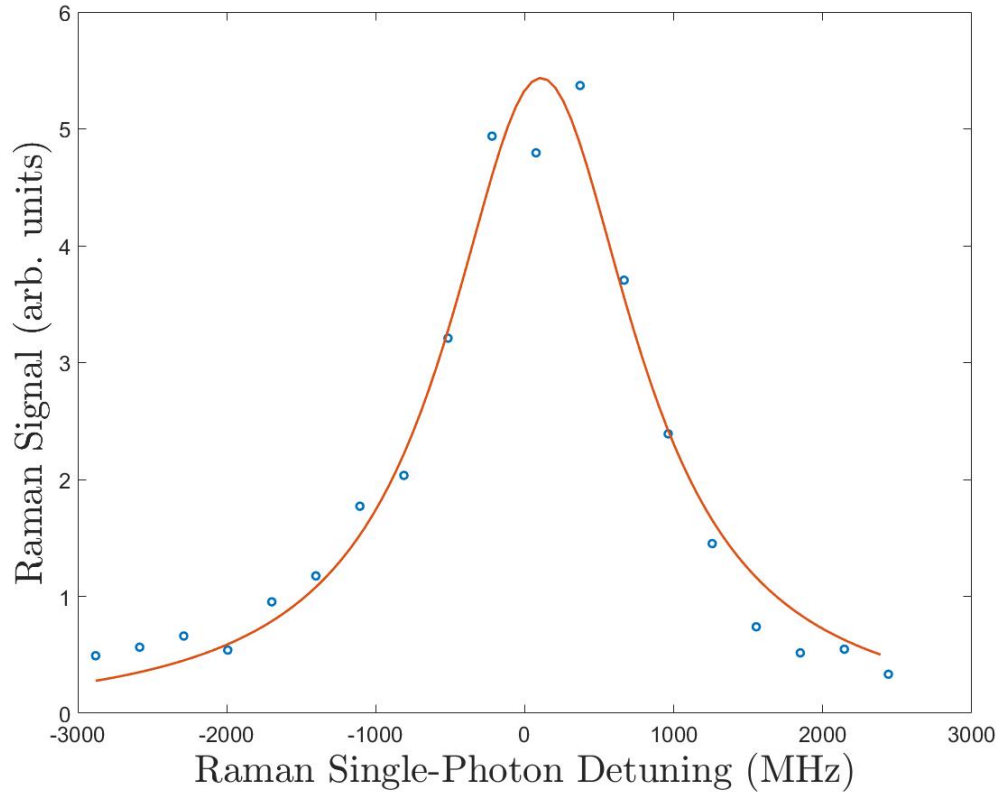
Figure 5.7: Experimentally measured signal of the -1 (or 5th peak from the left) of the full 11-peak Raman spectrum as a function of detuning. The data points are fit to $y = A/\left(B^2 + (t - t_0)^2\right) + c$, where $A = 3.31 \times 10^6 \ MHz^2$, $B = 776 \ MHz$, t is the detuning, $t_0 = 108 \ MHz$, and $c = -0.0705$.

We were able to repeat the measurement with an applied magnetic field in order to isolate the clock transition; see Figure (5.8).
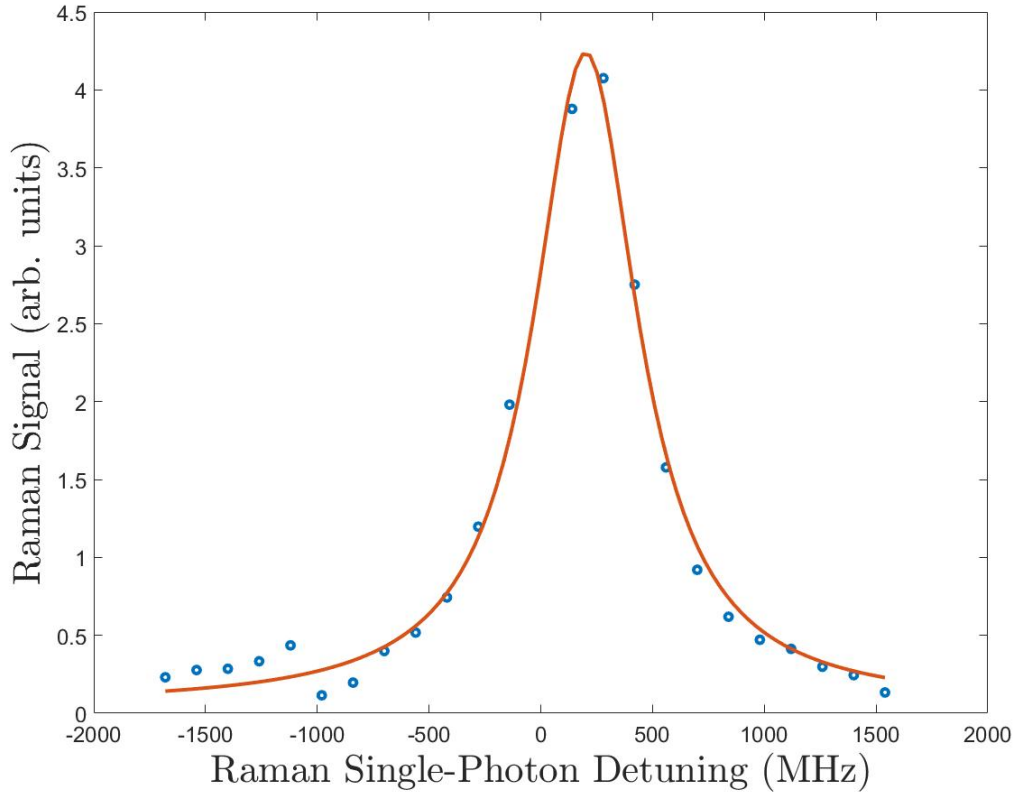
Figure 5.8: Experimentally measured signal of the clock transition as a function of detuning. The data points are fit to $y = A/\left(B^2 + (t - t_0)^2\right)$, where $A = 3.37 \times 10^{-5}\ MHz^2$, $B = 2.80 \times 10^{-8}\ MHz$, t is the detuning, and $t_0 = 2.00 \times 10^{-8}\ MHz$.

Finally, with the addition of the amplifier, we can evaluate the signal above background as a function of beam power. We expect the signal to increase up to a point before falling off again—this maximum is the π-pulse condition; Figure (5.9) shows the results of the measurement. Figure (5.10) shows a representative trace of an optimized Doppler-free Raman clock transition (with an applied magnetic field); the peak of this signal (along with the peaks from similar traces taken at different power settings) form the data points used for Figure (5.9). We took a similar measurement in Figure (5.11), but rather than plotting discrete data points we actively scanned the Raman laser power using an AOM. The results are similar to modeling in [1] and show Rabi oscillations as the laser power increases above the π-pulse condition.

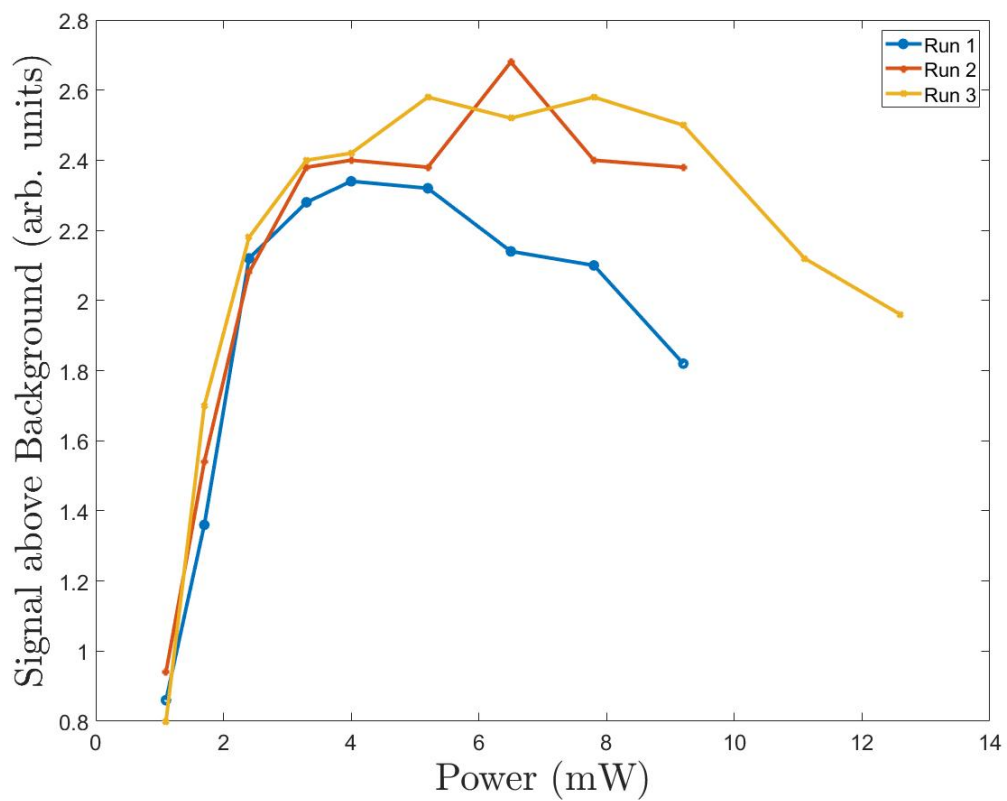Figure 5.9: Raman signal versus laser beam power. The RF scan settings were changed between runs 1 and 2 resulting in the slightly different curves.
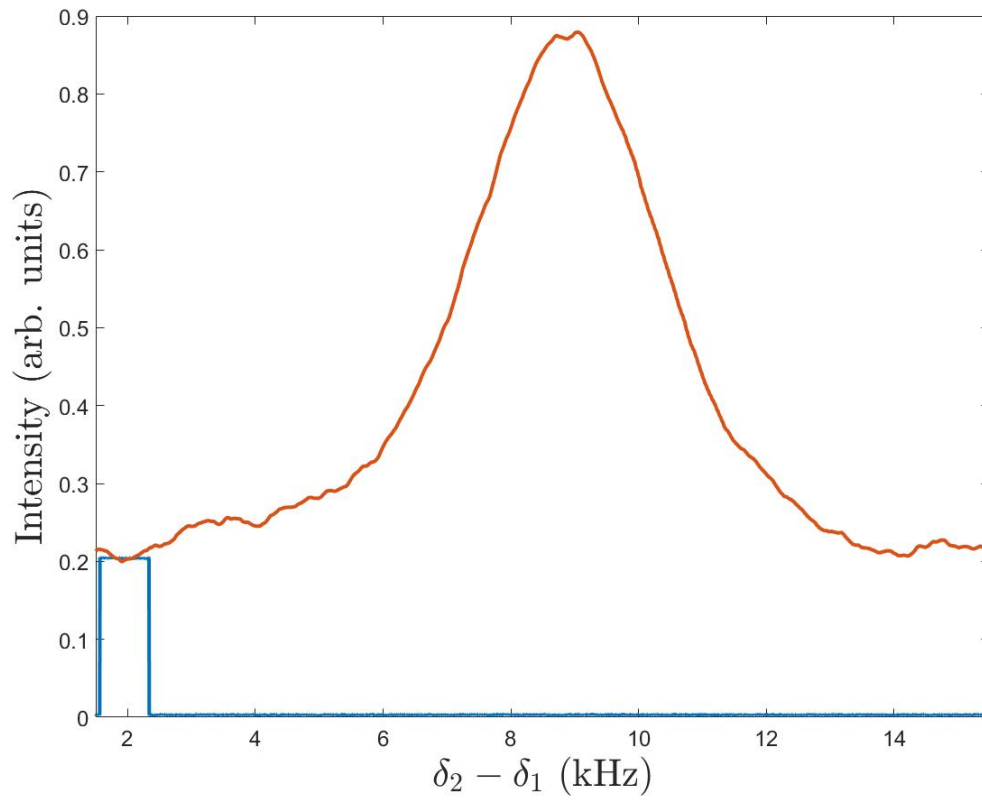
Figure 5.10: Experimentally measured Doppler-free Raman clock transition (plotted using a 100-point sliding average; orange trace is the measurement, blue trace is an RF trigger).
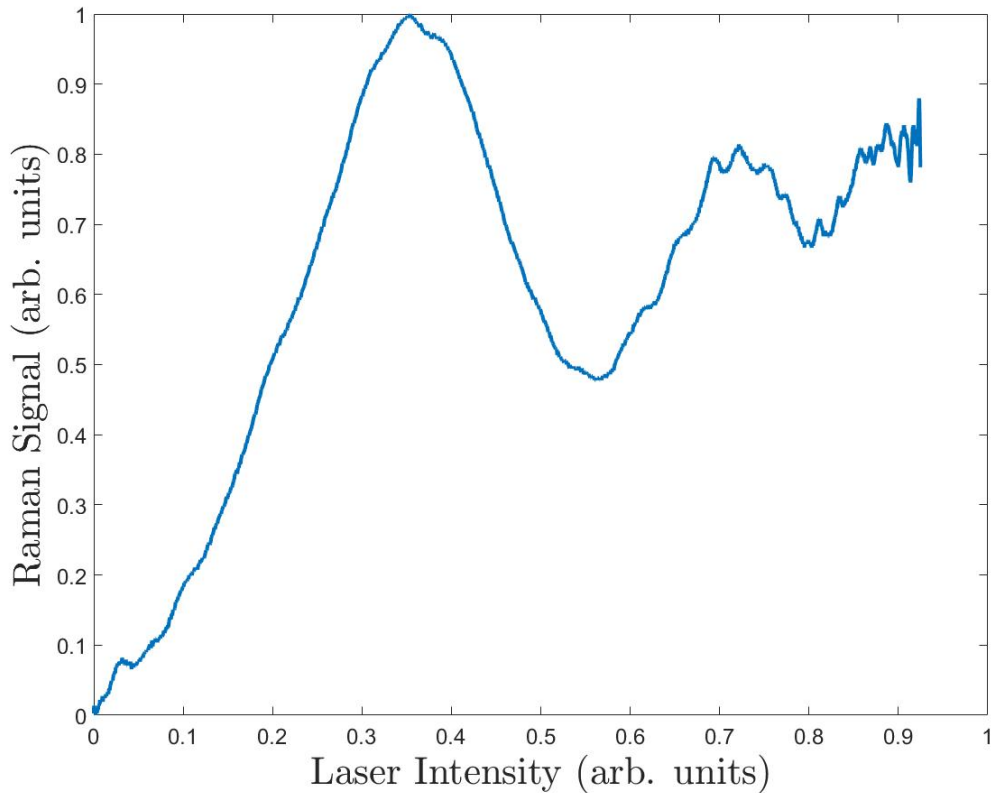
Figure 5.11: Rabi oscillations.

5.2   Ramsey Interference

Recall from Section 4.5 that Ramsey interference is a result of a $\pi/2 - \pi/2$ pulse sequence. This is a useful intermediate step as it represents the simplest form of atomic interference we can generate in the experiment. More importantly, it was crucial in that it demanded that all of our Raman settings were correct. We can only see it if the physical beams have acceptable coherence, geometry, and are truly providing the atoms with $\pi/2$-pulses (up to Doppler averaging). Figure (5.12) shows a representative trace of an optimized Doppler-free Ramsey interference pattern. (Note the asymmetry in the fringes. This effect is present in all of our measurements of Ramsey and spin echo interference. We suspect the asymmetry is a consequence of velocity averaging in the presence of AC Stark shifts, but we have not

been able to confirm this as of yet via theory or experiment—this will be the subject of future work in the lab.)
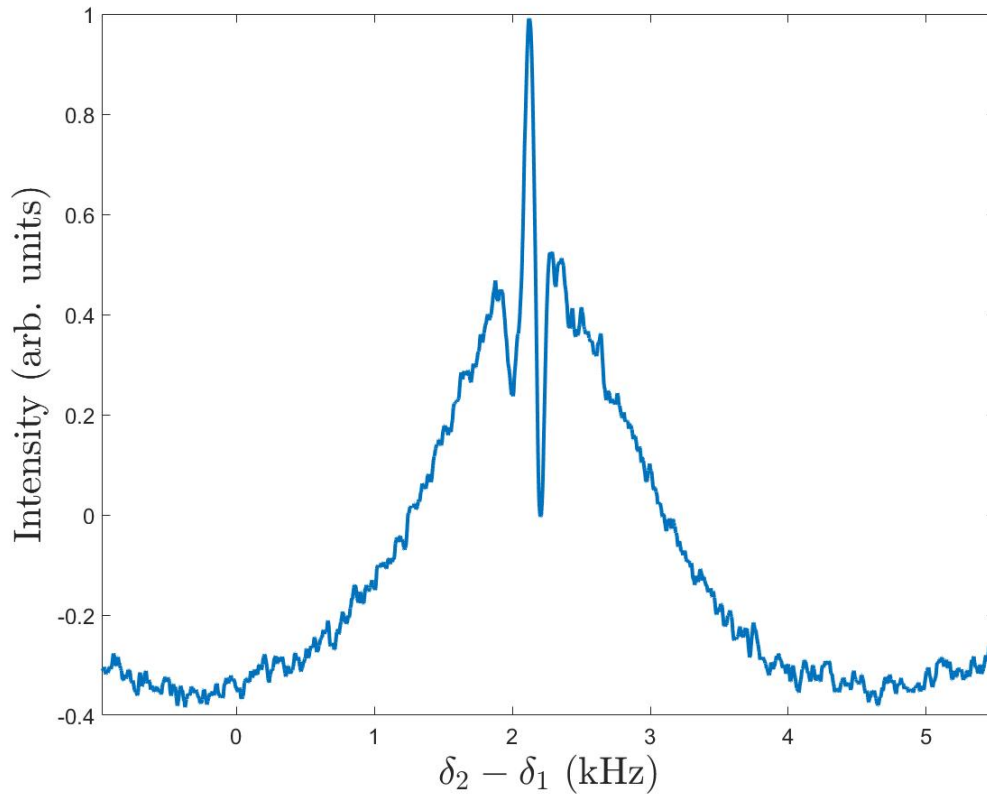
Figure 5.12: Experimentally measured Doppler-free Ramsey interference pattern.

This intermediate step provided us with more opportunities to optimize and characterize the experiment. Figure (5.13) shows coherence as measured by contrast in a Ramsey experiment as a function of detuning. Unlike the Raman signal that we expect to simply fall off with increasing detuning, as shown in Figure (5.8), the Ramsey signal is subject to competing factors.
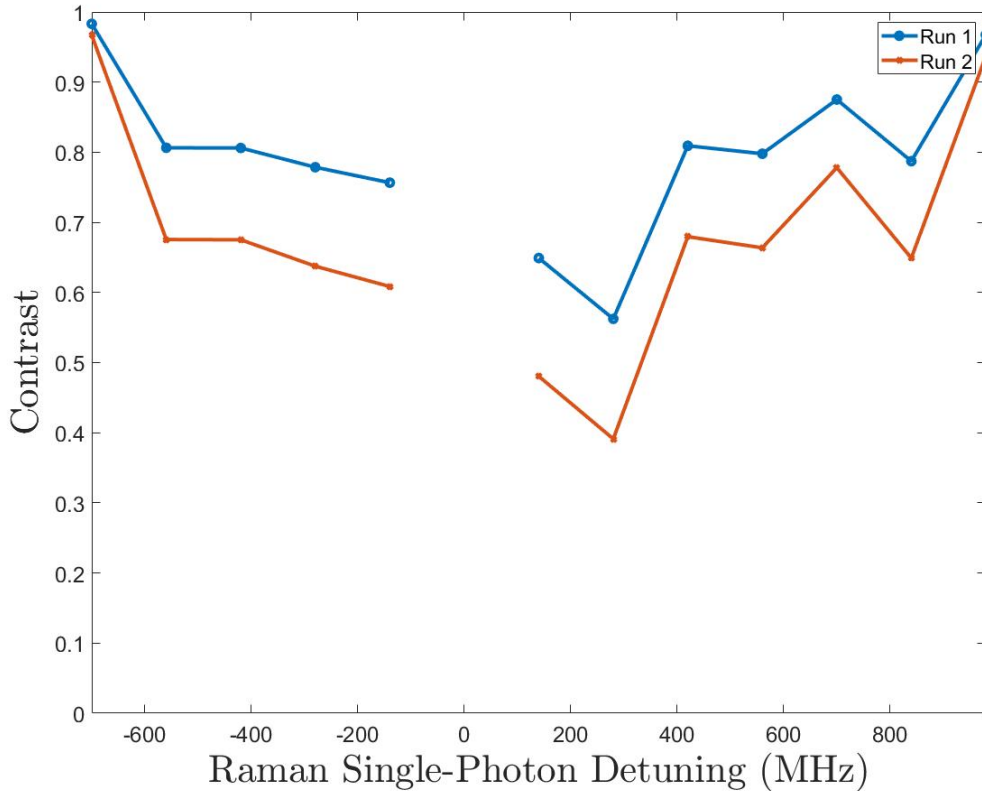
Figure 5.13: Experimentally measured signal of the Ramsey interference as a function of detuning.

First, I am defining "signal" here as a mix of SAB (as with Raman spectra) and *contrast*, which I define as

$$C = \left(Max - Min\right) / \left(Max + Min\right), \qquad (5.1)$$

where Min is the first local minimum to the right of the central fringe. The SAB should increase with decreasing detuning (as with Raman spectra). This is so because, if you assume for all power and detuning settings that you have something less than a π pulse, the closer you are the resonance, the closer you are to the π-pulse condition (with a larger signal). Contrast should remain fairly constant for all frequencies until one comes too close to resonance, at which point spontaneous emission cannot be ignored. This would imply an optimal operating detuning; Figure (5.14) shows Figures (5.8) and (5.13) normalized and overlaid on top of each other to illustrate the suggestion of an optimal detuning point

(maximizing signal without appreciably sacrificing contrast).
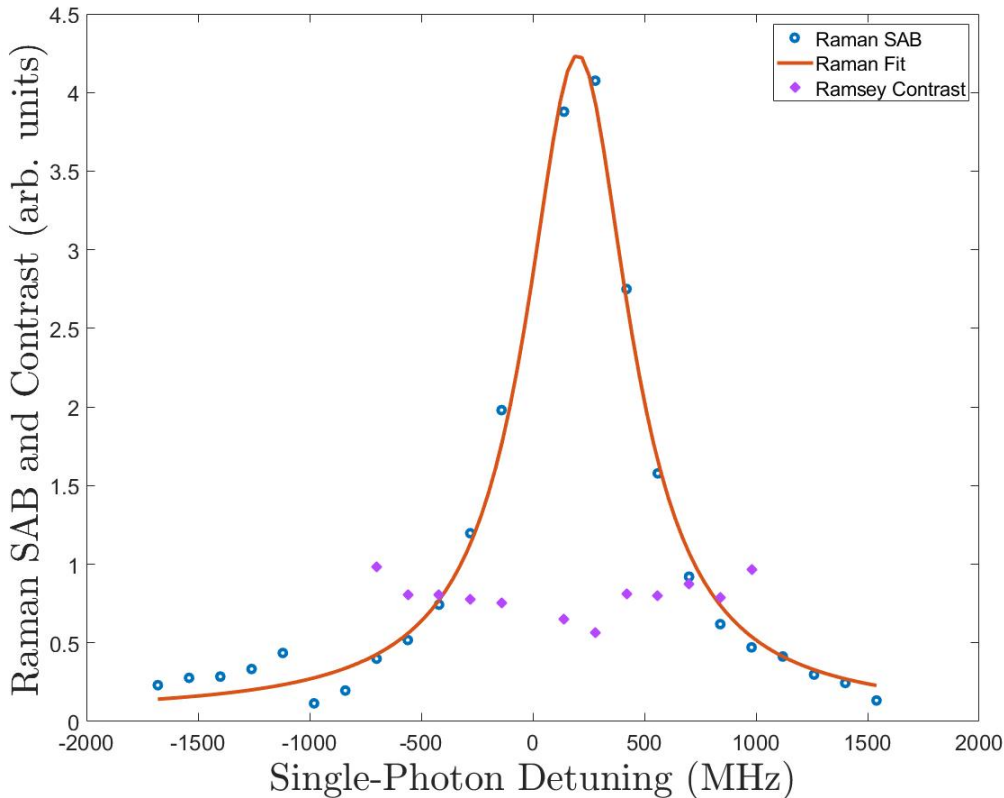
Figure 5.14: Experimentally measured Raman signal above background data points (blue circles), fit (orange trace, same fit parameters as Figure 5.8), and Ramsey contrast (purple diamonds) as a function of detuning.

One additional advantage of the mask method is the ease of varying slit separation (and height) as needed. Because each mask is 3D-printed and then placed inside an optics holder, the masks can be replaced in a matter of seconds. Figure (5.15) is a measurement of the fringe linewidth as a function of physical beam separation. Linewidth here is defined as the frequency difference between the center of the central fringe and the first trough to its right (higher frequency). Note that while the contrast does depend on power *balance* (between the physical beams), it remains constant as long as the power *ratio* (of the two frequency-shifted Raman beams) remains constant. Furthermore, the trough location does

not depend on power, so increasing the slit separation (with slits moving farther out in the Airy disk) does not affect the experiment. By this definition of linewidth, we expect it to vary inversely with beam separation [1]; all of our measurements are in qualitative agreement with this expectation.
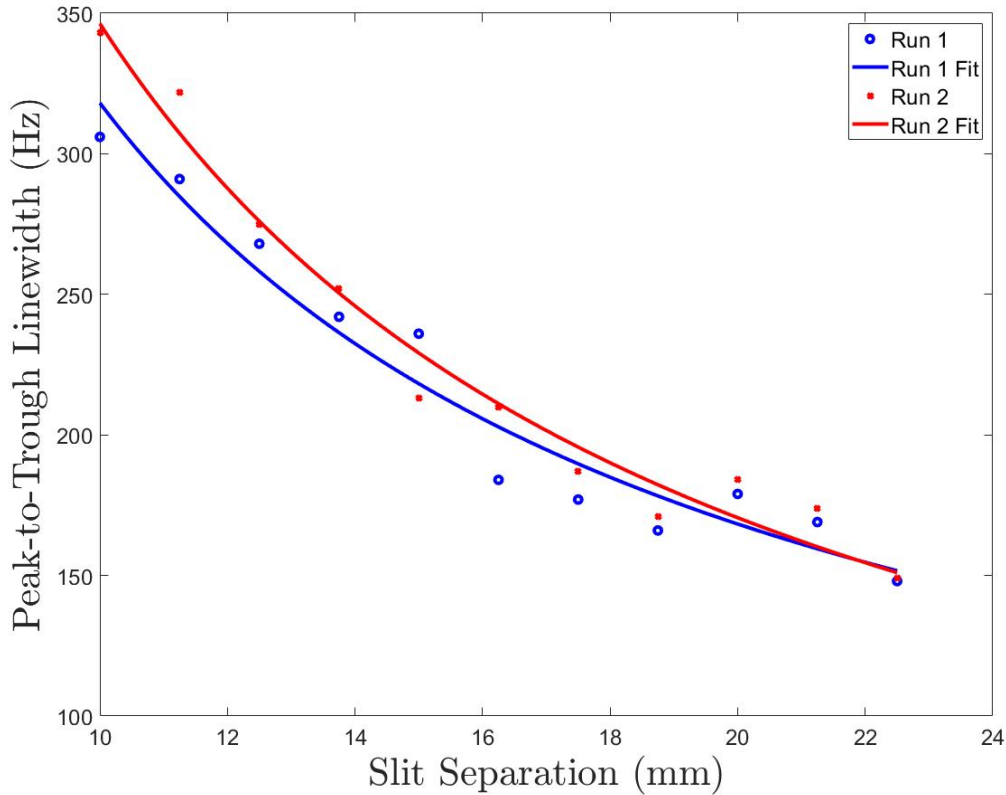
Figure 5.15: Experimentally measured Ramsey fringe linewidth (peak of the central fringe to the adjacent trough) as a function of physical beam spacing. The data points are fit to $y = A/d + c$, where $A = 2995\ Hz*mm$, d is the slit spacing, and $c = 18.6\ Hz$ for run 1, with $A = 3516\ Hz*mm$ and $c = -5.30\ Hz$ for run 2.

5.3   Spin-Echo Interference

Recall from Section 4.5 that spin echo interference is a result of a $\pi/2 - \pi - \pi/2$ pulse sequence. This is the full sequence that we use to close our Mach-Zender interferometer.

Figure (5.16) shows a representative trace of an optimized Doppler-free spin echo interference pattern. Here, we have used a mask with two slits surrounding a wider central slit. The slit widths are sized to mimic the $\pi/2 - \pi - \pi/2$ sequence, but there is some deviation as the intensity of the light is greater in the central slit compared to the outer slits due to the Gaussian nature of the laser beam.
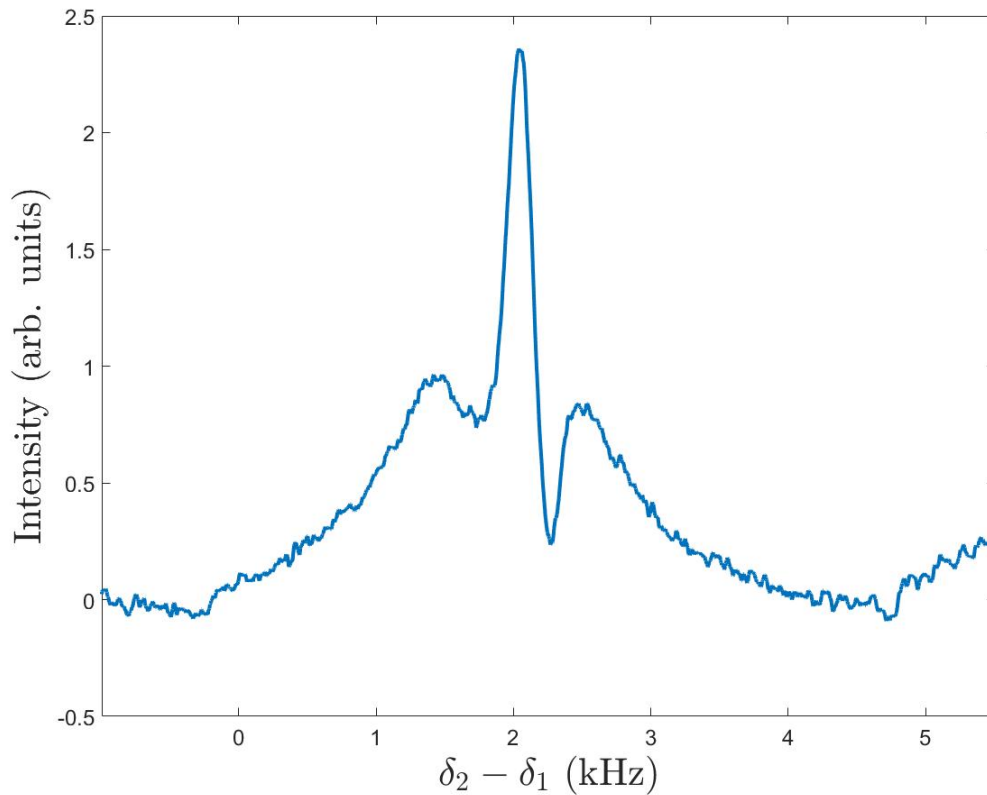
Figure 5.16: Experimentally measured Doppler-free spin echo interference pattern.

5.4 The Doppler-Sensitive Configuration

We discussed the counter-propagating Raman beam configuration that produces Doppler-sensitive spectra in Section 4.4—experimentally, this means removing the QWP in front of the vacuum chamber and adding a QWP and retroreflecting mirror on the far side of the vacuum chamber (see Figure 4.6). Recall that this is the type of signal necessary for an

inertially sensitive atom interferometer. We made many measurements in what I am calling the Doppler-sensitive *configuration* in what should have been one of the final steps on the way toward said interferometer. These include measurements of the Raman clock transition (Figure 5.17), Ramsey interference (Figure 5.18), and spin echo interference (Figure 5.19).

Figure 5.17: Experimentally measured Raman clock transition taken in the Doppler-sensitive configuration (plotted using a 100-point sliding average; orange trace is the measurement, blue trace is an RF trigger).
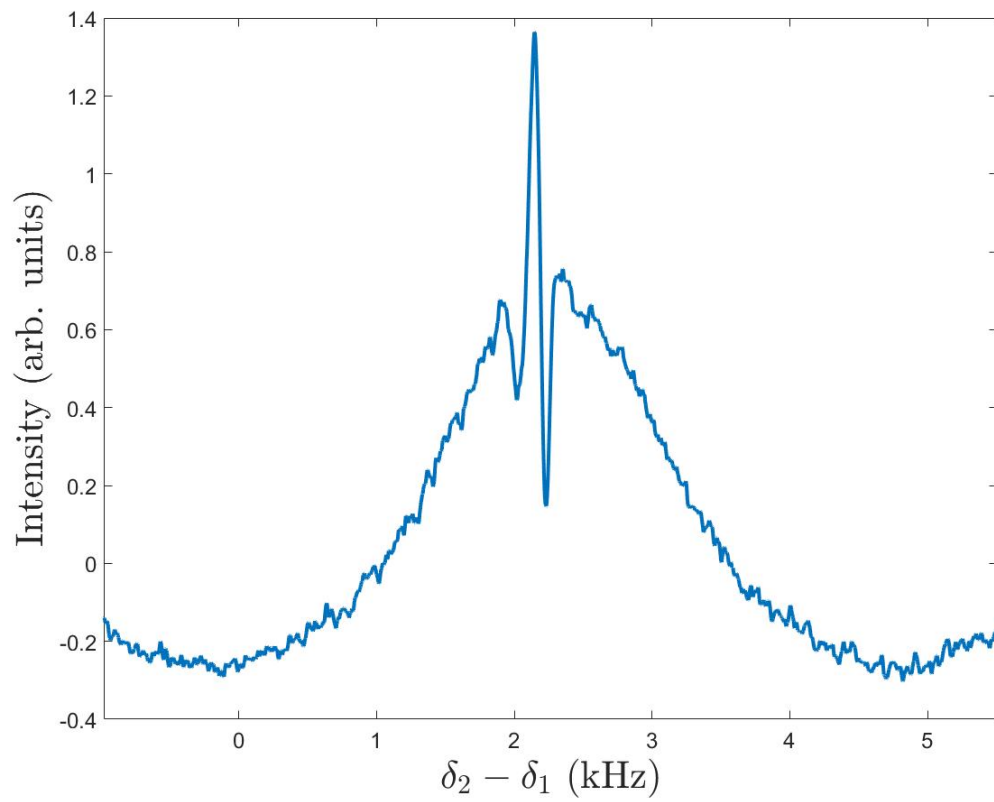
Figure 5.18: Experimentally measured Ramsey interference pattern taken in the Doppler-sensitive configuration.
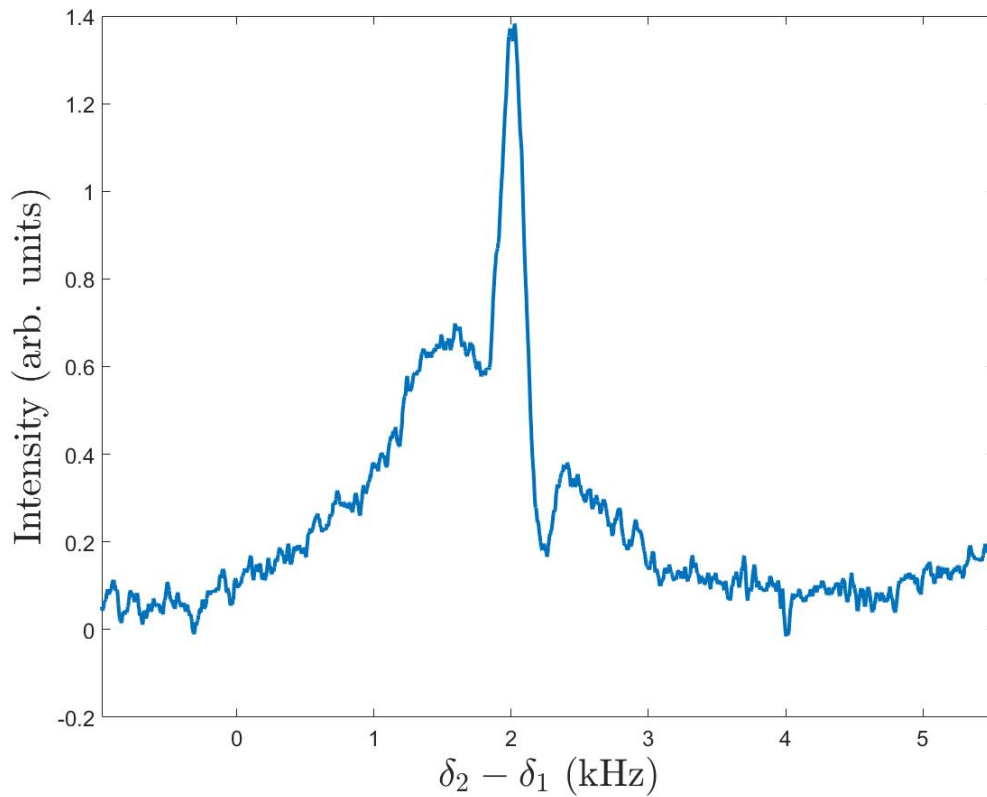
Figure 5.19: Experimentally measured spin echo interference pattern taken in the Doppler-sensitive configuration.

We also did some characterization akin to what we did for Doppler-free measurements; for example, Figure (5.20) depicts the linewidth of the Ramsey fringe as a function of beam spacing. This is similar to Figure (5.15)—in fact, it is *too* similar. We expect the same dependence but not the same actual values.
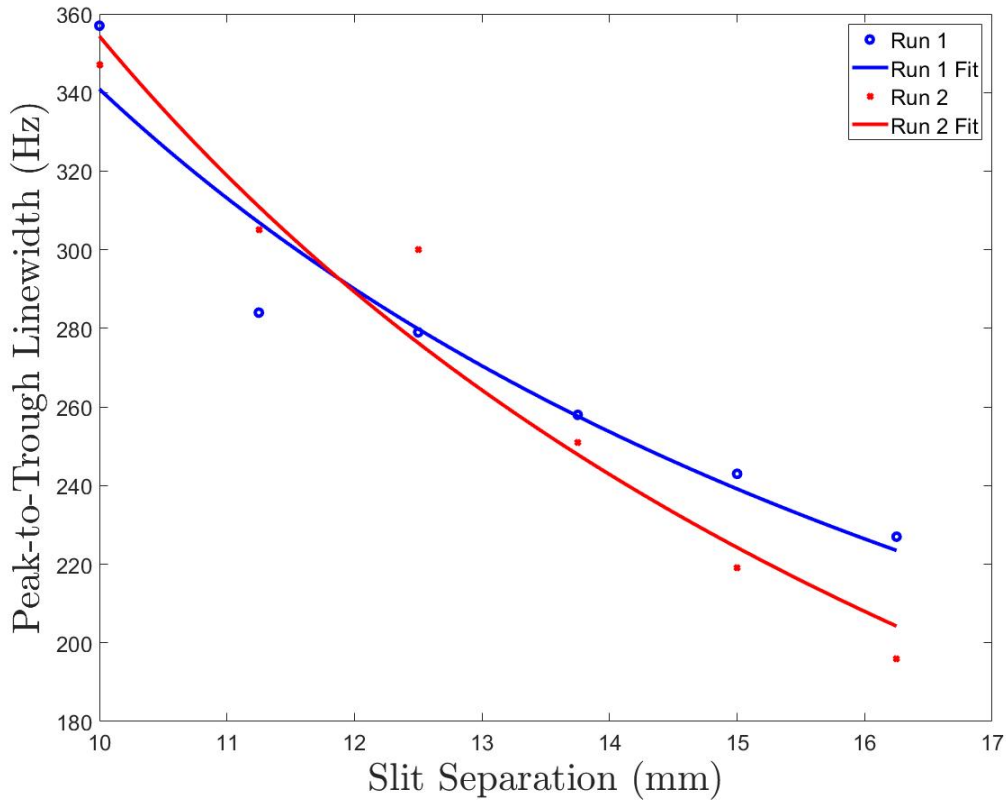
Figure 5.20: Experimentally measured Ramsey fringe linewidth (peak of the central fringe to the adjacent trough) as a function of physical beam spacing taken in the Doppler-sensitive configuration. The data points are fit to $y = A/d + c$, where $A = 3052 \ Hz * mm$, d is the slit spacing, and $c = 35.7 \ Hz$ for run 1, with $A = 3902 \ Hz * mm$ and $c = -35.9 \ Hz$ for run 2.

This motivated another look at the measurements of the Raman linewidth in both DF and DS configurations. For Raman spectra, we define linewidth the usual way (FWHM). We expect the linewidth of a Doppler-sensitive Raman peak to be much wider than the Doppler-free version (since it is average over a transverse velocity spread). This applies to Ramsey and spin echo interference as well since the Raman peak is the envelope within which fringes occur. We took fresh measurements of Raman and spin echo spectra (Figures 5.21 and 5.22, respectively) and confirmed our suspicion that what we had actually been measuring was not in fact Doppler-sensitive spectra, but rather Doppler-free spectra, with the retroreflected beams meeting the necessary polarization condition (recall Figure 4.8).
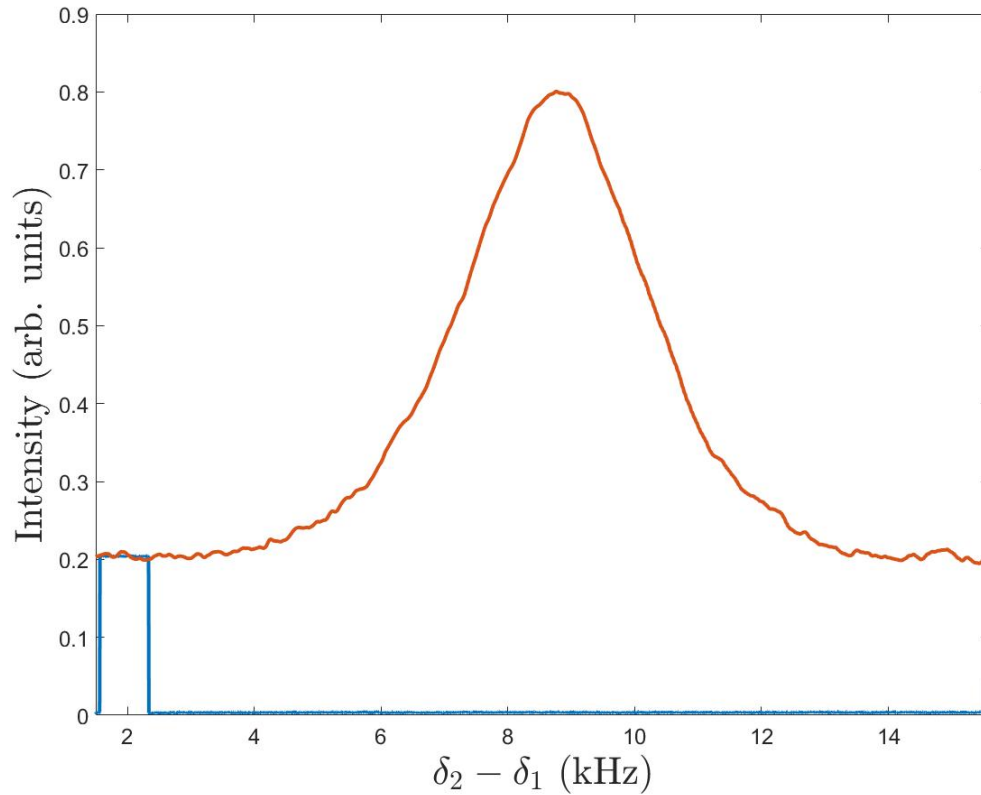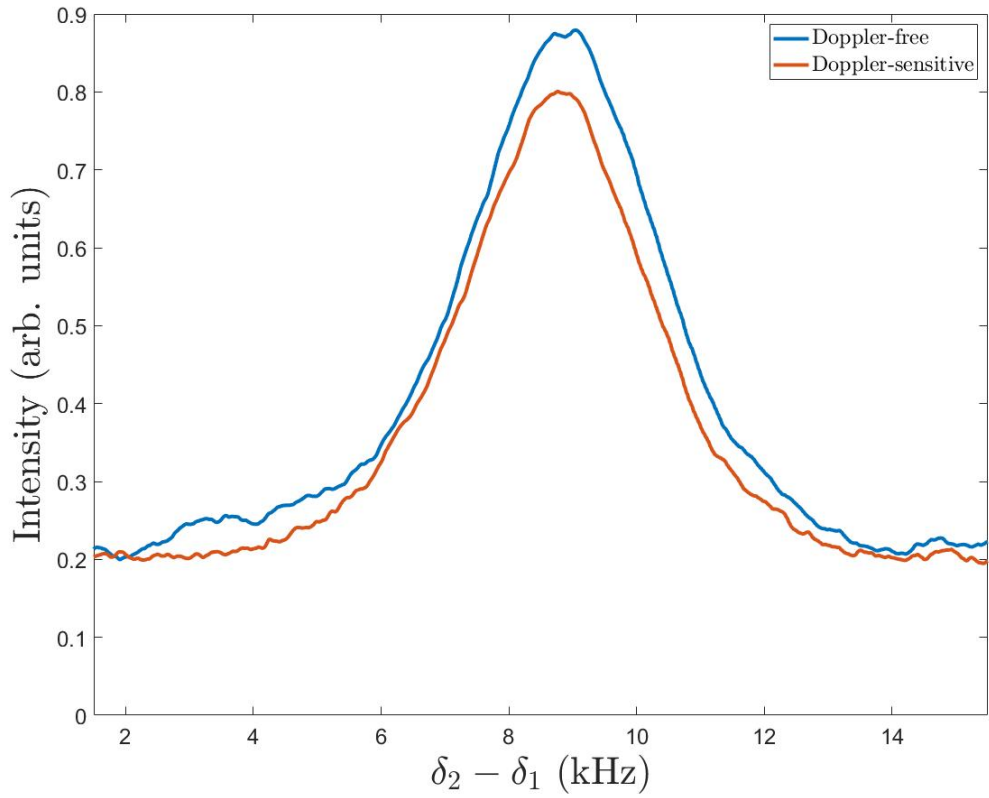
Figure 5.21: Experimentally measured Raman clock transition taken in the Doppler-free and Doppler-sensitive configurations (plotted using a 100-point sliding average); note the nearly identical linewidth, which indicates that the trace taken in the Doppler-sensitive configuration is actually retroreflected Doppler-free interference.
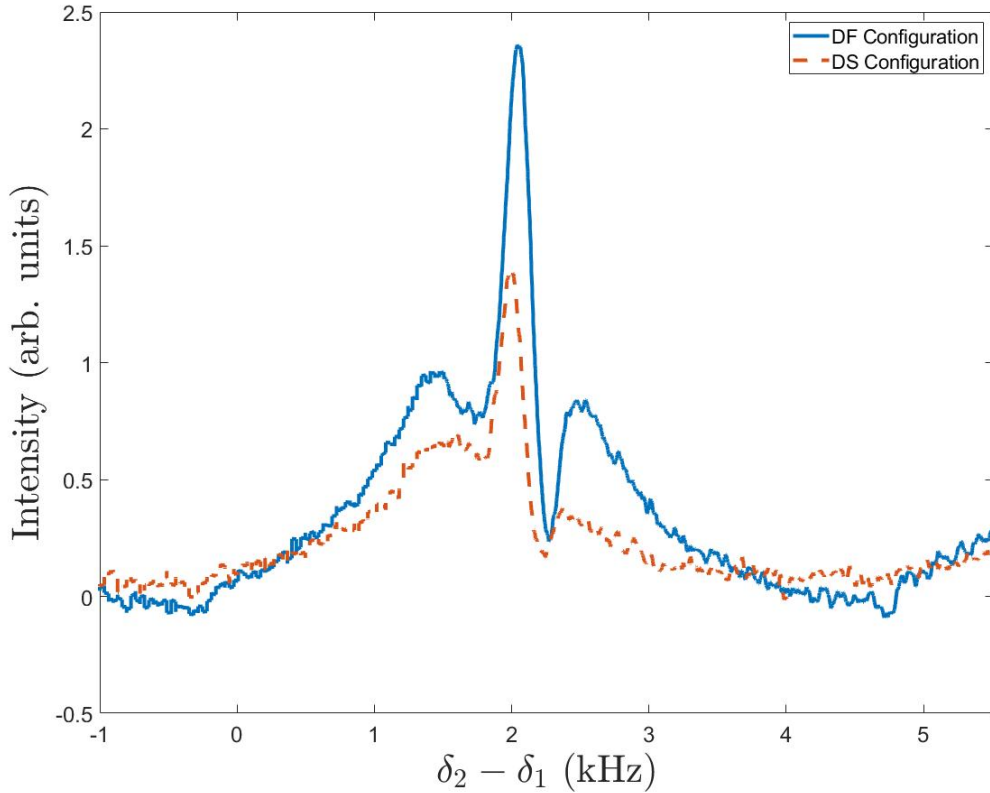
Figure 5.22: Experimentally measured spin echo interference pattern taken in the Doppler-free and Doppler-sensitive configurations; note the nearly identical linewidth which indicates that the trace taken in the Doppler-sensitive configuration is actually retroreflected Doppler-free interference.

Furthermore, though we did observe a reduction in signal in some cases (when switching to DS), this was not always so. We expect for the signal to be consistently and drastically reduced (for the same reason that we expect a wider linewidth, namely having to average over different velocity classes). The lack of signal reduction combined with the static linewidth when switching between our Doppler-free and Doppler-sensitive configurations confirms that the results produced in the latter configuration are indeed (retroreflected) Doppler-free spectra. Further work will be required to eliminate retroreflected Doppler-free spectra and enhance the Doppler-sensitive spectra. Likely this will involve a combination of additional atomic beam collimation, magnetic field tailoring, polarization control, and Raman (physical) beam alignment.

THIS PAGE INTENTIONALLY LEFT BLANK

CHAPTER 6:
Outlook and Conclusions

We have constructed from scratch an apparatus consisting of a 2D-MOT and a vacuum chamber in which we can conduct experiments on the resultant continuous atom beam. The atoms' transit times through laser fields act as effective laser pulse times. We have investigated Raman spectra, Ramsey interference, and spin echo interference in these continuous fields; these measurements have been in good agreement with theory. Though the use of continuous atom and laser beams introduces undesirable effects such as velocity spread of the atoms and divergence of the atomic and laser beams, we have described a model that accounts for these effects and shown how they impact the Ramsey interference spectra. Critically, we have simultaneously used a novel continuous-beam setup scheme which we believe will lend itself well to future efforts at miniaturization and hardening.

We have made great progress toward a continuous dual atom beam interferometer and thus accomplished the objective of my research. Work remains to be done, however, before the next steps can be taken. The stability of the signal needs to be improved, possibly via an improved locking method for the Raman laser. Although small (on the order of a MHz) frequency fluctuations of the Raman laser are not noticeable, long-term drifts (on the order of 10s of MHz) can impact long-term gyro performance. Thus we expect improved long-term stability if the Raman laser were locked. We have not yet operated with the Raman laser locked because the deleterious effects of the drifting have not been critical to our measurements and our current hard/software in the lab cannot physically lock to the operating frequency that we desire due to the lack of a nearby atomic resonance. We have noted and described some problems with the Doppler-sensitive configuration. We believe one problem with this configuration is simply a signal-to-noise issue. Since the Doppler-sensitive signal is a fraction of the Doppler-free signal, improved absolute Doppler-free signal would be beneficial. This improvement could possibly be achieved through more precise laser and atom beam alignments, altered shape or velocity profile of the atom beam, a different RF and detection scheme, or some combination thereof. Also, better atomic beam collimation will result in the Doppler-sensitive signals being a larger fraction of the Doppler-free signal. Additionally, it would be interesting (but not required) to continue to

investigate and address the cause(s) of asymmetry we have observed in the Ramsey and spin echo interference patterns.

Once these issues are addressed the experiment can be taken forward. The next step will be to take a measurement of rotation. We have already added a user-controlled rotation stage (pictured in Figure 6.1) underneath the apparatus' breadboard and conducted preliminary testing. Once we have reproducible and consistent Doppler-sensitive spin echo interference, the rotation of the apparatus upon the rotation stage is ready to be measured. After that, the next step would be a measurement of the Earth's rotation. This would obviously not require the rotation stage, but it would require the entire apparatus to be reoriented. The current setup was designed around the layout of the optics table and the laboratory. Unfortunately this orientation is in the worst possible direction with regard to the Earth's rotation axis and will need to be addressed in future work.
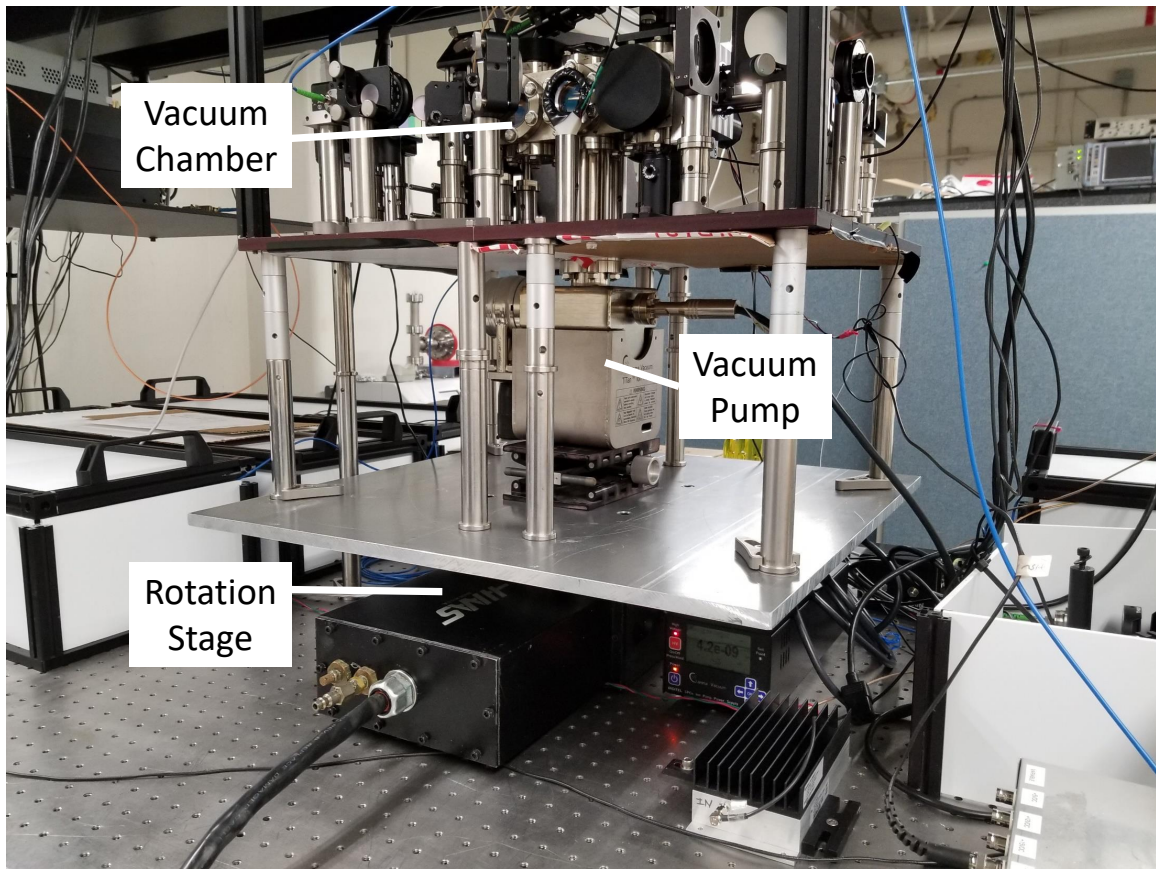
Figure 6.1: The apparatus on top of the rotation stage.

Finally, once rotation measurements have been made, the next phase of the research would involve measuring accelerations. This would require the addition of a second, anti-parallel atomic beam (as discussed in Section 4.7). With the lessons learned during the course of this research regarding continuous beams, this would be the final step in the characterization phase before the experiment would be ready to be scaled down to a more operational size.

THIS PAGE INTENTIONALLY LEFT BLANK

APPENDIX: Branching Ratio Calculations

A.1 Repumping

As mentioned in Section 2.2, the branching ratio describes the ratio of decay into different ground states. It is calculated by summing dipole matrix elements for the transitions between the various magnetic sublevels as listed in Table (A.1) [24], [33]. For the purposes of this discussion, the units of these numbers may be considered arbitrary, and their utility comes from summing all of the elements for a given hyperfine transition (i.e., F' to F).

Table A.1: Squared transition dipole moments for a portion of the ^{85}Rb D2 transition; summing all terms of a given hyperfine transition gives the relative strength of the transition compared to the others.

Excited States ($5^2P_{3/2}$)

		$F' = 2$					$F' = 3$						
	m_F	-2	-1	0	1	2	-3	-2	-1	0	1	2	3
$F = 2$	-2	7/27	7/54				2/9	2/27	2/135				
	-1	7/54	7/108	7/36				4/27	16/135	2/45			
	0		7/36		7/36				4/45	2/15	4/45		
	1			7/36	7/108	7/54				2/45	16/135	4/27	
	2				7/54	7/27					2/135	2/27	2/9
Ground States ($5^2S_{1/2}$)	-3	5/63					5/24	5/72					
	-2	5/189	10/189				5/72	5/54	25/216				
	-1	1/189	8/189	2/63				25/216	5/216	5/36			
$F = 3$	0		1/63	1/21	1/63				5/36		5/36		
	1			2/63	8/189	1/189				5/36	5/216	25/216	
	2				10/189	5/189					25/216	5/54	5/72
	3					5/63						5/72	5/24

For the decay from $F' = 3$ into $F = 2$ and $F = 3$ (as in the case of the repumping discussion), we have

$$F' = 3 \rightarrow F = 3 \quad : \quad \frac{5}{24} + \frac{5}{72} + \frac{5}{72} + \frac{5}{54} + \frac{25}{216} + \frac{25}{216} + \frac{5}{216} + \frac{5}{36}$$
$$+ \frac{5}{36} + \frac{5}{36} + \frac{5}{36} + \frac{5}{216} + \frac{25}{216} + \frac{25}{216} + \frac{5}{54} + \frac{5}{72}$$
$$+ \frac{5}{72} + \frac{5}{24}$$
$$F' = 3 \rightarrow F = 3 \quad : \quad \frac{35}{18}, \tag{A.1}$$

and

$$F' = 3 \rightarrow F = 2 \quad : \quad \frac{2}{9} + \frac{7}{27} + \frac{2}{135} + \frac{4}{27} + \frac{7}{108} + \frac{2}{45} + \frac{4}{45}$$
$$+ \frac{4}{45} + \frac{2}{45} + \frac{7}{108} + \frac{4}{27} + \frac{2}{135} + \frac{7}{27} + \frac{2}{9}$$
$$F' = 3 \rightarrow F = 2 \quad : \quad \frac{14}{9}, \tag{A.2}$$

which gives a ratio of

$$\frac{F' = 3 \rightarrow F = 3}{F' = 3 \rightarrow F = 2} = \frac{3518}{149} = \frac{35}{28} = \frac{5}{4} = 1.2. \tag{A.3}$$

Therefore, about half of the atoms that happen to get promoted to $F' = 3$ end up in $F = 2$.

A.2   Optical Pumping

In Section 2.4, we looked at decay from $F' = 2$ into $F = 2$ and $F = 3$. By referring back to Table (A.1), we can quickly calculate this branching ratio as well:

$$F' = 2 \rightarrow F = 3 \quad : \quad \frac{5}{63} + \frac{5}{189} + \frac{10}{189} + \frac{1}{189} + \frac{8}{189} + \frac{2}{63} + \frac{1}{63} + \frac{1}{21}$$
$$+ \frac{1}{63} + \frac{2}{63} + \frac{8}{189} + \frac{1}{189} + \frac{10}{189} + \frac{5}{189} + \frac{5}{63}$$
$$F' = 2 \rightarrow F = 3 \quad : \quad \frac{105}{189} = \frac{35}{63}, \tag{A.4}$$

and

$$F' = 2 \to F = 2 \quad : \quad \frac{7}{27} + \frac{7}{54} + \frac{7}{54} + \frac{7}{108} + \frac{7}{36} + \frac{7}{36}$$
$$+ \frac{7}{36} + \frac{7}{36} + \frac{7}{108} + \frac{7}{54} + \frac{7}{54} + \frac{7}{27}$$
$$F' = 2 \to F = 2 \quad : \quad \frac{35}{18}, \tag{A.5}$$

which gives a ratio of

$$\frac{F' = 2 \to F = 2}{F' = 2 \to F = 3} = \frac{3518}{3563} = \left(\frac{35}{18}\right)\left(\frac{63}{35}\right) = \frac{7}{2} = 3.5. \tag{A.6}$$

Thus the decay from $F' = 2$ is about four times stronger into $F = 2$ than into $F = 3$.

THIS PAGE INTENTIONALLY LEFT BLANK

List of References

[1] A. Meldrum, M. Manicchia, J. P. Davis, and F. A. Narducci, "Raman spectroscopy using a continuous beam from a 2D MOT," in *Steep Dispersion Engineering and Opto-Atomic Precision Metrology XI*, S. M. Shahriar and J. Scheuer, Eds., International Society for Optics and Photonics. SPIE, 2018, vol. 10548, pp. 114 – 124. Available: https://doi.org/10.1117/12.2299225

[2] M. Scully and J. Dowling, "Quantum-noise limits to matter-wave interferometry," *Phys. Rev. A*, vol. 48, pp. 3186–3190, Oct 1993. Available: https://link.aps.org/doi/10.1103/PhysRevA.48.3186

[3] D. Keith, C. Ekstrom, Q. Turchette, and D. Pritchard, "An interferometer for atoms," *Phys. Rev. Lett.*, vol. 66, pp. 2693–2696, May 1991. Available: https://link.aps.org/doi/10.1103/PhysRevLett.66.2693

[4] F. Riehle, T. Kisters, J. Helmcke, and C. Bordé, "Optical Ramsey spectroscopy in a rotating frame: Sagnac effect in a matter-wave interferometer," *Phys. Rev. Lett.*, vol. 67, pp. 177–180, Jul 1991. Available: https://link.aps.org/doi/10.1103/PhysRevLett.67.177

[5] O. Carnal and J. Mlynek, "Young's double-slit experiment with atoms: A simple atom interferometer," *Phys. Rev. Lett.*, vol. 66, pp. 2689–2692, May 1991. Available: https://link.aps.org/doi/10.1103/PhysRevLett.66.2689

[6] M. Kasevich and S. Chu, "Atomic interferometry using stimulated Raman transitions," *Phys. Rev. Lett.*, vol. 67, pp. 181–184, Jul 1991. Available: https://link.aps.org/doi/10.1103/PhysRevLett.67.181

[7] M. Cadoret, E. de Mirandes, P. Cladé, S. Guellati-Khélifa, C. Schwob, F. Nez, L. Julien, and F. Biraben, "Combination of Bloch oscillations with a Ramsey-Bordé interferometer: New determination of the fine structure constant," *Phys. Rev. Lett.*, vol. 101, p. 230801, Dec 2008. Available: https://link.aps.org/doi/10.1103/PhysRevLett.101.230801

[8] H. Müller, A. Peters, and S. Chu, "A precision measurement of the gravitational redshift by the interference of matter waves," *Nature*, vol. 463, pp. 926–929, 2010. Available: https://doi.org/10.1038/nature08776

[9] Q. Bodart, S. Merlet, N. Malossi, F. P. Dos Santos, P. Bouyer, and A. Landragin, "A cold atom pyramidal gravimeter with a single laser beam," *Applied Physics Letters*, vol. 96, no. 13, p. 134101, 2010. Available: https://doi.org/10.1063/1.3373917

107

[10] J. M. McGuirk, G. T. Foster, J. B. Fixler, M. J. Snadden, and M. A. Kasevich, "Sensitive absolute-gravity gradiometry using atom interferometry," *Phys. Rev. A*, vol. 65, p. 033608, Feb 2002. Available: https://link.aps.org/doi/10.1103/PhysRevA.65.033608

[11] B. Canuel, F. Leduc, D. Holleville, A. Gauguet, J. Fils, A. Virdis, A. Clairon, N. Dimarcq, C. J. Bordé, A. Landragin, and P. Bouyer, "Six-axis inertial sensor using cold-atom interferometry," *Phys. Rev. Lett.*, vol. 97, p. 010402, Jul 2006. Available: https://link.aps.org/doi/10.1103/PhysRevLett.97.010402

[12] D. S. Durfee, Y. K. Shaham, and M. A. Kasevich, "Long-term stability of an area-reversible atom-interferometer Sagnac gyroscope," *Phys. Rev. Lett.*, vol. 97, p. 240801, Dec 2006. Available: https://link.aps.org/doi/10.1103/PhysRevLett.97.240801

[13] S. Wu, E. Su, and M. Prentiss, "Demonstration of an area-enclosing guided-atom interferometer for rotation sensing," *Phys. Rev. Lett.*, vol. 99, p. 173201, Oct 2007. Available: https://link.aps.org/doi/10.1103/PhysRevLett.99.173201

[14] S. M. Dickerson, J. M. Hogan, A. Sugarbaker, D. M. S. Johnson, and M. A. Kasevich, "Multiaxis inertial sensing with long-time point source atom interferometry," *Phys. Rev. Lett.*, vol. 111, p. 083001, Aug 2013. Available: https://link.aps.org/doi/10.1103/PhysRevLett.111.083001

[15] M. Manicchia, J. G. Lee, G. R. Welch, J. Mimih, and F. A. Narducci, "Doppler-free and Doppler-sensitive Ramsey spectroscopy in a continuous beam of cold atoms," in *Rochester Conference on Coherence and Quantum Optics (CQO-11)*. Optical Society of America, 2019, p. W6A.2. Available: http://www.osapublishing.org/abstract.cfm?URI=CQO-2019-W6A.2

[16] X. H., "A continuous cold atomic beam interferometer," *J. Appl. Phys.*, vol. 117, p. 094901, 2015.

[17] C. Cohen-Tannoudji, B. Diu, and F. Laloë, *Quantum Mechanics*, first edition ed. France: Wiley, 1977, vol. 1 and 2.

[18] M. O. Scully and M. S. Zubairy, *Quantum Optics*. United Kingdom: Cambridge University Press, 1997.

[19] H. J. Kimble and L. Mandel, "Theory of resonance fluorescence," *Phys. Rev. A*, vol. 13, pp. 2123–2144, Jun 1976. Available: https://link.aps.org/doi/10.1103/PhysRevA.13.2123

[20] W. D. Phillips, "Laser cooling and trapping of neutral atoms," in *Proceedings of the International School of Physics «Enrico Fermi»*, W. D. P. E. Arimondo and F. Strumia, Eds., Italian Physical Society. North-Hollan Elsevier Science Publishers B. V., 1992, vol. CXVIII, pp. 289 – 343.

[21] H. J. Metcalf and P. van der Straten, *Laser Cooling and Trapping*. New York: Springer, 1999.

[22] E. Raab, M. Prentiss, A. Cable, S. Chu, and D. Pritchard, "Trapping of neutral sodium atoms with radiation pressure," *Phys. Rev. Lett.*, vol. 59, pp. 2631–2634, Dec 1987. Available: https://link.aps.org/doi/10.1103/PhysRevLett.59.2631

[23] E. Riis, D. S. Weiss, K. A. Moler, and S. Chu, "Atom funnel for the production of a slow, high-density atomic beam," *Phys. Rev. Lett.*, vol. 64, pp. 1658–1661, April 1990. Available: https://link.aps.org/doi/10.1103/PhysRevLett.64.1658

[24] D. A. Steck, "Rubidium 85 D line data," November 2019. Available: http://steck.us/alkalidata

[25] M. P. Manicchia, J. Lee, G. R. Welch, J. Mimih, and F. A. Narducci, "Construction and characterization of a continuous atom beam interferometer," *Journal of Modern Optics*, vol. 67, no. 1, pp. 69–79, 2020. Available: https://doi.org/10.1080/09500340.2019.1688410

[26] N. Ramsey and O. U. Press, *Molecular Beams* (International series of monographs on physics). OUP Oxford, 1956, ch. 2, p. 20. Available: https://books.google.com/books?id=un5XuwyZHRIC

[27] D. Braje, S. DeSavage, C. Adler, J. Davis, and F. Narducci, "A frequency selective atom interferometer magnetometer," *Journal of Modern Optics*, vol. 61, no. 1, pp. 61–71, 2014. Available: http://dx.doi.org/10.1080/09500340.2013.850776

[28] S. DeSavage, "The exploration of stimulated Raman processes in ^{85}Rb using dual amplitude pulses," Ph.D. dissertation, University of MD, Baltimore County, 2014.

[29] N. F. Ramsey, "Experiments with separated oscillatory fields and hydrogen masers," *Rev. Mod. Phys.*, vol. 62, p. 541, 1990.

[30] "Private communication from J.P. Davis to F. Narducci," 2017.

[31] T. Gustavson, A. Landragin, and M. Kasevich, "Rotation sensing with a dual atom-interferometer Sagnac gyroscope," *Classical and Quantum Gravity*, vol. 17, pp. 2385–2398, Jun 2000. Available: https://doi.org/10.1088/0264-9381/17/12/311

[32] S. DeSavage, J. Davis, and F. Narducci, "Controlling Raman resonances with magnetic fields," *J. Mod. Opt.*, vol. 60, p. 95, 2013.

[33] G. D. Domenico and A. Weis, "Transition strengths of alkali metal atoms," https://demonstrations.wolfram.com/TransitionStrengthsOfAlkaliMetalAtoms/, March 2011.

Initial Distribution List

1. Defense Technical Information Center
   Ft. Belvoir, Virginia

2. Dudley Knox Library
   Naval Postgraduate School
   Monterey, California